New molecular imaging in oncology

A focus on angiogenesis

Wouter B. Nagengast

New molecular imaging in oncology: a focus on angiogenesis

W.B. Nagengast

Stellingen behorende bij het proefschrift:

1. Het signaal verkregen bij *VEGF PET imaging* wordt met name veroorzaakt door binding van de tracer aan cel- en matrixgebonden VEGF in de micro-omgeving van de tumor. *Dit proefschrift en Stollman et al, Cancer Biother Radiopharm, 2009.*

2. De verandering in *VEGF PET imaging* signaal komen overeen met zowel de anti-angiogene respons alsmede de directe anti-tumor effecten na HSP90 inhibitie. *Dit proefschrift*

3. De VEGF expressie is verschillend in de rand en het centrum van de tumor tijdens sunitinib behandeling. *Dit proefschrift*

4. *VEGF PET imaging* is een gevoelige techniek voor het visualiseren van tumorlaesies. *Dit proefschrift*

5. De complexe interactie tussen tumorcellen en hun micro-omgeving maakt het doen van *in vivo* experimenten essentieel bij het onderzoek naar angiogene effecten. *Dit proefschrift*

6. Serendipiteit is één van de fundamenten van wetenschappelijkonderzoek.

7. Het niet kunnen onderscheiden van subpopulaties kan onnodig tot negatieve onderzoeksresultaten leiden in klinische studies.

8. Bevacizumab, gelabeld met een fluorescentie label, biedt de mogelijkheid om *VEGF imaging* ook toe te passen in de endoscopie.

9. Het niet accepteren van negatieve onderzoeksresultaten vertraagt de vooruitgang van de wetenschap.

10. "Too many people die every year worldwide because of drug issues....., they don't have any" *Artsen zonder grenzen*

11. Het opstellen van een hypothese voor het uitvoeren van een experiment is onontbeerlijk, echter de uitkomst komt er vaak niet mee overeen.

12. Wetenschap is soms net het normale leven: het ene jaar kopen we allemaal een witte auto, het jaar erop een zwarte.

13. Met vier vrouwelijke begeleiders heb ik de kabinetsdoelstellingen al gehaald.

14. **"Yes we can"** beschrijft beter het werk van dit proefschrift dan de enkele naam prijkend op de voorkant.

Financial support for the research and publication of this thesis was granted by the Dutch Cancer Society

For the publication of this thesis, financial sponsoring of the following institutions and companies is gratefully acknowledged:
Stichting Werkgroep Interne Oncologie, Roche Nederland, Novartis Oncology, University of Groningen, Schering-Plough Nederland, Genzyme Nederland, IBA Molecular, Olympus Nederland BV, FMH Endoscopy BV, Pfizer BV, AstraZeneca BV

Cover design: D.J. Buiter, Groningen
Layout: Legatron Electronic Publishing, Rotterdam
Printed by: Ipskamp Drukkers, Enschede

cmb.

RIJKSUNIVERSITEIT GRONINGEN

New molecular imaging in oncology: a focus on angiogenesis

Proefschrift

ter verkrijging van het doctoraat in de
Medische Wetenschappen
aan de Rijksuniversiteit Groningen
op gezag van de
Rector Magnificus, dr. F. Zwarts,
in het openbaar te verdedigen op
woensdag 16 december 2009
om 13.15 uur

door

Wouter Bastiaan Nagengast

geboren op 18 november 1978
te Deventer

Promotor:	Prof. dr. E.G.E. de Vries
Copromotores:	Dr. A.H. Brouwers Dr. M.N. Lub-de Hooge Dr. G.A.P. Hospers
Beoordelingscommissie:	Prof. dr. J.H. Beijnen Prof. dr. P.M. Price Prof. dr. P.H.B. Willemse

Paranimfen

Drs. B.P. Brassé

Drs. T.H. Oude Munnink

Contents

Chapter 1

Introduction

Background

Chemotherapeutic agents are the mainstay in anti-cancer treatment. Therefore patients that die of metastatic disease do so because they do not respond or develop resistance towards these anti-cancer drugs. The occurrence of tumor resistance to several structurally unrelated classes of natural products, including anthracyclines, taxanes and epipodophyllotoxines, is often referred to as multidrug resistance (MDR). MDR can be caused by several mechanisms including increased expression of the ATP-binding cassette transporters (ABC- transporters) and drug efflux pumps like P-glycoprotein (P-gp) and multidrug resistance protein (MRP1). It was initially thought, that overcoming MDR would resolve the problem of intrinsic or acquired resistance for these drugs. This was aimed for by inhibiting the drug efflux pump like P-gp. However, randomized clinical studies in different groups of cancer patients evaluating the effect of P-gp modulators when added to chemotherapeutic drugs have not shown any benefit in outcome for the patients. These and other findings let to the believe that the ceiling was reached with classical chemotherapeutic drugs. The abundance of knowledge from the preclinical research on dysregulated cellular pathways in tumor cells has resulted in the development of new targeted agents. Therefore, the use of the so-called new targeted agents, with or without chemotherapy, might be superior to circumvent MDR and enhance anti-tumor effects. Over the last decade numerous new targeted anticancer agents, specific for intra- and extra cellular tumor targets, antigens located in the extracellular matrix or at the blood vessels of tumors, have been developed. There is increasing evidence that several of these agents combined with chemotherapy can increase antitumor efficacy.

A subgroup of these agents is targeting the so-called process of angiogenesis. This process of new blood vessel formation is not only important in normal tissue development, but is also one of the hallmarks in carcinogenesis [1,2]. Already 30 years ago it was recognized that tumors need blood vessels to allow tumor cells to execute their critical growth by supplying the tumor with nutrients and oxygen, enabling disposal of metabolic waste products and it provides a route for metastatic spreading [1]. An important factor involved in angiogenesis is vascular endothelial growth factor A (hereafter referred as VEGF) [3]. It is released by tumor cells and it induces tumor neovascularization. Overexpression of VEGF occurs in many human tumor types which made VEGF a rational target for anti-angiogenic therapy. This has lead to interest in blocking the signaling of VEGF in human tumors. For this, antibodies binding to this ligand and its receptors as well as chemical molecules which can block the tyrosine kinase function of VEGF-receptors and drugs inhibiting cellular tumor signaling pathways affecting angiogenesis have been developed [4,5]. Although anti-angiogenic treatment, either as single agent or combined with chemotherapy has improved disease outcome for several

tumor types, such as renal cell cancer and colorectal cancer, benefit has been modest and often only transitory. Therefore it would be extremely helpful when a predictive marker would exist to select patients upfront. An option to achieve this might be the non-invasive use of molecular imaging. In this thesis, new targeted anti-angiogenic agents have been evaluated using different molecular (tumor) imaging techniques.

Outline of the thesis

In chapter 2 an overview is presented of molecular imaging techniques which can be used to monitor MDR non-invasively in patients. Several tracers and clinical studies in which these tracers have been evaluated are discussed. Evidence emerges that combination of chemotherapeutic drugs involved in MDR with the so-called targeted agents can improve patient outcome. Therefore, the concept of molecular imaging can also be used to visualize the targets for these new agents. Two examples, namely imaging of the epidermal growth factor 2 (HER2) and VEGF, are discussed to illustrate this new era of molecular imaging.

The blood brain barrier (BBB) is a major impediment for the delivery of several drugs to the brain, including cytotoxic, anti-epileptic, and anti-HIV drugs. The BBB is formed by specialized capillary endothelial cells which have several properties, such as strong tight junctions with a high electrical resistance, absence of fenestrations and presence of efflux-pumps such P-gp and MDR associated protein MRP1. Several strategies have been investigated to inhibit P-gp and MRP1 function, like the use of chemical inhibitors, though unfortunately, no clinical benefit has been observed. Combination with other treatment strategies which influence P-gp function could circumvent this. In the study described in chapter 3 we investigated the influence of radiotherapy on P-gp function and expression in the BBB. Healthy rat brains, naturally expressing P-gp within the BBB, were one sided irradiated. Thereafter, ^{11}C-carvedilol, a P-gp PET tracer, was used to assess the functionality of the P-gp transporter by autoradiography and to study whether irradiation could enhance the delivery of the P-gp substrate cyclosporine. These results were compared with immunohistological expression of P-gp.

Chapters 4-7 are dedicated to the development and evaluation of new molecular imaging tracers for the guidance of anti-angiogenic therapies. Non-invasive measurement of VEGF in the tumor might give insight in the available target for VEGF dependent anti-angiogenic therapy and thus assist in tumor response prediction. $VEGF_{121}$ is freely soluble, whereas $VEGF_{165}$ is secreted, though a significant fraction remains localized to the extra cellular matrix, like $VEGF_{189}$ and $VEGF_{206}$ [6]. This will most likely lead to locally high VEGF levels. Bevacizumab is an humanized monoclonal antibody, whereas ranibizumab is an humanized

Fab-fragment, both binding with high affinity to all VEGF-A isoforms. To allow *in vivo* VEGF imaging, we set up bevacizumab and ranibizumab labeling with the relatively new long-lived PET isotope ^{89}Zirconium [^{89}Zr] and short life PET isotope ^{18}Fluor [^{18}F], and the widely available single gamma emitting isotope ^{111}Indium [^{111}In] and evaluated quantitative VEGF PET imaging and used these tracers in the evaluation of anti-angiogenic therapy.

In chapter 4 the in vitro and *in vivo* development of radiolabeled bevacizumab is described. Labeling conditions were optimized to achieve maximal specific activity (Mbq/mg protein) and maximal labeling efficiency (>95%). Subsequently, we tested the immunoreactivity of ^{111}In- and ^{89}Zr-bevacizumab with an newly developed VEGF ELISA method. Thereafter, we evaluated ^{111}In- and ^{89}Zr-bevacizumab *in vivo* in a SKOV-3 human ovarian tumor xenografts model. Tumor uptake of ^{111}In- and ^{89}Zr-bevacizumab was evaluated at 24, 72 and 168 h post injection. In addition, ^{89}Zr-bevacizumab tumor uptake was measured by microPET imaging and compared to the uptake of ^{89}Zr-IgG. Hereafter, we investigated microscopically the localization of ^{89}Zr-bevacizumab.

Thereafter, in another series of experiment we investigated whether VEGF imaging could serve as biomarkers in the evaluation of anti-angiogenic therapy. In chapter 5 we investigated whether ^{89}Zr-bevacizumab could serve as an early biomarker of response following treatment with the new Heat Shock Protein 90 (HSP90) inhibitor NVP-AUY922. HSP90 is a molecular chaperone, involved in maintaining the conformation, stability, cellular localization and activity of several key oncogenic client proteins [7,8]. HSP90 is constitutively expressed at 2 to 10 fold higher levels in cancer cells and present in active multi-chaperone complexes, conferring relative sensitivity to treatment with HSP90 inhibitors compared to their normal counterparts [7,9]. At this moment, several HSP90 inhibitors are being developed but are no biomarkers to predict the effect of, or monitor, HSP90 inhibition therapy in individual patients. One potential way to monitor HSP90 therapy is to prove its effect via changes in client proteins of HSP90. However, most of these client proteins can only be measured by collecting tumor biopsies. A suitable candidate is VEGF, a downstream product of various HSP90 client proteins [8,10]. We hypothesized that HSP90 inhibition would lead to decreased VEGF levels. In chapter 5 we describe the study in which we investigated in vitro the effect of NVP-AUY922 on VEGF production in the human ovarian cancer cell line A2780 and its cisplatin resistant subline CP70. Next, the effect of NVP-AUY922 was investigated *in vivo* in A2780 and CP70 xenografts. ^{89}Zr-bevacizumab PET was performed before and after NVP-AUY922 treatment, and the imaging results were related to histological response and *ex vivo* tumor VEGF levels.

To assess the feasibility of VEGF imaging clinically, a study was performed in metastatic melanoma patients (chapter 6). Melanoma causes more than 75 per cent of all skin cancer deaths. The incidence has steadily risen in recent decades particularly among Caucasians in areas of high sun exposure. Melanoma features a specific metastatic spread from primary tumor to regional lymphatic beds and then distant metastasis [11,12]. Melanoma cells produce high amounts of VEGF-A which correlates with advanced disease, tumor burden, poor overall survival and probability of progression [13]. Furthermore, VEGF-A expression of nodal metastases is higher compared to primary tumors indicating the importance of a pro-angiogenic switch in the process of melanoma progression [11]. Therefore, the use of new anti-VEGF targeted therapies could be a potential step in the treatment of melanoma patients. The feasibility of ^{111}In-bevacizumab single photon emission tomography (SPECT) VEGF imaging was compared with ^{18}F-FDG PET, a glucose analogue reflecting glucose uptake and metabolism of the tumor, and CT imaging in lymph node positive stage III and IV melanoma patients eligible for surgery. Patients were scanned with ^{111}In-bevacizumab at day 0, 2, 4 and 7 post injection of the tracer.

Besides tumor angiogenesis, VEGF plays an important role fysiological processes and other diseases. One example is hereditary hemorrhagic telangiectasia (HHT). In this disease, vascular malformations are formed due to increased VEGF signaling. In chapter 6b we illustrate the feasibility of VEGF-SPECT in a HTT patient. Furthermore, we shortly describe the effect of long term treatment with bevacizumab in this patient.

Since the approval of anti-angiogenic treatment, many questions exist regarding heterogeneity of tumor response and tumor adaptation or resistance to anti-angiogenic therapy. Recently in preclinical models it has been shown that drugs blocking the VEGF/VEGF-receptor pathway such as the clinically used VEGF receptor tyrosine kinase inhibitor (TKI) sunitinib, did not only have an anti-angiogeneic effect. They can increase also the invasiveness of primary tumor boundary and enhance tumor lymph node infiltration and distant metastases.

In chapter 7 we investigated the effect of sunitinib treatment and its withdrawal on tumor behavior with the PET tracers ^{18}F-FDG and ^{15}O-water as well as with the ^{89}Zr-ranibizumab VEGF-PET tracer in two angiogenic human xenograft tumor models. ^{89}Zr-ranibizumab is an humanized Fab-fragment with high affinity for all VEGF-A isoforms. Due to its short half life it accumulates more rapidly within the tumor compared to bevacizumab giving instant information on the tumor status. In addition, it allows short imaging intervals during anti-angiogenic therapy. In both A2780 and Colo205, a human colon cancer cell line, tumor xenografts were treated with daily sunitinib for 14 days, or for 7 days followed by

a stop week. At baseline, day 7 and 14 ^{18}F-FDG, ^{15}O-water PET and/or ^{89}Zr-ranibizumab VEGF-PET were performed. In an effort to select the technique which would best reflect whole angiogenic tumor behavior during sunitinib treatment imaging results were in depth compared with tumor growth and histological and immunohistochemical findings in the tumor. In addition, we show the feasibility of clinical VEGF-PET in a metastatic renal cell carcinoma patient.

In chapter 8 and 9 the results of the studies are summarized and ideas and concepts for future studies are described.

References

1. Shimanuki, Y. *et al.* Role of serum vascular endothelial growth factor in the prediction of angiogenesis and prognosis for non-small cell lung cancer. *Lung* 183, 29-42 (2005).
2. Carmeliet, P. VEGF as a key mediator of angiogenesis in cancer. *Oncology* 69 Suppl 3, 4-10 (2005).
3. Ferrara, N. Vascular endothelial growth factor: basic science and clinical progress. *Endocr. Rev.* 25, 581-611 (2004).
4. Zhang, J., Yang, P. L. & Gray, N. S. Targeting cancer with small molecule kinase inhibitors. *Nat. Rev. Cancer* 9, 28-39 (2009).
5. Imai, K. & Takaoka, A. Comparing antibody and small-molecule therapies for cancer. *Nat. Rev. Cancer* 6, 714-727 (2006).
6. Ferrara, N., Gerber, H. P. & LeCouter, J. The biology of VEGF and its receptors. *Nat. Med.* 9, 669-676 (2003).
7. Xu, W. & Neckers, L. Targeting the molecular chaperone heat shock protein 90 provides a multifaceted effect on diverse cell signaling pathways of cancer cells. *Clin. Cancer Res.* 13, 1625-1629 (2007).
8. Neckers, L. Heat shock protein 90: the cancer chaperone. *J. Biosci.* 32, 517-530 (2007).
9. Kamal, A. *et al.* A high-affinity conformation of Hsp90 confers tumour selectivity on Hsp90 inhibitors. *Nature* 425, 407-410 (2003).
10. Ferrara, N. & Davis-Smyth, T. The biology of vascular endothelial growth factor. *Endocr. Rev.* 18, 4-25 (1997).
11. Gorski, D. H., Leal, A. D. & Goydos, J. S. Differential expression of vascular endothelial growth factor-A isoforms at different stages of melanoma progression. *J. Am. Coll. Surg.* 197, 408-418 (2003).
12. Tas, F. *et al.* Circulating serum levels of angiogenic factors and vascular endothelial growth factor receptors 1 and 2 in melanoma patients. *Melanoma Res.* 16, 405-411 (2006).
13. Ugurel, S., Rappl, G., Tilgen, W. & Reinhold, U. Increased serum concentration of angiogenic factors in malignant melanoma patients correlates with tumor progression and survival. *J. Clin. Oncol.* 19, 577-583 (2001).

Chapter 2

Multidrug resistance in oncology and beyond: from imaging of drug efflux pumps to cellular drug targets

Wouter B. Nagengast, Thijs H. Oude Munnink, Eli C.F. Dijkers, Geke A.P. Hospers, Adrienne H. Brouwers, Carolien P. Schröder, Marjolijn Lub-de Hooge, Elisabeth G.E. de Vries

Department of Medical Oncology University Medical Center Groningen, The Netherlands

In press, Humana Press, chapter in Multi Drug Resistance

Abstract

Resistance of tumor cells to several structurally unrelated classes of natural products, including anthracyclines, taxanes and epipodophyllotoxines, is often referred as multidrug resistance (MDR). This is associated with ABC transporters which function as drug efflux pumps such as P-gp and MRP1. Due to the hypothesis in the early eighties that blockade of these efflux pumps by modulators would improve the effect of chemotherapy, extensive effort has been put to visualize these pumps using nuclear imaging with several specific tracers, using both SPECT and PET techniques. The methods and possibilities to visualize these pumps in both the tumor and the blood brain barrier will be discussed. Due to the fact that the addition of P-gp or MRP modulators has not shown any clinical benefit in patient outcome, these specific MDR tracers are not routinely used in clinical practice. Evidence emerges that combination of chemotherapeutic drugs involved in MDR with, the so-called targeted agents can improve patient outcome. The concept of molecular imaging can also be used to visualize the targets for these agents, such as HER2/neu and angiogenic factors like vascular endothelial growth factor (VEGF). Potentially visualizing molecular drug targets in the tumor can function as biomarkers to support treatment decision for the individual patient.

Introduction

The occurrence of resistance to several structurally unrelated classes of natural products, including anthracyclines, taxanes and epipodophyllotoxines, is often referred as multidrug resistance (MDR). MDR can be caused by several mechanisms such as increased expression of the ATP-binding cassette transporters (ABC- transporters) and drug efflux pumps like P-glycoprotein (P-gp) and multidrug resistance protein (MRP1). In the nineties the idea was that overcoming MDR would resolve the problem of intrinsic or acquired resistance for these drugs. However, randomized clinical studies in different groups of cancer patients evaluating the effect of P-gp or MRP1 modulators combined with chemotherapy have not shown any benefit in outcome for the patients [1,2]. Increasingly thereafter, the idea was that the ceiling was reached with classical chemotherapeutic drugs and that the use of a different approach, the combination with, the so-called targeted agents might be superior to circumvent MDR. Over the last decade numerous targeted anticancer agents, specific for intra- and extra cellular tumor targets, antigens located in the extracellular matrix or at the blood vessels of tumors, have been developed. To select patients upfront and determine early treatment response, new tracers and imaging modalities are being developed which information reflects with molecular changes during therapy. These tracers may give insight in the biological behavior of tumors and could help in the follow-up of targeted therapies and chemotherapy.

In this chapter we will shortly address the methods and possibilities of imaging classical MDR mechanism. In addition we will address the option to image targets in the tumor for targeted therapies. We will focus on HER2 and VEGF imaging, as both can serve as target for drugs that can increase the effect of MDR drugs.

MDR drug efflux pump detection in tumor and blood brain barrier

MDR detection in tumor

Various detection assays provide information about the presence of drug efflux pumps in the tumor at the mRNA and protein levels. However, these methods do not provide information about the dynamic function of P-gp and MRP *in vivo*. For that reason, to study of P-gp and MRP-mediated transport, single-photon emission computed tomography (SPECT) and positron emission tomography (PET) have been used. Several substrates for P-gp and MRP have been radiolabeled with different SPECT and PET isotopes and both pre- as clinical studies have demonstrated the potential and Achilles' heel of these tracers.

^{99}Technetium (^{99m}Tc) sestamibi, a SPECT tracer, is a substrate for P-gp and MRP, and has been used in both pre- and clinical studies for tumor imaging, and for visualization of P-gp-

mediated transport after modulation with competing drugs of the P-gp pump [3]. Kostakoglu and colleagues demonstrated the potential of the tracer by a nice inverse correlation between tumor uptake of (^{99m}Tc) sestamibi and P-gp staining by immunohistochemistry (IHC) on tumor biopsies and surgical material in breast and lung cancer patients [4]. Hereafter, ^{99m}Tc-sestamibi was used in breast cancer patients to predict tumor responses during neoadjuvant epirubicin therapy. The tumor clearance rate (cut off ≤ 204 min) of ^{99m}Tc-sestamibi out of the tumor was used as a predictive marker to characterize patients. In 15 out of 17 patients (88%) with rapid tracer clearance the mastectomy specimens showed macroscopic evidence of residual tumor, which contained highly dense and viable tumor cells. This indicates a lack of tumor response to the treatment, again demonstrating a nice correlation between imaging data and *ex vivo* tumor analysis [5]. Though in contrast to this, only out eight of 22 (36%) patients with prolonged tracer uptake had no pathologic evidence of residual tumor or showed only scattered and/or small clusters of tumor cells in a dense hyalinized stromal tissue after surgical resection of the tumor. No relationship between tracer uptake and/or patient outcome with P-gp or MRP expression was investigated in this study, which makes it difficult to interpret whether the clearance rate was P-gp or MRP dependent.

Other ^{99m}Tc SPECT radiopharmaceuticals, such as ^{99m}Tc-tetrofosmin and several ^{99}Tc-Q complexes, are also substrates for P-gp and have been tested clinically. In patients with hepatocelular carcinoma ^{99m}Tc-tetrofosmin imaging displayed a very low sensitivity for the detection of carcinomas [6]. Unfortunately, tracer uptake was not correlated with P-gp expression by IHC. High P-gp expression could have explained this low sensitivity. This is supported by Wang et al., who demonstrated that a negative ^{99}Tc-methoxyisobutyl isonitrile (MIBI) scan (68 out of 78 patients) correlated with positive P-gp expression in hepato-cellular carcinoma, suggesting the ability of MDR assessment in this tumor type [7]. This finding was supported by a study in which ^{99m}Tc-tetrofosmin imaging revealed lesions which were both P-gp and MRP negative by post operative P-gp IHC in 33 patients with parathyroid adenoma. Tumors with positive P-gp and/or MRP staining could not be detected with ^{99m}Tc-tetrofosmin imaging indicating a good correlation between imaging data and *ex vivo* analysis [6].

The potential of response to chemotherapy prediction by MDR imaging has been most extensively investigated in lung cancer patients. In 20 patients with non-small cell lung cancer (NSCLC) a low baseline uptake of ^{99m}Tc-tetrofosmin was correlated with a poor response to paclitaxel based chemotherapy. The authors suggested that this was due to high MDR and/or P-gp expression [8]. Similar results were seen in patients with small cell lung cancer with ^{99m}Tc-tetrofosmin imaging prior to cisplatin and etoposide based chemotherapy [9]. All

patients (n=16) with a negative scan prior to chemotherapy had a poor response to therapy. However, 4 out of 23 patients with a positive ^{99m}Tc-tetrofosmin image had also a poor response, which could be due to other resistance mechanisms which decreases the specificity of this scan, resulting in false positive scans. Furthermore, in patients with a negative ^{99m}Tc-tetrofosmin scan (low uptake) a poor correlation was found between tracer uptake and P-gp expression; 6 out of 16 patients with a negative scan did not show any P-gp expression in tumor biopsy material by IHC. Therefore, besides expression of MDR related proteins other factors could contribute to the clearance of ^{99m}Tc-tetrofosmin in these patients. A very good correlation between ^{99}Tc-MIBI imaging and P-gp IHC staining was found in 30 NSCLC (stage IIIb and IV) patients. All patients with a positive ^{99}Tc-MIBI scan had negative P-gp expression and vice versa. All 15 cases with a good response (complete response or partial response assessed 3 months after completion of the treatment by clinical and radiological methods) had a positive ^{99}Tc-MIBI scan and negative P-gp staining. In patients who did not responded on paclitaxel based chemotherapy both positive (5 out of 15) and negative (10 out of 15) ^{99}Tc-MIBI scans prior to therapy were seen, which, comparable with ^{99m}Tc-tetrofosmin imaging, in false positive imaging results [9,10].

A relative large study was performed in 82 untreated breast cancer patients, which aimed to determine P-gp and MRP expression by visual and quantitative indices of double-phase ^{99m}Tc MIBI scintimammography, quantifying an early and late tumor uptake. The early (10 min post injection of the tracer (pi)) and delayed (3 h pi) tumor to normal tissue ratio (T/N ratio) was assessed to compare the initial uptake of ^{99m}Tc MIBI and the wash-out rate of tracer out of the tumor. It was hypothesized that the wash-out rate was affected by the presence of P-gp or MRP. Both the early and delayed T/N ratio of the P-gp-negative and MRP-negative group was higher than of the P-gp-positive and MRP-positive group. However, there were no significant differences in wash-out rate according to P-gp and MRP expression [11].

Several other agents, including the PET tracers ^{11}C-colchicine and ^{11}C-verapamil have been evaluated for *in vivo* quantification of P-gp-mediated transport with PET imaging [3]. We analyzed after iv injection the ^{11}C-verapamil kinetics in five cancer patients using PET. One h after injection, accumulation of ^{11}C in lungs, heart and tumor was respectively 43.0%, 1.3% and 0.9% of the injected verapamil dose. Half-lives of ^{11}C-verapamil in these tissues were 46.2 min, 73.8 min and 23.7 min, respectively [12]. This showed that iv administered ^{11}C-verapamil was mainly extracted by the lungs and that efflux of ^{11}C-verapamil administered as bolus, out of solid tumor tissue is relatively fast.

Specific MRP expression has been less extensively investigated even though given the fact that leukotrienes are specific substrates for MRP. Therefore, N-^{11}C-acetyl-leukotriene

E4 provides an opportunity to study MRP function non-invasively [13]. Results obtained in MRP2 mutated GY/TR$^-$ rats (MRP2 is defective in GY/TR$^-$ rats due to MRP2 mutations) demonstrated visualization of MRP-mediated transport. This tracer permits the study of MRP transport function abnormalities *in vivo*, e.g. in Dubin-Johnson patients, who are MRP2 gene deficient.

Several studies have demonstrated that the substrate specificity of MRP1 is very similar to that of MRP2. Most substrates are conjugated to, or co-transported with, glutathione (GSH), glucuronide or sulfate [14]. We studied MRP2 in a different way. We analyzed the transporter specificity of the cholescintigraphic agents ^{99m}Tc-HIDA and ^{99m}Tc-MIBI, which are already used clinically for myocardial perfusion measurements. Secondly, we aimed to deduce MRP and P-gp functions *in vivo* from hepatic ^{99m}Tc kinetics [14]. In vitro transporter specificity was demonstrated measuring the accumulation of radioactivity in the human small cell lung cancer cell lines GLC4, GLC4/ADR150x (MRP1-overexpressing/P-gp-negative) and GLC4/P-gp (P-gp-overexpressing). ^{99m}Tc-HIDA accumulated 5.8-fold less in GLC4/ADR150x cells than in GLC4 or GLC4/P-gp cells. In GLC4/ADR150x, the cellular ^{99m}Tc-HIDA content was 3.4-fold higher following exposure to by the MRP1,2 inhibitor MK571 (50 μM), while the MK571 had no measurable effect in GLC4 and GLC4/P-gp cells. ^{99m}Tc-MIBI accumulated less in GLC4/P-gp and GLC4/ADR150x cells than in GLC4 cells. *In vivo*, bile secretion of ^{99m}Tc-HIDA was impaired in GY/TR$^-$ compared to control rats and not affected by GSH depletion in GY/TR$^-$ rats. Hepatic secretion of ^{99m}Tc-HIDA was slower in GY/TR$^-$ rats ($t_{1/2}$ 40 min) than in control rats ($t_{1/2}$ 7 min). Bile secretion of ^{99m}Tc-MIBI was similar in both rat strains and impaired by GSH depletion in control rats only, indicating compensatory activity of additional transporter(s) in GY/TR- rats. ^{99m}Tc-HIDA is transported only by MRP1,2, while ^{99m}Tc-MIBI is transported by P-gp and MRP1,2. The results indicate that hepatic P-gp and MRP1,2 function can be assessed *in vivo* by sequential use of both radiopharmaceuticals [14].

Apart from functional imaging, static P-gp expression can also be assessed with the ^{111}In-labeled 15D3 monoclonal anti-P-gp [15]. In Nude BALB/c mice with subcutaneously growing human uterine sarcoma cell tumors with either high (MES-SA/D×5 1977) or low (MES-SA 1976) P-gp expression were used. Uptake was higher in the high compared to low P-gp expressing tumors.

All the above examples nicely illustrate that *in vivo* imaging of the function of ABC transporters involved in MDR in tumors is possible. However, the interest in imaging them in cancer patients is fading due to the fact that it is difficult to use this information for standard clinical patient care. This is partly the consequence of the frequent occurrence of

false positive scans, which could be due to other responsible mechanisms which lead to poor patient outcome, and new targeted therapies with has been currently frequently used in the treatment of patients. Therefore, new targeted therapies have emerged the need for additional new imaging probes which give information on targets involved in tumor resistance of these new therapies.

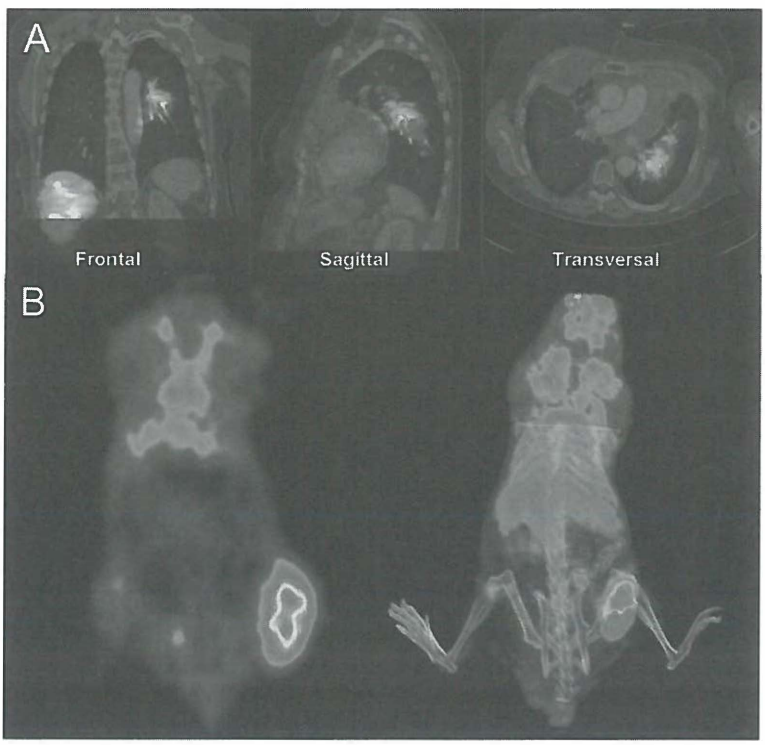

Figure 1. (A) Fused computed tomography (CT) with indium-111–diethylenetriamine penta-acetic acid anhydride (111In-DTPA) –trastuzumab single-photon emission tomography (SPECT) image (96 h after tracer injection). Tumor indicated by arrow. *Reproduced with permission of The Journal of Clinical Oncology*. (B) Coronal ^{89}Zr-bevacizumab MicroPET image and fused 3D ^{89}Zr-bevacizumab/CT image 144 h post injection. (see page 150 for color picture)

MDR detection in blood-brain barrier

The blood–brain barrier (BBB) is a major impediment for the delivery of several drugs to the brain, including cytotoxic, antiepileptic, and anti-HIV drugs. The BBB is formed by

specialized capillary endothelial cells, which have several properties, such as strong tight junctions with a high electrical resistance, absence of fenestrations and presence of efflux-pumps such P-gp and MRP1. Strategies to pass the BBB have been directed to inhibition of efflux pump function. At present, the concept of efflux pump inhibition has been most extensively studied for P-gp. Studies in rodents have shown that P-gp function can be inhibited with cyclosporine [16-18]. Numerous knockout mouse studies have revealed that P-gp limits drug distribution across the mouse BBB. To determine the importance of P-gp at the human BBB, P-gp activity was analyzed with ^{11}C-verapamil as the P-gp substrate and cyclosporine as the competing P-gp substrate. ^{11}C-verapamil was administered to healthy volunteers (6 women and 6 men) as an iv infusion before and after at least 1 h after infusion of cyclosporine (2.5 mg x kg(-1) x h(-1)). The brain uptake of ^{11}C-radioactivity (brain area under the curve [AUCbrain]/blood area under the curve [AUCblood]) was determined in the presence and absence of cyclosporine. The AUCbrain/AUCblood ratio of ^{11}C-radioactivity was increased by 88% +/- 20% in the presence of cyclosporine without affecting ^{11}C-verapamil metabolism or plasma protein binding. The corresponding increases ^{11}C-verapamil in the brain white and gray matter were comparable.

Beside pharmacologic modulation of P-gp by specific substrates such as cyclosporine, other therapies like radiotherapy could potentially also influence P-gp function. Early effects on brain capillary endothelium were studied by Mima et al [19]. They exposed in rats one brain hemisphere to a single dose of 25 Gy and demonstrated that P-gp expression was lower in the irradiated hemisphere compared to the non-irradiated hemisphere 5 days after irradiation. It is therefore hypothesized that brain irradiation could also be used to enhance the delivery of P-gp substrates to the brain. We irradiated the right brain hemisphere of rats with single fractions of radiotherapy to elucidate whether radiation therapy reduced P-gp expression and function in the brain, as measured with the P-gp substrate ^{11}C-carvedilol [20]. The right hemispheres received single doses of 2-25 Gy followed by 10 mg/kg of the P-gp substrate cyclosporine iv, with once 15 Gy followed by cyclosporine, or with fractionated irradiation (4 x 5 Gy) followed by cyclosporine 5 days later. Irradiation increased ^{11}C-carvedilol uptake dose-dependently, to a maximum of 20% above non-irradiated hemisphere. Cyclosporine increased ^{11}C-carvedilol uptake dose-dependently in both hemispheres, but more in the irradiated hemisphere. Fractionated irradiation resulted in a lost P-gp expression 10 days after start irradiation, which coincided with increased ^{11}C-carvedilol uptake. P-gp expression decreased between day 15 and 20 after single dose irradiation, and increased again thereafter. Rat brain irradiation resulted in a temporary decreased P-gp function.

These studies indicate that radiotherapy influences both P-gp expression and P-gp function.

All the above examples illustrate that *in vivo* imaging of the function of ABC transporters involved in MDR in tumors and BBB is possible. The impact for the clinic is however currently minor.

Imaging of molecular targets for molecular targeted drugs that could sensitize tumor cells to MDR related chemotherapeutic drugs

Over the last decade numerous new anticancer agents have entered the clinic. Many of these agents are specifically designed to target receptors, intracellular proteins or ligands which are over expressed by tumor cells. Two examples which have had a big impact clinically are the monoclonal antibodies trastuzumab (Herceptin®) and bevacizumab (Avastin®), both improving patient outcome when combined with MDR related chemotherapeutic drugs. Trastuzumab binds to the HER2/neu receptor, bevacizumab binds to VEGF-A. Combining trastuzumab with paclitaxel leads to increased progression free survival and overall survival in metastatic breast cancer [21]. Combining bevacizumab with paclitaxel increases progression free survival in metastatic breast cancer [22]. Despite this progress, there still remain a significant number of patients which do not respond to these agents or become resistant. Potentially, visualizing their specific molecular drug targets in the tumor can function as biomarkers to support treatment decision for the individual patient. HER2 imaging and VEGF imaging are discussed as examples of this new imaging approach.

HER2 imaging

The HER2 antibody trastuzumab potentiates the antitumor effect of the MDR drugs, the taxanes. As a consequence, trastuzumab reduces taxane resistance. For antitumor efficacy of trastuzumab, the HER2 gene has to be amplified, as is the case in about 20-30% of the breast tumors [23]. The HER2 tumor expression can vary during the treatment of a patient and can differ across metastatic lesions within a patient [24]. Therefore, there is a need for methods that are able to assess the HER2 status repeatedly, preferable in all lesions and non-invasively. Molecular imaging of the HER2 receptor could serve this aim. In addition to this diagnostic purpose, HER2 imaging could also be used as an early predictive marker for the tumor response to HER2 targeted or HER2 degrading therapies.

HER2 imaging starts with selecting a suitable HER2 targeted molecule. Currently available HER2 targeted molecules includes full length monoclonal antibodies, Fab-fragments, $F(ab')_2$-fragments, diabodies, minibodies, affibodies, scFv-Fc and peptides. In order to image the HER2 targeted molecule, and thus the receptor, labeling with a radionuclide tracer or fluorescent dye must first be accomplished. The label should be suitable for the proposed

imaging technique: PET, SPECT, MRI or optical imaging [25]. For radio-labeling purposes, the physical half-life of the isotope must suit the biological half-life of the HER2 targeting molecule to reduce tumor-to-background ratios and to allow imaging at the optimal time-point. This implicates that full-length monoclonal antibodies are mostly radiolabeled with long-lived isotopes and the smaller HER2 targeting molecules, which have a more rapid clearance, are radiolabeled with shorter-lived isotopes. Full-length HER2 monoclonal antibodies have been radiolabeled with $^{125/131}$I, ^{111}In and ^{99m}Tc for HER2 SPECT/gamma camera imaging [26-32] and with ^{124}I, ^{86}Y, ^{76}Br and ^{89}Zr for HER2 PET imaging [33-38]. The smaller HER2 targeting antibody fragments, proteins and peptides have been labeled with ^{111}In, ^{125}I and ^{99m}Tc for HER2 SPECT/gamma camera imaging [39-45] and with ^{18}F, ^{68}Ga, ^{64}Cu, ^{124}I and ^{76}Br for HER2 PET imaging [46-51].

We have imaged HER2 in patients using ^{111}In-trastuzumab (Fig.1A). SPECT-imaging with ^{111}In-trastuzumab was able to visualize previously unidentified lesions in 13 out of 15 patients [52]. Since PET-imaging provides a higher spatial resolution, a better signal-to-noise ratio and is more quantitative than SPECT, we currently are evaluating the use of ^{89}Zr-trastuzumab for clinical PET-imaging of the HER2-receptor in metastatic breast cancer. Preliminary data of this clinical evaluation show excellent tumor uptake of ^{89}Zr-trastuzumab and high resolution images [38].

Smith-Jones et al preclinically studied the HER2 response of the HER2 targeted therapy with 17-allylamino-17-demethoxygeldanamycin (17-AAG; tanespimycin), a Heat Shock Protein 90 (HSP90)-inhibitor [48]. HSPs are molecular chaperones involved in maintaining the conformation, stability, cellular localization and activity of several key oncogenic client proteins [53]. Client proteins of HSP90 include the key regulator of VEGF expression HIF-1α, HER2, hormone receptors and others [53]. Treatment with HSP90 inhibitors leads to HER2 degradation. The pharmacodynamics of HER2 degradation induced by 17-AAG was visually and quantitatively evaluated by PET imaging with a ^{68}Ga labeled F(ab')$_2$ fragment of trastuzumab. Results show that PET imaging with this fragment was able to quantify the HER2 response after 48 h as the pharmocodynamic effect of 17-AAG [54]. Secondly, the ^{68}Ga labeled F(ab')$_2$ PET visualized HER2 response to 17-AAG was compared with response measurement by ^{18}FDG-PET [55], which visualizes glucose metabolism and is being used for detection, staging and response monitoring in breast cancer patients [56]. Quantification of the ^{68}Ga labeled F(ab')$_2$ PET-data showed a 70% reduction in tracer uptake 24 h after treatment with 17-AAG. With ^{18}FDG-PET there was no significant difference in tumor uptake between 17-AAG treated and control mice in the 3 weeks post treatment.

The clinical success of trastuzumab is limited by resistance for this drug, which can among others be due to alterations in receptor-antibody interaction. HER2 imaging could therefore potentially be used to elucidate altered receptor-antibody interaction in trastuzumab resistant tumors [57].

VEGF level imaging

The development of vascular supply, the so-called angiogenesis, is important in the development and growth of tumors. Without a vascular network, tumors cannot grow above several mm^3 in size [58,59]. Newly formed blood vessels supply the tumor with nutrients and oxygen, disposal of metabolic waste products and provide route for metastatic spreading. Compared to normal blood vessels, tumor vasculature is structurally and functionally abnormal, presumably to an imbalance of pro-angiogenic and anti-angiogenic growth factors produced by tumor cells [60,61]. This abnormality causes interstitial hypertension, hypoxia and acidosis, which makes tumors more aggressive. This is associated with chemo- and radiotherapy resistance [60,62,63].

One of the most important factors involved in angiogenesis is vascular endothelial growth factor (VEGF). VEGF exists of at least five different isoforms A-E. VEGF-A (hereafter referred as VEGF) is one of the most important growth factors involved in tumor angiogenesis with different splice variants like VEGF 121, 145, 165, 189 and 206. $VEGF_{121}$ is freely soluble, whereas $VEGF_{165}$ is secreted, though a significant fraction remains localized to the extra cellular matrix, such as $VEGF_{189}$ and $VEGF_{206}$ [64]. The actions of VEGF are transmitted by the VEGF-receptors VEGFR-1, VEGFR-2 (KDR/Flk-1), being the most abundant in tumor angiogenesis, and VEGFR-3 (Flt-4) [65]. The VEGFRs are tyrosine kinase mediated transmembrane receptors, present on endothelial cells, circulating endothelial progenitor cells and both epithelial and mesenchymal tumor cells [66]. The role of these receptors on the surface of tumor cells is not completely elucidated. Physiologically, large amounts of VEGF are stored in blood platelets and only small amounts are freely soluble [67]. In tumors there is an unproportional upregulation of VEGF production which leads to locally high VEGF levels mainly located in the extracellular matrix. All this leads to paracrine effects in the tumor tissue, a pro-angiogenic status, thus altering the micro-environment of the tumor. This results in increased tumor growth and increased interstitial pressure which leads to hypoxia and elevated production of ongogenic transcription factors, such as hypoxia inducible factor (HIF) [68]. HIF-1α is one of the cellular key regulators of the transcription of VEGF. Furthermore, HIF is a potent transcription factor involved in the regulation and activation of multiple oncogenic pathways, increased glucose uptake, increased homing of endothelial

progenitor cells and pericyte progenitor cells. It is also involved in chemotherapeutic drug resistance, for example, by increased transcription of the MDR-1 gene, resulting in increased P-gp expression [69,70].

Despite the fact that the importance of tumor angiogenesis in tumor progression was already postulated decades ago, it was only recently that clinical advancement has been made [71,72]. The first clinical breakthrough came from bevacizumab, a humanized monoclonal antibody which neutralizes all isoforms of VEGF-A. In patients with metastatic breast, the addition of bevacizumab to the MDR associated drug paclitaxel leads to an increased response rate and increased progression free survival, and thus decreasing drug resistance [22]. One of the proposed working mechanisms of this anti-VEGF targeted therapy is that treatment results in vessel normalization and thereby increased perfusion and a decline of interstitial fluid pressure, which coincides with an increased penetration and efficacy of chemotherapeutic drugs [62].

Other anti-angiogenic strategies which have shown clinical efficacy are tyrosine kinase inhibitors (TKIs), which block the signal transduction of VEGFRs on endothelial and tumor cells. More recently, progress has been made in the inhibition of intracellular targets like HSP90 and the mammalian target of rapamycin (mTOR) pathway. HSP90 inhibition reduces angiogenesis through HIF-1α inhibition resulting in a reduction of VEGF secretion and other HIF-1α activated genes [73-75]. For example, a recent study demonstrated that the inhibition by means of 17-AAG, reduced VEGF secretion by 60% under hypoxic conditions in pancreatic cancer cells leading to e.a. decreased mean vessel density (MVD) in a xenograft model [74]. The mTOR pathway plays a key role in regulating cancer cell proliferation, tumor growth and angiogenesis though altering HIF-1 and VEGF expression by its upstream pathways such as phosphoinositide 3-kinases (PI3Ks), AKT and extracellular signal-regulated kinases (ERKs) [76]. Treatment with RAD001, an oral mTOR inhibitor, resulted in decreased VEGF expression and decreased MVD in a transgenic mouse model of ovarian cancer [77]. Furthermore, the mTOR pathway is involved in specific drug resistance mechanism. For example, upstream PI3K activation leads to MRP1 expression and subsequent chemoresistance in advanced prostate cancer cells [78]. These examples nicely demonstrate the close and complex interaction between classic chemotherapeutic MDR, angiogenesis and tumor progression. Therefore, new anti-angiogenic therapies, such as HSP90 and mTOR inhibition, could facilitate to overcome resistance to classic chemotherapeutics and targeted therapies.

To select patients who benefit from this targeted therapy, and to follow up new treatment regimes, molecular imaging of transcription factors and key proteins of these pathways, by

using specific molecular imaging probes, is of great interest. VEGF is an interesting example key protein. It is an important down stream protein produced as a result of multiple processes (hypoxia ea), activation of growth factor receptors (EGFR, HER eo) and intracellular proteins (HIF-1α, mTor etc.). Therefore, VEGF could potentially serve as a representative biomarker for early prediction of these targeted therapies. Furthermore, VEGF imaging could give insight in drug resistance. For example, acquired resistance in a breast cancer xenograft model for trastuzumab was associated with increased expression of VEGF [79]. Treatment with bevacizumab in this setting, and thus lowering the increased VEGF levels, could overcome resistance for trastuzumab which resulted in delayed tumor progression.

To date, several radiolabeled anti-VEGF antibodies and Fab-fragments have been used for the development of VEGF imaging: VG76e, HumMV833, bevacizumab and ranibizumab [80,81,81,82]. ^{125}I- and ^{124}I-labeled VG76e, an IgG1 mouse monoclonal anti-VEGF antibody which recognizes the 121, 165 and 189 isoforms of human VEGF-A, showed specific tumor targeting in a human fibrosarcoma xenograft mice model. Jayson et al. used ^{124}I-HuMV833, a humanized monoclonal IgG4$_k$ antibody that binds VEGF$_{121}$ and VEGF$_{165}$, to perform PET-imaging studies in patients with various progressive solid tumors (82). Tumor uptake of ^{124}I-HuMV833 was highly variable between and within patients. For example, there was high uptake of ^{124}I-HuMV833 in an ovarian tumor and low uptake in a poorly vascularized metastasis in a colon cancer patient [81]. These differences are very likely to present the variation VEGF secretion among tumor types and lesions. Radiolabeled bevacizumab showed specific tumor uptake in a human ovarian xenograft model (Fig. 1B) [80]. MicroPET imaging using ^{89}Zirconium (^{89}Zr) labeled bevacizumab showed clear tumor localization 72 h post injection with maximal uptake 168 h post injection [80]. Uptake could be quantified non-invasively, allowing follow-up of VEGF secretion during therapy. Comparable results were seen using ^{89}Zr- and ^{18}Fluor (^{18}F) labeled ranibizumab, a Fab-fragment binding to all VEGF-A isoforms. Though, due to fast distribution and clearance of the Fab-fragment images could be made earlier; already 3 h post injection of the tracer, though absolute tumor uptake is lower compared to bevacizumab [83]. This tracer could be attractive to follow up rapid changes of VEGF secretion following therapy. Preliminary clinical SPECT imaging using ^{111}indium (^{111}In) labeled bevacizumab revealed tumor lesions in both recurrent melanoma and metastatic colon cancer patients [84]. Future studies, both pre- as well as clinically can potentially further elucidate the role of VEGF-imaging in the assessment of drug resistance for chemotherapeutics and the response evaluation of new molecular targeted therapies. All this could lead to more patient tailored therapy.

Conclusion

To overcome MDR and increase the efficacy of chemotherapy new targeted therapies have to be added. At this moment, blockade of specific growth factor receptors, intracellular targets and tyrosine kinase signaling has increased the efficacy of classic chemotherapy in several cancer types. However, despite this success a lot of patients do not benefit of the addition of these therapies. To select patients up front and follow up treatment response, new tracers and imaging modalities which represent changes in intra- and extra cellular tumor targets, antigens located in the extra cellular matrix or at the blood vessels of tumors during therapy might support treatment follow-up. As indicated, growth factor receptors present on the membrane of tumor cells, like HER2, EGFR etc, are suitable candidates for this. Another approach is to use a downstream product whose transcription is increased in MDR and by other oncogenic processes. As indicated, VEGF is such a target which could serve as a specific read-out modality for MDR and the response of new targeted therapies. Besides intact mAb molecules like trastuzumab and bevacizumab (molecular weight, 150 kDa), mAb fragments and engineered variants are also used, like F(ab)2, F(ab), Fab, single chain Fv (scFv), and the covalent dimers scFv2, diabodies, and minibodies (molecular weights ranging from 25 to 100 kDa), as well as several types of protein therapeutics based on nontraditional scaffolds, like, for example, domain antibodies, affibodies, nanobodies, and anticalins could be used for this purpose [85]. During the development of these tracers, one of the main goals should be to observe whether baseline values and/or changes during therapy, correspond with patient outcome and ultimately patient survival. All this will lead to more patient tailored therapy.

Acknowledgments:

Supported by a personal grant (W.B. Nagengast) and grant RUG 2007-3739 of the Dutch Cancer Society.

References

1. Hait, W. N. & Yang, J. M. Clinical management of recurrent breast cancer: development of multidrug resistance (MDR) and strategies to circumvent it. *Semin. Oncol.* 32, S16-S21 (2005).
2. Pusztai, L. *et al.* Phase II study of tariquidar, a selective P-glycoprotein inhibitor, in patients with chemotherapy-resistant, advanced breast carcinoma. *Cancer* 104, 682-691 (2005).
3. Hendrikse, N. H., Franssen, E. J., van der Graaf, W. T., Vaalburg, W. & De Vries, E. G. Visualization of multidrug resistance *in vivo*. *Eur. J. Nucl. Med.* 26, 283-293 (1999).
4. Kostakoglu, L. *et al.* Clinical validation of the influence of P-glycoprotein on technetium-99m-sestamibi uptake in malignant tumors. *J. Nucl. Med.* 38, 1003-1008 (1997).
5. Ciarmiello, A. *et al.* Tumor clearance of technetium 99m-sestamibi as a predictor of response to neoadjuvant chemotherapy for locally advanced breast cancer. *J. Clin. Oncol.* 16, 1677-1683 (1998).
6. Ho, Y. J. *et al.* A trial of single photon emission computed tomography of the liver with technetium-99m tetrofosmin to detect hepatocellular carcinoma. *Anticancer Res.* 23, 1743-1746 (2003).
7. Wang, H., Chen, X. P. & Qiu, F. Z. Correlation of expression of multidrug resistance protein and messenger RNA with 99mTc-methoxyisobutyl isonitrile (MIBI) imaging in patients with hepatocellular carcinoma. *World J. Gastroenterol.* 10, 1281-1285 (2004).
8. Kao, C. H. *et al.* Paclitaxel-Based chemotherapy for non-small cell lung cancer: predicting the response with 99mTc-tetrofosmin chest imaging. *J. Nucl. Med.* 42, 17-20 (2001).
9. Yeh, J. J. *et al.* Technetium-99m tetrofosmin SPECT predicts chemotherapy response in small cell lung cancer. *Tumour. Biol.* 24, 151-155 (2003).
10. Hsu, W. H. *et al.* Predicting chemotherapy response to paclitaxel-based therapy in advanced non-small-cell lung cancer (stage IIIb or IV) with a higher T stage (> T2). Technetium-99m methoxyisobutylisonitrile chest single photon emission computed tomography and P-glycoprotein express ion. *Oncology* 63, 173-179 (2002).
11. Kim, I. J. *et al.* Determination and prediction of P-glycoprotein and multidrug-resistance-related protein expression in breast cancer with double-phase technetium-99m sestamibi scintimammography. Visual and quantitative analyses. *Oncology* 70, 403-410 (2006).
12. Hendrikse, N. H., De Vries, E. G., Franssen, E. J., Vaalburg, W. & van der Graaf, W. T. *In vivo* measurement of [11C]verapamil kinetics in human tissues. *Eur. J. Clin. Pharmacol.* 56, 827-829 (2001).
13. Guhlmann, A. *et al.* Noninvasive assessment of hepatobiliary and renal elimination of cysteinyl leukotrienes by positron emission tomography. *Hepatology* 21, 1568-1575 (1995).
14. Hendrikse, N. H. *et al. In vivo* imaging of hepatobiliary transport function mediated by multidrug resistance associated protein and P-glycoprotein. *Cancer Chemother. Pharmacol.* 54, 131-138 (2004).
15. van Eerd, J. E., de Geus-Oei, L. F., Oyen, W. J., Corstens, F. H. & Boerman, O. C. Scintigraphic imaging of P-glycoprotein expression with a radiolabelled antibody. *Eur. J. Nucl. Med. Mol. Imaging* 33, 1266-1272 (2006).
16. Hendrikse, N. H. *et al.* Complete *in vivo* reversal of P-glycoprotein pump function in the blood-brain barrier visualized with positron emission tomography. *Br. J. Pharmacol.* 124, 1413-1418 (1998).
17. Hendrikse, N. H. *et al.* A new *in vivo* method to study P-glycoprotein transport in tumors and the blood-brain barrier. *Cancer Res.* 59, 2411-2416 (1999).
18. Syvanen, S. *et al.* Duration and degree of cyclosporin induced P-glycoprotein inhibition in the rat blood-brain barrier can be studied with PET. *Neuroimage.* 32, 1134-1141 (2006).
19. Mima, T., Toyonaga, S., Mori, K., Taniguchi, T. & Ogawa, Y. Early decrease of P-glycoprotein in the endothelium of the rat brain capillaries after moderate dose of irradiation. *Neurol. Res.* 21, 209-215 (1999).
20. Bart, J. *et al.* Irradiation of rat brain reduces P-glycoprotein expression and function. *Br. J. Cancer* 97, 322-326 (2007).

21. Slamon, D. J. *et al.* Use of chemotherapy plus a monoclonal antibody against HER2 for metastatic breast cancer that overexpresses HER2. *N. Engl. J. Med.* 344, 783-792 (2001).
22. Miller, K. *et al.* Paclitaxel plus bevacizumab versus paclitaxel alone for metastatic breast cancer. *N. Engl. J. Med.* 357, 2666-2676 (2007).
23. Hayes, D. F. *et al.* HER2 and response to paclitaxel in node-positive breast cancer. *N. Engl. J. Med.* 357, 1496-1506 (2007).
24. Zidan, J. *et al.* Comparison of HER-2 overexpression in primary breast cancer and metastatic sites and its effect on biological targeting therapy of metastatic disease. *Br. J. Cancer* 93, 552-556 (2005).
25. Cai, W., Niu, G. & Chen, X. Multimodality imaging of the HER-kinase axis in cancer. *Eur. J. Nucl. Med. Mol. Imaging* 35, 186-208 (2008).
26. De, S. K. *et al.* Radiolabeled antibody targeting of the HER-2/neu oncoprotein. *Cancer Res.* 52, 1916-1923 (1992).
27. Zalutsky, M. R. *et al.* Radioiodinated antibody targeting of the HER-2/neu oncoprotein: effects of labeling method on cellular processing and tissue distribution. *Nucl. Med. Biol.* 26, 781-790 (1999).
28. Tsai, S. W. *et al.* Biodistribution and radioimmunotherapy of human breast cancer xenografts with radiometal-labeled DOTA conjugated anti-HER2/neu antibody 4D5. *Bioconjug. Chem.* 11, 327-334 (2000).
29. Lub-De Hooge, M. N. *et al.* Preclinical characterisation of 111In-DTPA-trastuzumab. *Br. J. Pharmacol.* 143, 99-106 (2004).
30. Allan, S. M. *et al.* Radioimmunolocalisation in breast cancer using the gene product of c-erbB2 as the target antigen. *Br. J. Cancer* 67, 706-712 (1993).
31. Persson, M. *et al.* [(177)Lu]pertuzumab: experimental studies on targeting of HER-2 positive tumour cells. *Eur. J. Nucl. Med. Mol. Imaging* 32, 1457-1462 (2005).
32. Meenakshi, A., Kumar, R. S., Ganesh, V. & Kumar, N. S. Preliminary study on radioimmunodiagnosis of experimental tumor models using technetium-99m-labeled anti-C-erbB-2 monoclonal antibody. *Tumori* 88, 507-512 (2002).
33. Bakir, M. A. *et al.* c-erbB2 protein overexpression in breast cancer as a target for PET using iodine-124-labeled monoclonal antibodies. *J. Nucl. Med.* 33, 2154-2160 (1992).
34. Garmestani, K., Milenic, D. E., Plascjak, P. S. & Brechbiel, M. W. A new and convenient method for purification of 86Y using a Sr(II) selective resin and comparison of biodistribution of 86Y and 111In labeled Herceptin. *Nucl. Med. Biol.* 29, 599-606 (2002).
35. Bruskin, A. *et al.* Radiobromination of monoclonal antibody using potassium [76Br] (4 isothiocyanatobenzyl-ammonio)-bromo-decahydro-closo-dodecaborate (Bromo-DABI). *Nucl. Med. Biol.* 31, 205-211 (2004).
36. Winberg, K. J., Persson, M., Malmstrom, P. U., Sjoberg, S. & Tolmachev, V. Radiobromination of anti-HER2/neu/ErbB-2 monoclonal antibody using the p-isothiocyanatobenzene derivative of the [76Br] undecahydro-bromo-7,8-dicarba-nido-undecaborate(1-) ion. *Nucl. Med. Biol.* 31, 425-433 (2004).
37. Mume, E. *et al.* Radiobromination of humanized anti-HER2 monoclonal antibody trastuzumab using N-succinimidyl 5-bromo-3-pyridinecarboxylate, a potential label for immunoPET. *Nucl. Med. Biol.* 32, 613-622 (2005).
38. E.C.F Dijkers *et al.* Characterization of ^{89}Zr-trastuzumab for clinical HER2 immunoPET imaging. Vol 25, No. 18S (June 20 Supplement), 2007: 3508. 2007. Proc. Am. Soc. Clin. Oncology. Ann. Meeting. Ref Type: Generic
39. Tang, Y. *et al.* Imaging of HER2/neu-positive BT-474 human breast cancer xenografts in athymic mice using (111)In-trastuzumab (Herceptin) Fab fragments. *Nucl. Med. Biol.* 32, 51-58 (2005).
40. Tang, Y. *et al.* Imaging of HER2/neu expression in BT-474 human breast cancer xenografts in athymic mice using [(99m)Tc]-HYNIC-trastuzumab (Herceptin) Fab fragments. *Nucl. Med. Commun.* 26, 427-432 (2005).
41. Adams, G. P. *et al.* Highly specific *in vivo* tumor targeting by monovalent and divalent forms of 741F8 anti-c-erbB-2 single-chain Fv. *Cancer Res.* 53, 4026-4034 (1993).

42. Adams, G. P. *et al*. Enhanced tumor specificity of 741F8-1 (sFv')2, an anti-c-erbB-2 single-chain Fv dimer, mediated by stable radioiodine conjugation. *J. Nucl. Med*. 36, 2276-2281 (1995).
43. Adams, G. P. *et al.* Prolonged *in vivo* tumour retention of a human diabody targeting the extracellular domain of human HER2/neu. *Br. J. Cancer* 77, 1405-1412 (1998).
44. Orlova, A. *et al*. Tumor imaging using a picomolar affinity HER2 binding affibody molecule. *Cancer Res. 66*, 4339-4348 (2006).
45. Tran, T. *et al.* (99m)Tc-maEEE-Z(HER2:342), an Affibody molecule-based tracer for the detection of HER2 expression in malignant tumors. *Bioconjug. Chem.* 18, 1956-1964 (2007).
46. Cheng, Z. *et al.* Small-animal PET imaging of human epidermal growth factor receptor type 2 expression with site-specific 18F-labeled protein scaffold molecules. *J. Nucl. Med.* 49, 804-813 (2008).
47. Kramer-Marek, G. *et al.* [18F]FBEM-Z(HER2:342)-Affibody molecule-a new molecular tracer for *in vivo* monitoring of HER2 expression by positron emission tomography. *Eur. J. Nucl. Med. Mol. Imaging* 35, 1008-1018 (2008).
48. Smith-Jones, P. M. *et al*. Imaging the pharmacodynamics of HER2 degradation in response to Hsp90 inhibitors. *Nat. Biotechnol.* 22, 701-706 (2004).
49. Olafsen, T. *et al.* Optimizing radiolabeled engineered anti-p185HER2 antibody fragments for *in vivo* imaging. *Cancer Res*. 65, 5907-5916 (2005).
50. Robinson, M. K. *et al*. Quantitative immuno-positron emission tomography imaging of HER2-positive tumor xenografts with an iodine-124 labeled anti-HER2 diabody. *Cancer Res*. 65, 1471-1478 (2005).
51. Mume, E. *et al*. Evaluation of ((4-hydroxyphenyl)ethyl)maleimide for site-specific radiobromination of anti-HER2 affibody. *Bioconjug. Chem.* 16, 1547-1555 (2005).
52. Perik, P. J. *et al*. Indium-111-labeled trastuzumab scintigraphy in patients with human epidermal growth factor receptor 2-positive metastatic breast cancer. *J. Clin. Oncol.* 24, 2276-2282 (2006).
53. Neckers, L. Heat shock protein 90: the cancer chaperone. *J. Biosci*. 32, 517-530 (2007).
54. Smith-Jones, P. M. *et al*. Imaging the pharmacodynamics of HER2 degradation in response to Hsp90 inhibitors. *Nat. Biotechnol.* 22, 701-706 (2004).
55. Smith-Jones, P. M., Solit, D., Afroze, F., Rosen, N. & Larson, S. M. Early tumor response to Hsp90 therapy using HER2 PET: comparison with 18F-FDG PET. *J. Nucl. Med*. 47, 793-796 (2006).
56. Eubank, W. B. & Mankoff, D. A. Evolving role of positron emission tomography in breast cancer imaging. *Semin. Nucl. Med*. 35, 84-99 (2005).
57. Nahta, R., Yu, D., Hung, M. C., Hortobagyi, G. N. & Esteva, F. J. Mechanisms of disease: understanding resistance to HER2-targeted therapy in human breast cancer. *Nat. Clin. Pract. Oncol.* 3, 269-280 (2006).
58. Folkman, J. What is the evidence that tumors are angiogenesis dependent? *J. Natl. Cancer Inst.* 82, 4-6 (1990).
59. Folkman, J. & Klagsbrun, M. Angiogenic factors. *Science* 235, 442-447 (1987).
60. Jain, R. K. Lessons from multidisciplinary translational trials on anti-angiogenic therapy of cancer. *Nat. Rev. Cancer* 8, 309-316 (2008).
61. Varey, A. H. *et al*. VEGF(165)b, an antiangiogenic VEGF-A isoform, binds and inhibits bevacizumab treatment in experimental colorectal carcinoma: balance of pro- and antiangiogenic VEGF-A isoforms has implications for therapy. *Br. J. Cancer* (2008).
62. Jain, R. K., Duda, D. G., Clark, J. W. & Loeffler, J. S. Lessons from phase III clinical trials on anti-VEGF therapy for cancer. *Nat. Clin. Pract. Oncol.* 3, 24-40 (2006).
63. Willett, C. G. *et al.* Direct evidence that the VEGF-specific antibody bevacizumab has antivascular effects in human rectal cancer. *Nat. Med.* 10, 145-147 (2004).
64. Park, J. E., Keller, G. A. & Ferrara, N. The vascular endothelial growth factor (VEGF) isoforms: differential deposition into the subepithelial extracellular matrix and bioactivity of extracellular matrix-bound VEGF. *Mol. Biol. Cell* 4, 1317-1326 (1993).

65. Mishani, E. *et al.* Novel carbon-11 labeled 4-dimethylamino-but-2-enoic acid [4-(phenylamino)-quinazoline-6-yl]-amides: potential PET bioprobes for molecular imaging of EGFR-positive tumors. *Nucl. Med. Biol.* 31, 469-476 (2004).
66. Holliger, P. & Hudson, P. J. Engineered antibody fragments and the rise of single domains. *Nat. Biotechnol.* 23, 1126-1136 (2005).
67. Nguyen, D. M. *et al.* Enhancement of paclitaxel-mediated cytotoxicity in lung cancer cells by 17-allylamino geldanamycin: in vitro and *in vivo* analysis. *Ann. Thorac. Surg.* 72, 371-378 (2001).
68. Ferrara, N. Vascular endothelial growth factor: basic science and clinical progress. *Endocr. Rev.* 25, 581-611 (2004).
69. Comerford, K. M. *et al.* Hypoxia-inducible factor-1-dependent regulation of the multidrug resistance (MDR1) gene. *Cancer Res.* 62, 3387-3394 (2002).
70. Liu, L. *et al.* Hypoxia-inducible factor-1 alpha contributes to hypoxia-induced chemoresistance in gastric cancer. *Cancer Sci.* 99, 121-128 (2008).
71. Cai, W. *et al.* PET imaging of colorectal cancer in xenograft-bearing mice by use of an 18F-labeled T84.66 anti-carcinoembryonic antigen diabody. *J. Nucl. Med.* 48, 304-310 (2007).
72. Hurwitz, H. *et al.* Bevacizumab plus irinotecan, fluorouracil, and leucovorin for metastatic colorectal cancer. *N. Engl. J. Med.* 350, 2335-2342 (2004).
73. Lang, S. A. *et al.* Inhibition of heat shock protein 90 impairs epidermal growth factor-mediated signaling in gastric cancer cells and reduces tumor growth and vascularization *in vivo*. *Mol. Cancer Ther.* 6, 1123-1132 (2007).
74. Lang, S. A. *et al.* Targeting heat shock protein 90 in pancreatic cancer impairs insulin-like growth factor-I receptor signaling, disrupts an interleukin-6/signal-transducer and activator of transcription 3/hypoxia-inducible factor-1alpha autocrine loop, and reduces orthotopic tumor growth. *Clin. Cancer Res.* 13, 6459-6468 (2007).
75. Eccles, S. A. *et al.* NVP-AUY922: a novel heat shock protein 90 inhibitor active against xenograft tumor growth, angiogenesis, and metastasis. *Cancer Res.* 68, 2850-2860 (2008).
76. Jiang, B. H. & Liu, L. Z. Role of mTOR in anticancer drug resistance: Perspectives for improved drug treatment. *Drug Resist. Updat.* (2008).
77. Mabuchi, S. *et al.* RAD001 (Everolimus) delays tumor onset and progression in a transgenic mouse model of ovarian cancer. *Cancer Res.* 67, 2408-2413 (2007).
78. Lee, J. T., Jr., Steelman, L. S. & McCubrey, J. A. Phosphatidylinositol 3'-kinase activation leads to multidrug resistance protein-1 expression and subsequent chemoresistance in advanced prostate cancer cells. *Cancer Res.* 64, 8397-8404 (2004).
79. du Manoir, J. M. *et al.* Strategies for Delaying or Treating *In vivo* Acquired Resistance to Trastuzumab in Human Breast Cancer Xenografts. *Clin. Cancer Res.* 12, 904-916 (2006).
80. Nagengast, W. B. *et al. In vivo* VEGF imaging with radiolabeled bevacizumab in a human ovarian tumor xenograft. *J. Nucl. Med.* 48, 1313-1319 (2007).
81. Jayson, G. C. *et al.* Molecular imaging and biological evaluation of HuMV833 anti-VEGF antibody: implications for trial design of antiangiogenic antibodies. *J. Natl. Cancer Inst.* 94, 1484-1493 (2002).
82. Collingridge, D. R. *et al.* The development of [(124)I]iodinated-VG76e: a novel tracer for imaging vascular endothelial growth factor *in vivo* using positron emission tomography. *Cancer Res.* 62, 5912-5919 (2002).
83. Wouter B.Nagengast *et al. In vivo* VEGF imaging with an anti-VEGF Fab-fragment in a human ovarian tumor xenograft model using MicroPET and MicroCT. *Proc. Am. Assoc. Cancer Res. Ann. Meeting.* Abstract 3161 (2008).
84. Nagengast, W. B. *et al.* Towards clinical VEGF imaging using the anti-VEGF antibody bevacizumab and Fab-fragment ranibizumab. *Proc. Am. Soc. Clin. Oncology. Ann. Meeting.* Abstract 3547 (2008) Ref Type: Generic
85. Van Dongen, G. A., Visser, G. W., Lub-De Hooge, M. N., De Vries, E. G. & Perk, L. R. Immuno-PET: a navigator in monoclonal antibody development and applications. *Oncologist.* 12, 1379-1389 (2007).

Chapter 3

Irradiation of rat brain reduces P-glycoprotein expression and function

J. Bart[1,4], W.B. Nagengast[2], R.P. Coppes[3], T.D. Wegman[4], W.T.A. van der Graaf[2], H.J.M. Groen[5], W. Vaalburg[4], E.G.E. de Vries[2], N.H. Hendrikse[4]

Departments of [1]Pathology, [2]Medical Oncology, and [3]Radiation and Stress Cell Biology [4]PET-center and [5]Pulmonology, University of Groningen and University Medical Center Groningen, P.O. Box 30.001, 9700 RB Groningen, The Netherlands

British Journal of Cancer. 2007;97:322-6.

Abstract

Introduction: The blood brain barrier (BBB) hampers delivery of several drugs including chemotherapeutics to the brain. The drug efflux pump P-glycoprotein (P-gp), expressed on brain capillary endothelial cells, is part of the BBB. P-gp expression on capillary endothelium decreases 5 days after brain irradiation, which may reduce P-gp function and increase brain levels of P-gp substrates.

Aim: To elucidate whether radiation therapy reduces P-gp expression and function in the brain.

Methods: Right hemispheres of rats were irradiated with single doses of 2-25 Gy followed by 10 mg/kg of the P-gp substrate cyclosporine A (CsA) intravenously (iv), with once 15 Gy followed by CsA (10, 15 or 20 mg/kg), or with fractionated irradiation (4 x 5 Gy) followed by CsA (10 mg/kg) 5 days later. Additionally four groups of 3 rats received 25 Gy once and were sacrified 10, 15, 20 or 25 days later. The brains were removed and P-gp detected immunohistochemically. P-gp function was assessed by [^{11}C]carvedilol uptake using quantitative autoradiography.

Results: Irradiation increased [^{11}C]carvedilol uptake dose dependently, to a maximum of 20% above non irradiated hemisphere. CsA increased [^{11}C]carvedilol uptake dose dependently in both hemispheres, but more ($p < 0.001$) in the irradiated hemisphere. Fractionated irradiation resulted in a lost P-gp expression 10 days after start irradiation which coincided with increased [^{11}C]carvedilol uptake. P-gp expression decreased between day 15 and 20 after single dose irradiation, and increased again thereafter.

Conclusion: Rat brain irradiation results in a temporary decreased P-gp function.

Introduction

The blood-brain barrier (BBB) is a major impediment for the delivery of several drugs to the brain, including cytotoxic, anti-epileptic, and anti-HIV drugs. The BBB is formed by specialized capillary endothelial cells which have several properties, such as strong tight junctions with a high electrical resistance, absence of fenestrations and presence of efflux-pumps such P-gp and Multidrug resistance associated protein 1 (MRP1). The efflux-pumps are transmembrane proteins, able to actively extrude toxic compounds against a concentration gradient. P-gp effluxes a broad spectrum of natural compounds, among which chemotherapeutic drugs, such as anthracyclines, taxanes, and epipodophyllotoxins [1]. MRP1 transports also a broad spectrum of substrates, but these substrates are transported in conjugation with or co-transported with glucuronide or glutathione. Strategies to pass the BBB include therapies to change the physical properties of the capillary endothelium by hypertonic solutions or by bradykinin analogs [2,3]. Other strategies are directed to inhibition of efflux-pump function. At present the concept of efflux pump inhibition is most frequently studied for P-gp. Studies in rodents have shown that P-gp function can be inhibited with cyclosporin A (CsA) [4-6]. To circumvent toxic side effects of CsA in patients, therapies that influence P-gp function could be utilized, such as radiotherapy. Early effects on brain capillary endothelium were studied by Mima et al [7]. They exposed one brain hemisphere of rats to a single dose of 25 Gray and demonstrated that P-gp expression was decreased in the irradiated hemisphere compared to the non-irradiated hemisphere 5 days after irradiation. It is therefore hypothesized that brain irradiation could also be used to enhance the delivery of P-gp substrates to the brain. P-gp function can be measured with the aid of radiolabelled P-gp substrates, such as [^{11}C]verapamil and [^{11}C]carvedilol [4,6,8-10]. Other approaches like the ^{111}In-labeled 15D3 monoclonal anti-P-gp has been used to visualize P-gp expression [11]. To elucidate whether the decrease in P-gp expression, which was determined with immunohistochemistry using C219, also resulted in a decrease of P-gp function, the latter was assessed by autoradiography using [^{11}C]carvedilol [8]. The right brain hemisphere of rats was irradiated with single fractions of radiotherapy. Furthermore, to mimic clinically relevant palliative whole brain radiotherapy, radiation was also administered in 5 fractions of 4 Gy.

Materials and Methods

Chemicals

Ketamine (Ketanest® 25 mg/ml) was obtained from Parke-Davis (Munich, Germany), medetomidine (Domitor® 10 mg/ml) from Pfizer (New York, NY), CsA (50 mg/ml) in cremophore EL (650 mg/ml) (Sandimmune®/Neoral®) from Novartis (Basel, Switzerland)

and C219, a monoclonal antibody against rat and human P-gp, from Thamer Diagnostica (Uithoorn, The Netherlands). Peroxidase conjugated rabbit-anti-mouse secondary antibody (RAMPO) and peroxidase conjugated goat-anti-rabbit antibody (GARPO) were purchased from DAKO (Glostrup, Denmark), 3.3-diaminobenzidine tetrahydrochloride and isopentane from Sigma (St. Louis, MO), phosphate buffered saline (PBS, 140 mmol/l NaCl, 9 mmol/l Na_2HPO_4, 9 mmol/l NaH_2PO_4; pH=7.4)) and imidazole from Merck (Darmstadt, Germany), and bovine serum albumin (BSA) from Serva Electrophoresis GmbH (Hamburg, Germany). Desmethyl carvedilol was kindly provided by Roche (Mannheim, Germany).

Preparation of [^{11}C]carvedilol

[^{11}C]carvedilol was synthesized as described earlier [12], with some modifications. Desmethyl carvedilol reacts with [^{11}C]methyltriflate, in the presence of K_2CO_3 (4 mg) with kryptofix (4 mg) in 400 µl dry acetone for 5 min at 85°C. The product was purified by HPLC Platinum C18 column (300 x 7.8 mm, Alltech, Deerfield, IL) with a solvent system of 25 mM NaH_2PO_4 (pH 7.6) : MeOH (43:57), flow rate 3 ml/min and UV-detection at 254 nm. After evaporation of the solvent under reduced pressure, [^{11}C]carvedilol was dissolved in 0.3 ml saline.

Animal experiments

Male Wistar rats (HSD CPB wu, Harlan, The Netherlands) weighing 225-275 g, were anesthetized with an intra-peritoneal injection of a mixture of S-ketamine 25 mg/ml and medetomidine 1 mg/ml (5:1, 1 ml/kg). However, the rats who underwent fractionated irradiation were anesthetized with inhaled isoflurane/oxygen. The irradiations were performed with a Philips/Muller MG 300 X-ray machine operated at 200 kV (HVL=1.05 mm Cu) and a beam of 15 mA. The rat was protected against X-rays with a 3 mm lead shield, except the right half of the skull. The right hemisphere was irradiated with a dose rate of 1 Gy/min as measured in air with a calibrated electrometer and ionisation chamber combination (Keithley 35040 + NE 2571) at source to skin distance of 32 cm.

Four groups of rats were formed: Group 1 received 2 (n=4), 5 (n=4), 10 (n=4), 15 (n=4), and 25 Gy (n=5) once, group 2 received 15 Gy once, group 3 received fractionated irradiations (5 days 4 Gy, biological effective dose equal to ≈ 10 Gy when an a/b of 2 for brain is used), and group 4 received 25 Gy (n=12) once. Five days post-irradiation, all rats were anesthetized again with the medetomidine/S-ketamine mixture, and the tail was cannulated. Rats in groups 1 and 3 received 10 mg/kg CsA, to obtain a better signal/noise ratio, and in group 2 10 mg/kg (n=4), 15 mg/kg (n=4), 20 mg/kg (n=4) CsA. CsA was administered

intravenously (iv) after 30 min followed by [^{11}C]carvedilol iv. After 15 min the rats were sacrified by extirpation of the heart and the brain was removed. One part of the brain was fixed in formalin and embedded in paraffin for immunohistochemistry and the second part was frozen in isopentane at -70°C for auto-radiographic assessment. The rats in group 4 were sacrificed 10, 15, 20, and 25 days after irradiation. The removed brains were fixed in formalin, embedded in paraffin, and stained for P-gp.

Animal studies were conducted according to the UKCCCR Guidelines for the care and use of laboratory animals.

Histology/Immunohistochemistry

The embedded brains were cut into 4 μm slices, placed on positively charged glass slides, and dried. The slices were dewaxed in xylene and re-hydrated in serial ethanol washes (100%, 96%, and 70%). Subsequently, they were washed three times in 1% BSA/PBS (pH=7.4). For histology, the slices were stained with hematoxylin/eosin. For immunohistochemistry, the slices were heated three times for 10 min in an autoclave at 115°C in 20 mM blocking reagens (Boehringer Mannheim, Mannheim, Germany) at pH=6.0. Endogenous peroxidase was blocked by incubation with 1% H_2O_2 in PBS during 30 min and a-specific antigens were blocked with 1% rat serum in PBS. The slices were incubated with C219 antibody in 1% BSA/PBS (pH=7.4) for 1 h at room temperature in a humidified chamber. The primary antibody was detected with a peroxidase conjugated rabbit anti-mouse secondary antibody (1:50 diluted in 1% BSA/PBS) followed by incubation with peroxidase labelled goat-anti-rabbit antibody (1:50 diluted in 1% BSA/PBS). As chromagen served 3,3-diaminobenzidine tetrahydrochloride (25 mg) and imidazole (50 mg) in PBS (50 ml) with 50 μl 30% H_20_2. After counterstaining with Mayer's hematoxylin for 2 min, slices were dehydrated through graded ethanols (70%, 96%, and 100%) and mounted with coverslips. Rat liver served as positive controls for P-gp staining. A negative control was made by processing a rat liver slice identical to other slices, but without C219 antibody. Slides were scored by two independent investigators, P-gp expression was assessed semi-quantitatively by using a scale of 0-3 (0: no staining, 1: very weak staining, 2: intermediate staining, 3: strong staining). Strong staining was defined as comparable to the strongest stained slide of all tissue slides. Samples were considered negative if less than 10% of a specific subtype of cells was stained.

Uptake of [^{11}C]carvedilol in the brain

Brain slices of 80 μm thickness were prepared with a Cryo-cut microtome, model 840 (American Optical Corp. Buffalo, NY) at -7°C, placed on object glases and dried at room

temperature. Cyclone™ (Super Sensitive, Packard Instrument Company, Inc., Meriden, CT) storage phosphor screens were exposed to the slices for at least 400 min (20 half lifes of [^{11}C]) and subsequently analyzed with Optiquant analysis software (version 03.00, Packard Instrument Company, Inc., Meriden, CT). To convert from the photo-stimulated-luminescence (PSL) of the exposed screen to Bequerel (Bq), a calibration line was made during each experiment. Regions of interest (ROI) were drawn over the right (irradiated) and the left (non-irradiated) hemisphere in all slices. The ratio of [^{11}C]carvedilol uptake in the right over the left hemisphere was calculated. Exposition in each area was quantified with the aid of a calibration line, converted to Bq, and corrected for injected dose of [^{11}C] carvedilol and body mass [13-15].

Calibration

In each experiment a 1 MBq/ml [^{11}C]carvedilol solution in saline was prepared. The solution was diluted to 714, 625, 500, 250, 125, 55.6, 26.3, and 17.2 kBq/ml and 10 µl of each dilution was loaded on filter paper. The radioactivity (counts per min) of the pieces of filter paper was measured in the gamma counter (Compu Gamma, LKB Wallace, Turku, Finland) for 15 sec, corrected for decay, and converted to Bq. Thereafter the pieces were placed on the phosphor storage screen at the same time as the brain slices and exposed for the same time. The photo-stimulated luminescence (PSL) of the spots from the calibration pieces was measured and corrected for background PSL. The calibration lines were highly reproducible. The mean direction-coefficients of the individual calibration lines was $63x10^3$ ($SD=4.8{\cdot}10^3$, n=10). The equation of the linear relationship between PSL and Bq from the combined calibration line was: PSL=65.3 kBq ($r^2=0.99$). The calibration lines showed a good linearity between the radiation intensity (Bq) and the PSL of the calibration samples in an order of 10 magnitudes.

Statistics

Wilcoxon rank tests were used to examine paired data from right (irradiated) and left (non-irradiated) hemisphere. Univariate ANOVA was used to examine differences in uptake ratio of [^{11}C]carvedilol between groups of rats which were exposed to different single doses of X-rays. (SPSS, version 12). Significance was defined as $p<0.05$.

Results

P-gp function measured by auto-radiographic uptake of [^{11}C]carvedilol in rat brain

The [^{11}C]carvedilol uptake in rat brains, expressed as the ratio between the irradiated hemisphere versus the non-irradiated hemisphere in group 1, 5 days after different doses of irradiation is shown in figure 1. Increasing the radiation dose resulted in a higher [^{11}C] carvedilol uptake ratio (p=0.001). The fitted curve shows a dose dependent increase of the uptake ratio, to 1.20, which means that the increase in [^{11}C]carvedilol uptake by 25 Gy irradiation is 20% compared to the non-irradiated hemisphere. Furthermore, the fitted curve suggests that a plateau of [^{11}C]carvedilol uptake will be reached above 25 Gy. In figure 1 is also depicted that fractionated irradiation for 5 days with 4 Gy (group 3) results in a 13% increased uptake in the irradiated hemisphere, confirming the biological equally effectiveness to ≈ 10 Gy single dose for this end-point.

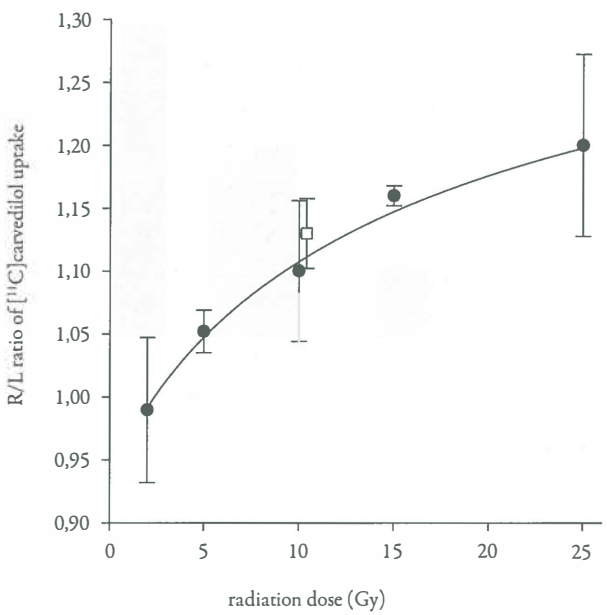

Figure 1. Ratio (± SD) of [^{11}C]carvedilol uptake in right (irradiated) hemisphere/left (non-irradiated) hemisphere (●). Five days after single dose irradiation the R/L ratio increases dose dependently. The fitted curve is a 4 parameter Hill-plot (r^2=0.72). Open square (□) depicts [^{11}C] carvedilol accumulation after 5 x 4 Gy irradiation.

The effect of different doses CsA combined with irradiation was investigated in rats of group 2. Figure 2 shows, that increasing dosages of CsA pre-treatment resulted in a dose dependently increased uptake of [^{11}C]carvedilol, in both the irradiated and the non-irradiated hemisphere, suggesting that maximal P-gp blockade was not reached. In individual rats, irradiation with 15 Gy single dose resulted in a 20-30% higher uptake in the irradiated hemisphere compared with the non-irradiated hemisphere (p=0.02).

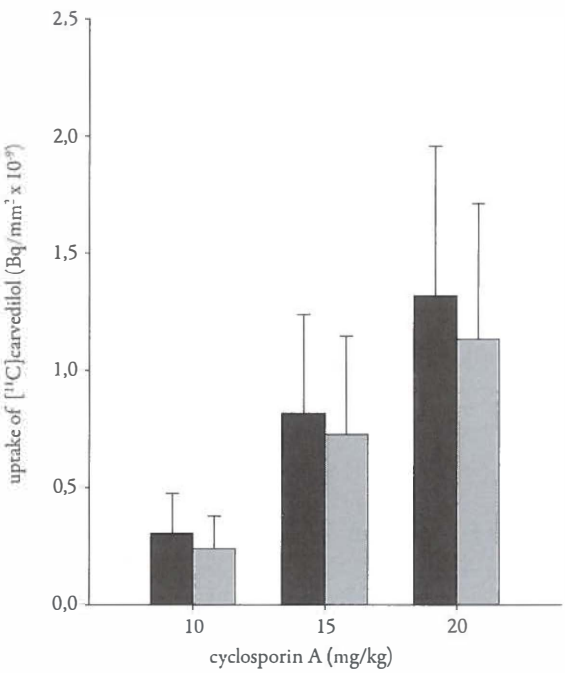

Figure 2. [^{11}C]carvedilol uptake (mean ± SD) in right versus left hemisphere after treatment with different dosages of CsA. Note that in individual rats [^{11}C]carvedilol uptake is 20-30 % higher in the irradiated vs. non-irradiated hemisphere after 15 Gy (p=0.02, Wilcoxon test for paired measures). Interindividual variation masks this effect partly.

= irradiated hemisphere (R), = non-irradiated hemisphere (L)

P-gp expression measured by immunohistochemistry

In rats that underwent single dose irradiation (group 1 and 2), P-gp was equally expressed at the endothelial wall of brain capillaries in the irradiated and non-irradiated hemisphere on day 5. P-gp expression in the rats that underwent single dose irradiation (group 4) is

shown in figure 3. P-gp expression is reduced 15 days after irradiation, and this reduction is maximal after 20 days. Interestingly, P-gp expression restores to the same level as before irradiation between day 20 and day 25. Furthermore, in rats who underwent fractionated dose irradiation (5x4 Gy), P-gp is not detectable immunohistochemically on capillary endothelium 10 days after start of the irradiation (figure 4A versus 4B). As expected other morphological changes of brain tissue were not found at these time points after irradiation.

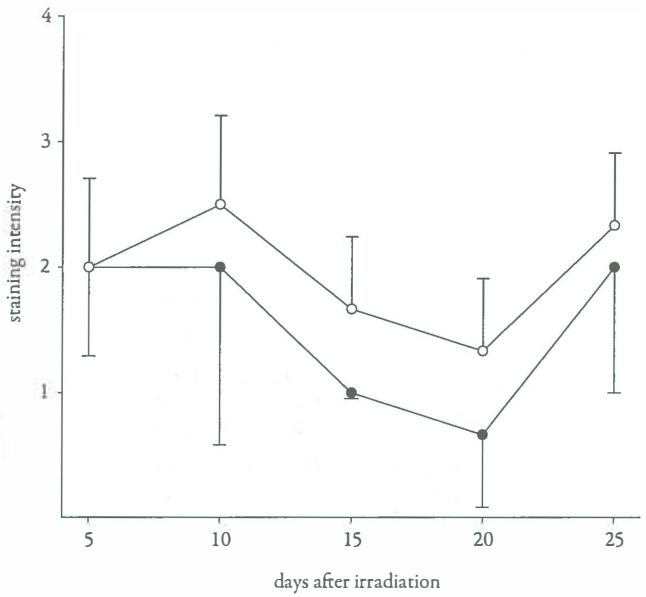

Figure 3. Semiquantitative representation of P-gp expression (mean ± SD) in non-irradiated hemisphere (○) and irradiated hemisphere (●) at different days after irradiation with 25 Gy, single dose.

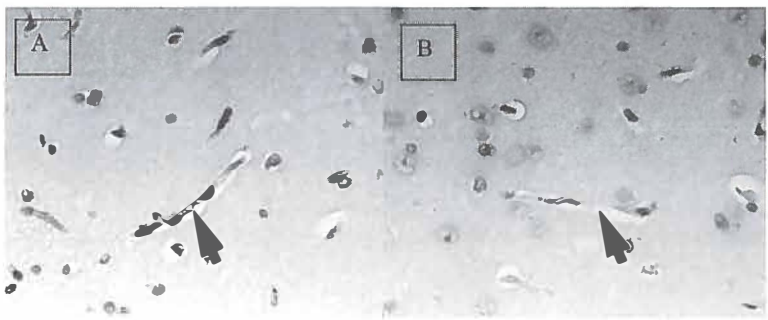

Figure 4. C219 staining (magnification 400 x) of a rat brain. Capillary endothelium stains brown in the non-irradiated hemisphere (A), revealing the presence of P-gp. In the irradiated hemisphere (B), after 5 fractions of 4 Gy, no P-gp is present in the capillary endothelium. Arrows mark capillaries.

Discussion

The present study shows that single and fractionated doses of irradiation of rat brains, increases brain uptake of the P-gp substrate [^{11}C]carvedilol after 5 days. This coincided with a maximal reduction in P-gp expression 20 days after single dose irradiation and a complete loss of P-gp expression 10 days after the start of fractionated irradiation (5x4 Gy). After 25 days P-gp expression returned to the same values, as before radiotherapy.

Five days after irradiation there is a discrepancy between P-gp expression and [^{11}C] carvedilol uptake. [^{11}C]Carvedilol uptake already is higher in the irradiated hemisphere whereas P-gp expression remains immunohistochemically unaffected. In contrast to Mima *et al* [7], who showed a decrease in P-gp expression by immunohistochemistry 5 days after irradiation which was quantified by Western blot (-40%), we observed a decrease in P-gp expression between day 15 and 20 after single dose irradiation. This discrepancy might be explained by the use of different P-gp antibodies. Secondly, evaluation of P-gp function by assessment of [^{11}C]carvedilol uptake is most likely more sensitive compared to semi-quantitative measurement of P-gp expression by immunohistochemistry. Therefore minor changes in P-gp expression levels might be missed by immunohistochemistry shortly after irradiation which can already be detected with quantitative PET autoradiography.

We showed that uptake of the P-gp substrate [^{11}C]carvedilol already increased 5 days after irradiation which could indicate that P-gp function decreases earlier than observed with P-gp expression. Interestingly, P-gp expression disappeared completely five days after fractions

of 4 gray. Uptake of [^{11}C]carvedilol after fractionated irradiation was the same as for the calculated equal biological effective single dose of 10 Gy, indicating that a dose dependent relationship as shown with single dose irradiation could have clinical implications. The impairment of P-gp functionality after single dose irradiation is most likely not solely due to a loss of P-gp expression. It is known that irradiation induces membrane damage, which may result in changes in membrane fluidity and in increased apoptosis of irradiated cells [16-18]. P-gp function is closely related to membrane fluidity status [19,20]. Irradiation induced cell-membrane damage, may therefore indirectly cause a loss of function of transmembrane proteins such as P-gp, but could also apply to other efflux pumps in the BBB such as multidrug-resistance-associated proteins (MRPs), organic anion/cation transporters (OAT/OCT) and glucose transporter 1 (GLUT-1). Apart from a reduction in P-gp expression, reduced P-gp function may also be due to cell membrane damage, which could be another potential explanation for the discrepancy seen in P-gp function and expression of P-gp 5 days post irradiation.

Little is known about early effects of irradiation on the BBB. If an early decrease in P-gp expression and P-gp function in the BBB also occurs in patients after brain irradiation, the results of this study may have clinical implications. Since brain irradiation is frequently applied to patients with brain metastases, it can be speculated that irradiation can lead to a temporary window leading to increased delivery of chemotherapeutic drug to the brain. This could be considered as a tool in the treatment and prevention of brain metastases. P-gp expression in the rat brain is maximally reduced 20 days after radiotherapy and decrease of P-gp function can already be measured at day 5 after irradiation. To elucidate whether P-gp function decreases after irradiation in patients, P-gp mediated kinetics can be measured *in vivo* with PET with e.g. [^{11}C]verapamil as P-gp substrate in patients [4-6,8-10]. Future studies should elucidate if these results can be extrapolated to the human setting. A study in which patients with brain metastases who receive radiotherapy undergo a [^{11}C]carvedilol or [^{11}C]verapamil PET scan before and shortly after radiotherapy would give helpful information. In this way an optimal time schedule of chemotherapy following radiotherapy can potentially be determined.

Acknowledgment

Supported by grant RUG 99-1882 of the Dutch Cancer Society

References

1. Bart, J. *et al.* The blood-brain barrier and oncology: new insights into function and modulation. *Cancer Treat. Rev.* 26, 449-462 (2000).
2. Elliott, P. J. *et al.* Unlocking the blood-brain barrier: a role for RMP-7 in brain tumor therapy. *Exp. Neurol.* 141, 214-224 (1996).
3. Bartus, R. T. *et al.* Controlled modulation of BBB permeability using the bradykinin agonist, RMP-7. *Exp. Neurol.* 142, 14-28 (1996).
4. Hendrikse, N. H. *et al.* A new *in vivo* method to study P-glycoprotein transport in tumors and the blood-brain barrier. *Cancer Res.* 59, 2411-2416 (1999).
5. Hendrikse, N. H. *et al.* Complete *in vivo* reversal of P-glycoprotein pump function in the blood-brain barrier visualized with positron emission tomography. *Br. J. Pharmacol.* 124, 1413-1418 (1998).
6. Syvanen, S. *et al.* Duration and degree of cyclosporin induced P-glycoprotein inhibition in the rat blood-brain barrier can be studied with PET. *Neuroimage.* 32, 1134-1141 (2006).
7. Mima, T., Toyonaga, S., Mori, K., Taniguchi, T. & Ogawa, Y. Early decrease of P-glycoprotein in the endothelium of the rat brain capillaries after moderate dose of irradiation. *Neurol. Res.* 21, 209-215 (1999).
8. Bart, J. *et al.* New positron emission tomography tracer [(11)C]carvedilol reveals P-glycoprotein modulation kinetics. *Br. J. Pharmacol.* 145, 1045-1051 (2005).
9. Takano, A. *et al.* Evaluation of *in vivo* P-glycoprotein function at the blood-brain barrier among MDR1 gene polymorphisms by using 11C-verapamil. *J. Nucl. Med.* 47, 1427-1433 (2006).
10. Bart, J. *et al.* Quantitative assessment of P-glycoprotein function in the rat blood-brain barrier by distribution volume of [11C]verapamil measured with PET. *Neuroimage.* 20, 1775-1782 (2003).
11. van Eerd, J. E., de Geus-Oei, L. F., Oyen, W. J., Corstens, F. H. & Boerman, O. C. Scintigraphic imaging of P-glycoprotein expression with a radiolabelled antibody. *Eur. J. Nucl. Med. Mol. Imaging* 33, 1266-1272 (2006).
12. Doze, P. *et al.* Synthesis and evaluation of radiolabeled antagonists for imaging of beta-adrenoceptors in the brain with PET. *Neurochem. Int.* 40, 145-155 (2002).
13. Sihver, W. *et al.* Methodological aspects for in vitro characterization of receptor binding using 11C-labeled receptor ligands: a detailed study with the benzodiazepine receptor antagonist [11C]Ro 15-1788. *Nucl. Med. Biol.* 24, 723-731 (1997).
14. Murata, T. *et al.* Receptor imaging technique with 11C-labeled receptor ligands in living brain slices: its application to time-resolved imaging and saturation analysis of benzodiazepine receptor using [11C]Ro15-1788. *Neurosci. Res.* 25, 145-154 (1996).
15. Ishiwata, K., Ogi, N., Tanaka, A. & Senda, M. Quantitative *ex vivo* and in vitro receptor autoradiography using 11C-labeled ligands and an imaging plate: a study with a dopamine D2-like receptor ligand [11C] nemonapride. *Nucl. Med. Biol.* 26, 291-296 (1999).
16. Vincent-Genod, L., Benderitter, M. & Voisin, P. Micro-organisation of the membrane after radiation-induced apoptosis: a flow cytometry study. *Radiat. Environ. Biophys.* 40, 213-219 (2001).
17. Giusti, A. M., Raimondi, M., Ravagnan, G., Sapora, O. & Parasassi, T. Human cell membrane oxidative damage induced by single and fractionated doses of ionizing radiation: a fluorescence spectroscopy study. *Int. J. Radiat. Biol.* 74, 595-605 (1998).
18. Berroud, A., Le, R. A. & Voisin, P. Membrane oxidative damage induced by ionizing radiation detected by fluorescence polarization. *Radiat. Environ. Biophys.* 35, 289-295 (1996).
19. Regev, R., Assaraf, Y. G. & Eytan, G. D. Membrane fluidization by ether, other anesthetics, and certain agents abolishes P-glycoprotein ATPase activity and modulates efflux from multidrug-resistant cells. *Eur. J. Biochem.* 259, 18-24 (1999).
20. Sinicrope, F. A., Dudeja, P. K., Bissonnette, B. M., Safa, A. R. & Brasitus, T. A. Modulation of P-glycoprotein-mediated drug transport by alterations in lipid fluidity of rat liver canalicular membrane vesicles. *J. Biol. Chem.* 267, 24995-25002 (1992).

Chapter 4

In vivo VEGF imaging with radiolabeled bevacizumab in a human ovarian tumor xenograft

Wouter B. Nagengast[1], Elisabeth G. de Vries[1], Geke A. Hospers[1], Nanno H. Mulder[1], Johan R. de Jong[3], Harry Hollema[4], Adrienne H. Brouwers[3], Guus A. van Dongen[5], Lars R. Perk[5], Marjolijn N. Lub-de Hooge[2,3]

Dept. of Medical Oncology[1], Hospital and Clinical Pharmacy[2], Nuclear Medicine and Molecular Imaging[3], Pathology[4], University of Groningen and University Medical Center Groningen, Dept. of Nuclear Medicine and PET Research[5], VU Medical Center, Amsterdam, The Netherlands.

Journal of Nuclear Medicine. 2007;48:1313-9.

Abstract

Vascular endothelial growth factor (VEGF), released by tumor cells, is an important growth factor in tumor angiogenesis. The humanized monoclonal antibody bevacizumab blocks VEGF induced tumor angiogenesis by binding, and thereby neutralizing VEGF. Aim: Development of radiolabeled bevacizumab for non-invasive *in vivo* VEGF visualization and quantification with the single gamma emitting isotope ^{111}Indium [^{111}In] and the PET isotope ^{89}Zirconium [^{89}Zr]. Methods: Labeling, stability and binding studies were performed. Nude mice with a human SKOV-3 ovarian tumor xenograft were injected with ^{89}Zr-bevacizumab, ^{111}In-bevacizumab or human ^{89}Zr-IgG. Human ^{89}Zr-IgG served as an aspecific control antibody. MicroPET imaging and microCT imaging studies were obtained at 24, 72 and 168 h post injection of ^{89}Zr-bevacizumab and ^{89}Zr-IgG (3.5 ± 0.5 MBq, 100 ± 6 μg, 0.2 mL). MicroPET and microCT images were fused to calculate tumor uptake and compared with *ex vivo* biodistribution at 168 h post injection. ^{89}Zr-, and ^{111}In-bevacizumab *ex vivo* biodistribution were compared at 24, 72 and 168 h post injection (2.0 ± 0.5 MBq each, 100 ± 4 μg in total, 0.2 mL). Results: Labeling efficiencies, radiochemical purity, stability and binding properties were optimal for the radioimmunoconjugates. MicroPET imaging showed uptake in well-perfused organs at 24 h and clear tumor localization from 72 h on. Tumor uptake determined by quantification of MicroPET images was higher for ^{89}Zr-bevacizumab, namely 7.38 ± 2.06 %ID/g compared to 3.39 ± 1.16 %ID/g for human ^{89}Zr-IgG (P = 0.011) at 168 h and equivalent to *ex vivo* biodistribution studies. Tracer uptake in other organs was mainly seen in liver and spleen. ^{89}Zr-, and ^{111}In-bevacizumab biodistribution was comparable. Conclusion: Radiolabeled bevacizumab showed higher uptake compared to radiolabeled human IgG in a human SKOV-3 ovarian tumor xenograft. Non-invasive quantitative MicroPET imaging was similar to invasive *ex vivo* biodistribution. Radiolabeled bevacizumab is a new tracer for non-invasive *in vivo* imaging of VEGF in the tumor micro-environment.

Introduction

There are several factors involved in the development and growth of tumors. Angiogenesis, the forming of new blood vessels is one of these factors. New vasculature allows tumor cells to execute their critical growth by supplying the tumor with nutrients and oxygen, enabling disposal of metabolic waste products and providing a route for metastatic spreading [1,2]. An important factor involved in angiogenesis is Vascular Endothelial Growth Factor A (hereafter referred as VEGF) [3]. VEGF consists of at least 4 splice variants, containing 121, 165, 189 and 206 amino acids [3]. It is produced by tumor cells and induces tumor neovascularization [4-7].

Overexpression of VEGF occurs in many human tumor types which made VEGF a rational target for anti-angiogenic therapy [8-11]. This has lead to interest in blocking the signaling of VEGF in human tumors. Antibodies binding to this ligand and its receptors, and chemical molecules which can block the tyrosine kinase function of VEGF-receptors have been developed [12].

The drug that is currently most widely used in the clinic is the humanized monoclonal antibody bevacizumab. It blocks VEGF induced endothelial cell proliferation, permeability and survival, and it inhibits human tumor cell line growth in pre-clinical models [8,13-15]. The likely mechanism is that bevacizumab binds to VEGF, both soluble and bound to the extra cellular matrix, and thereby prevents VEGF binding to its receptors, blocking the biological pathways induced following VEGF binding. Bevacizumab is approved for clinical use in metastatic colon carcinoma and non-small cell lung cancer [16,17]. Approval for several other tumor types is expected soon.

Despite the success of anti-angiogenic therapy, there is a large percentage of patients who do not benefit from this targeted therapy. Currently, it is impossible to predict which patient will benefit from anti-angiogenic therapy. Reasons for treatment failure may be the fact that the target for the drug is not present or that the drug may not reach the target. As described above, tumor cells produce VEGF, which can lead to paracrine effects in the micro-environment. $VEGF_{121}$ is freely soluble, whereas $VEGF_{165}$ is secreted, though a significant fraction remains localized to the extra cellular matrix, like $VEGF_{189}$ and $VEGF_{206}$ [18]. This will most likely lead to locally high VEGF levels. It is currently not possible to evaluate these local VEGF levels [19]. Non-invasive measurement of VEGF in the tumor might give insight in the available target for VEGF dependent anti-angiogenic therapy and thus assist in tumor response prediction. To allow *in vivo* VEGF imaging, we set up bevacizumab labeling with the relatively new long-lived PET isotope ^{89}Zirconium [^{89}Zr], and the widely available single gamma emitting isotope ^{111}Indium [^{111}In] [20,20-23].

In the present study we describe the development and the *in vivo* evaluation of ^{89}Zr-bevacizumab and ^{111}In-bevacizumab in a tumor bearing mice model, and will compare non-invasively obtained *in vivo* ^{89}Zr-bevacizumab and ^{89}Zr-IgG imaging quantification data with *ex vivo* biodistribution data.

Materials and Method

Conjugation and ^{89}Zr-labeling of bevacizumab and control IgG

Bevacizumab (Avastin®, 25 mg/mL, Roche, Welwyn Garden City, UK) and human IgG (Immunoglobulin iv, Sanquin, Amsterdam, The Netherlands) conjugation and labeling was performed as described previously by Verel et al [22]. Human IgG served as an aspecific control antibody. Briefly, bevacizumab and IgG were purified from other excipients by ultrafiltration (Vivaspin-2, Sartorius, Göttingen, Germany) and diluted in water for injection to 5 mg/mL. Hereafter, conjugation of purified bevacizumab and IgG was achieved using *N*-succinyldesferrioxamine B-tetrafluorphenol (*N*-sucDf-TFP) (VUmc, Amsterdam, The Netherlands). The ester and the antibodies (bevacizumab and human IgG) were conjugated at room temperature for 30 min at pH 9.5-9.7 (0.1 mol/L Na_2CO_3, Bufa, Uitgeest, The Netherlands) with 1.5-2.5 chelate groups per antibody molecule. After conjugation, the mixture was set to pH 4.2-4.4 (0.1 mol/L H_2SO_4) and 50 µL of 25 mg/mL ethylenediaminetetraacetic acid (EDTA, Calbiochem, Darmstadt, Germany) were added. The solutions were incubated 30 min at 35°C, and again purified by ultrafiltration, diluted in water for injection (5 mg/mL) and stored at -20°C.

Labeling was performed with ^{89}Zr ($T_{1/2}$ 3.27d) produced by Cyclotron BV (Amsterdam, The Netherlands), which was delivered as ^{89}Zr-oxalate dissolved in oxalic acid (1 M oxalic acid, 2 GBq/mL, 4 GBq/ug ^{89}Zr, 99.9% radionuclidic purity). In brief, the ^{89}Zr-oxalate solution was set on pH 3.9-4.2 and mixed for 3 min. with 4-(2-hydroxyethyl)-1-piperazineethanesulfonic acid (HEPES) (Sigma-Aldrich, Poole, UK) buffer and was adjusted to pH 6.7-6.9. N-sucDf-bevacizumab was added and incubated for 45 min at room temperature.

Conjugation and ^{111}In-labeling of bevacizumab

Bevacizumab was conjugated with the chelator 2-(4-Isothiocyanatobenzyl)-diethylene-triaminepentaacetic acid (ITC-DTPA)(Macrocyclics, Dallas, TX) according to Ruegg et al [24] with 2-3 chelate groups per antibody molecule. Briefly, 5 mg purified bevacizumab was adjusted to pH 9.2-9.5 (50 mmol/L Na_2CO_3, pH 9.5, Bufa, Uitgeest, The Netherlands) and 50 M excess ITC-DTPA was added. After 1 h incubation at room temperature, the

reaction mixture was purified by ultracentrifugation with ammonium acetate (50 mmol/L), pH 5.5, to eliminate the excess unconjugated ITC-DTPA. Purified conjugated bevacizumab was diluted (5 mg/mL) in ammonium acetate and stored at -20°C. Labeling was performed with 1 mg of purified ITC-DTPA-bevacizumab, which was allowed to react with 50 MBq of $^{111}InCl_3$ (370 MBq/mL, >1.85 GBq/μg ^{111}In, 99.9% radionuclidic purity, Tyco Health Care, Petten, Netherlands) for 1 h at room temperature. Glassware, materials and solutions used for the conjugation and labeling procedures were sterilized, pyrogen-free and metal-free.

Quality control of ^{89}Zr-bevacizumab, ^{111}In-bevacizumab and ^{89}Zr -IgG

The radiochemical purity of the radiolabeled antibodies was determined by size exclusion high performance liquid chromatography (SE-HPLC), trichloroacetic acid protein precipitation (TCA) (^{89}Zr-antibodies) and instant thin layer chromatography (iTLC) (^{111}In-bevacizumab) to differentiate the labeled product from aggregates and unlabeled ^{89}Zr and ^{111}In.

The HPLC system used consisted of a Waters 1500 series manual injector with 20 μL injection loop (Rheodyne™ 7725i injector, Milford, MA), a Waters 1525 binary HPLC pump, a Waters 2487 dual-wavelength absorbance detector and an in-line radioactivity detector made of a sodium iodide crystal coupled to a multichannel analyzer (Ortec, Nieuwegein, The Netherlands). Chromatograms were analyzed using the Breeze software (Waters, Etten-Leur, The Netherlands). The size exclusion column used was a Superdex™ 200 30/300 GL (Amersham Biosciences, Uppsala, Sweden). The mobile phase consisted of phosphate-saline buffer (PBS; 140 mmol/L NaCl, 9 mmol/L Na_2HPO_4, 1.3 mmol/L NaH_2PO_4; pH=7.4, UMC Groningen, The Netherlands) containing 10% methanol and 23 g/L NaCl. The flow was 0.75 mL/min and the UV-detector wavelengths were set to 220 and 280 nm. The column performance was tested using a reference Bio-Rad gel filtration standard. The retention time of bevacizumab was 16.7 min. TCA precipitation was performed by mixing equal amounts of water for injection, trichloroacetic acid 20% and 3 μL ^{89}Zr-bevacizumab reaction solution. The mixture was centrifuged and the radiochemical purity was determined by separation of the protein fraction and supernatant. The radioactivity in the fractions was measured by a LKB-1282-Compu-gamma system (LKB Wallac, Turku, Finland).

ITLC was performed on silica gel strips using 0.15 mol/L citrate buffer (pH 6.0) as the mobile phase. Radioactivity was determined by an iTLC scanner (VCS-101, Veenstra Instruments, Joure, The Netherlands).

In vitro evaluation of the radiolabeled compounds

Stability of ^{89}Zr-bevacizumab, ^{89}Zr-IgG and ^{111}In-bevacizumab was determined by storing the final product (1 mg, 50 MBq) in 1 mL ammonium acetate (50 mmol/L) at 4°C and in 1 mL human serum at 37°C for 7 days. SE-HPLC, TCA and iTLC procedures were performed 24, 72 and 168 h after labeling.

The binding properties for VEGF of ^{89}Zr-bevacizumab, ^{111}In-bevacizumab and ^{89}Zr-IgG were evaluated using a VEGF coated ELISA, comparable with the method described by Collingridge et al [25]. Shortly, recombinant human $VEGF_{165}$ (catalog No. 293-VE/CF; R&D systems, Minneapolis, MN) was used as the target antigen and coated to Nunc-Immuno™ BreakApart™ plates (NUNC, Roskilde, Denmark). Recombinant human $VEGF_{165}$ was diluted in PBS to a concentration of 5 μg/mL. The solution was adjusted to pH 9.2-9.5 (50 mmol/L Na_2CO_3, UMC Groningen, The Netherlands). 50 μL were added to the wells, incubated overnight at 4°C and then blocked with 1% human serum albumin (HSA) (Sanquin, Amsterdam, The Netherlands) in PBS. After blocking, the plates were washed with 0.1% polysorbate 80 (Sigma-Aldrich, Poole, UK) in PBS. ^{89}Zr-Bevacizumab, ^{111}In-bevacizumab and ^{89}Zr-IgG solutions were diluted in PBS (concentrations 1.0-1.0x10^6 ng/mL), added to the wells and incubated for 2 h. Subsequently, the reaction solution was collected from the wells in two wash steps. Both the sustained radioactivity stacked to the antigen-coated wells and the collected reaction solution containing unbound radiolabeled antibody were measured by a LKB-1282-Compu-gamma system. The percentage of binding was calculated as the fraction radioactivity stacked to antigen coated wells divided by the total amount of radioactivity added.

Competition experiments were performed by diluting bevacizumab standard solution (25 mg/mL) with PBS and adding an excess of unlabeled bevacizumab up to 500 fold. Glassware, materials and solutions used for binding studies were pyrogen-free, metal-free and coated with 2% HSA in PBS.

Cell culture and animal studies

The human ovarian cancer cell line SKOV-3 was cultured in Dulbecco's Modified Eagles Medium (DMEM) with 4.5 g/mL glucose and 10% fetal calf serum. SKOV-3 cells were chosen because of identified high VEGF production *in vivo* [26]. Before animals were inoculated, the SKOV-3 cells were harvested by trypsinization and resuspended in culture medium and Matrigel™ (BD Bioscience, Alphen aan den Rijn, The Netherlands). *In vivo* imaging and biodistribution experiments were conducted using male athymic mice (HSD; Athymic nude-*nu*) obtained from Harlan Nederland (Horst, the Netherlands). At 8 weeks

of age the mice were injected subcutaneous with $1x10^6$ SKOV-3 cells mixed equally with 0.1 mL Matrigel™. Animals were used for *in vivo* studies when the tumor measured between 6-8 mm in diameter (± 0.2 cm^3), approximately 2-3 weeks after inoculation.

All animal experiments were performed with isofluran inhalation anesthesia (induction 3%, maintenance 1.5%). ^{89}Zr-bevacizumab (n=6) and ^{89}Zr-IgG (n=6) were injected intravenously into the penile vein (3.5 ± 0.5 MBq, 100 ± 6 μg, 0.2 mL). Animals were imaged using a MicroPET Focus 220 rodent scanner (CTI Siemens, Munich, Germany). Static images of 30 min acquisition time were obtained at 24, 72 and 168 h post injection. Images were corrected for scatter and attenuation. Thereafter, MicroCT images were made using a MicroCAT II (CTI Siemens, Munich, Germany). Images were reconstructed and 3-dimensional regions of interest (ROI) were drawn within the MicroCT images and transposed into MicroPET images for quantification, using the AsiPro 6.2.5.0. software fusion tool (CTI Siemens, Munich, Germany). The total injected dose was calculated by decay correction of the activity present at 24 h post injection in the animal, at which the clearance of the injected antibodies is almost negligible. Data is presented as percentage of injected dose per gram tissue (%ID/g), assuming a tissue density of 1 g/cm^3. Animals were sacrificed after the last scan (168 h) and organs and tissues were excised, rinsed for residual blood and weighed.

Animals used for *ex vivo* biodistribution studies were injected intravenously into the penile vein containing a combined dose of 50% ^{111}In-bevacizumab and 50% ^{89}Zr-bevacizumab (2.0 ± 0.5 MBq each, 100 ± 4 μg in total, 0.2 mL). Mice were sacrificed at 24 (n=5), 72 (n=5) and 168 h (n=5) post injection. Organs and tissues were excised, rinsed for residual blood and weighed.

Samples and primed standards were counted for radioactivity in a calibrated well-type LKB-1282-Compu-gamma system and corrected for physical decay. Biodistribution samples were measured using dual isotope counting programs for ^{89}Zr and ^{111}In enabling comparison between ^{89}Zr-bevacizumab and ^{111}In-bevacizumab distribution. Tissue activity is expressed as percentage of the injected dose per gram tissue (%ID/g).

All animal experiments were approved by the animal experiments committee of the University of Groningen.

Immunohistochemistry

Frozen-embedded tumors were stained with antibodies against mouse CD31 (PEGAM-1) (BD Pharmingen, San Diego, CA) and human IgG (Dako, Glostrup, Denmark). Anti-CD31 staining was performed to determine the micro vessel density in the tumors of mice

who received ^{89}Zr-bevacizumab or ^{89}Zr-IgG. Micro vessel density was scored in three areas, defined as hot spot areas with maximum number of microvessels, by using a calibrated grid. Anti-human IgG staining was carried out to obtain more detailed information about the localization of the tracers. The slides were examined at x200 magnification.

Statistical analysis

Data are presented as means ± standard deviation (SD). Statistical analysis was performed using Mann-Whitney test (SPSS, version 12). A *P*-value ≤ 0.05 was considered significant.

Results

Radiolabeling, quality control

Labeling with ^{89}Zr and ^{111}In resulted in labeling yields of 98.0 ± 0.7% for ^{89}Zr-bevacizumab and 96.6 ± 0.5% for ^{111}In-bevacizumab and 95.4 ± 0.3% for ^{89}Zr-IgG, not acquiring purification. Specific activity was 58 MBq/mg for ^{89}Zr-bevacizumab and 50 MBq/mg for ^{111}In-bevacizumab. No impurities were detected. These results demonstrate that bevacizumab and human IgG can be labeled with high labeling efficiency with ^{89}Zr and ^{111}In.

In vitro evaluation of the radiolabeled compounds

^{89}Zr-bevacizumab stored at 4°C ammonium acetate and at 37°C serum for 1 week displayed a small decrease (6%) in protein-bound radioactivity after 168 h. ^{111}In-bevacizumab and ^{89}Zr-IgG showed even less decrease (≤ 5%) in protein-bound radioactivity. The stability of the labeled products ensures optimal quantitative measurement and imaging during 1 week.

Radiolabeled bevacizumab showed adequate VEGF binding, irrespective the type of radiolabeling. Binding experiments of ^{89}Zr-bevacizumab resulted in 54.0 ± 3.7% binding. A competition assay with an excess unlabeled bevacizumab (≥ 500 fold) could almost completely block ^{89}Zr-bevacizumab binding (< 5%), comparable to 4-8% non-specific binding for ^{89}Zr-IgG. Experiments with ^{111}In-bevacizumab showed 56.9 ± 0.7% binding. Competitions experiments with 50% radiolabeled and unlabeled bevacizumab (1:1) resulted in 35.9 ± 7.5% decrease the initial binding of radiolabeled bevacizumab, demonstrating almost equal binding characteristics of radiolabeled and unlabeled bevacizumab. These results ensure adequate VEGF binding by ^{89}Zr- and ^{111}In-bevacizumab.

Animal Studies

MicroPET and MicroCT fusion enabled excellent tumor visualization and quantification (Figure 1). MicroPET images showed uptake in well-perfused organs and plasma at 24 h

post injection, which declined at later time points. Increasing tumor/blood ratio resulted in clear tumor localization of ^{89}Zr-bevacizumab from 72 h on post injection (Figure 2). In addition uptake of ^{89}Zr-bevacizumab was furthermore predominantly seen in liver and spleen. Quantitative measurement of ^{89}Zr-bevacizumab in the tumor by MicroPET was significantly higher compared to human ^{89}Zr-IgG, namely 7.38 ± 2.06 %ID/g compared to 3.39 ± 1.16 %ID/g (P=0.011) at 168 h post injection (Figure 3). Similar results were seen in biodistribution experiments when tumors were excised and counted in a gamma counter: tumor uptake was 6.82 ± 1.80 %ID/g for ^{89}Zr-bevacizumab compared to 2.87 ± 0.48 %ID/g for human ^{89}Zr-IgG (P=0.006) (Figure 3). Beside tumor uptake, *ex vivo* biodistribution experiments showed an equal organ distribution pattern for ^{89}Zr-bevacizumab and ^{89}Zr-IgG (Figure 4), except for kidney uptake, which was significantly higher for ^{89}Zr-IgG, compared to ^{89}Zr-bevacizumab (P=0.004).

The *ex vivo* biodistribution for ^{89}Zr-bevacizumab and ^{111}In-bevacizumab was similar at 24, 72 and 168 h post injection (Table 1), demonstrating that both tracers could be used for VEGF imaging.

Immunohistochemistry

There was no difference in micro vessel density or blood vessel distribution pattern between the tumors of the ^{89}Zr-bevacizumab and the ^{89}Zr-IgG injected mice. Anti-human IgG staining was mainly seen in the blood vessels of the tumor (Figure 5).

Discussion

^{89}Zr and ^{111}In labeling of bevacizumab resulted in high labeling efficiencies and adequate preservation of VEGF binding properties. Tumor uptake of ^{89}Zr-bevacizumab and ^{111}In-bevacizumab were both significantly higher compared to control ^{89}Zr-IgG. Tumor uptake of ^{89}Zr-bevacizumab and ^{111}In-bevacizumab was already high at 24 h post injection, increasing in time with clear tumor visualization from 72 h on post injection. These results demonstrate that radiolabeled bevacizumab is a potential new tracer for non-invasive imaging of VEGF in the micro-environment of the tumor.

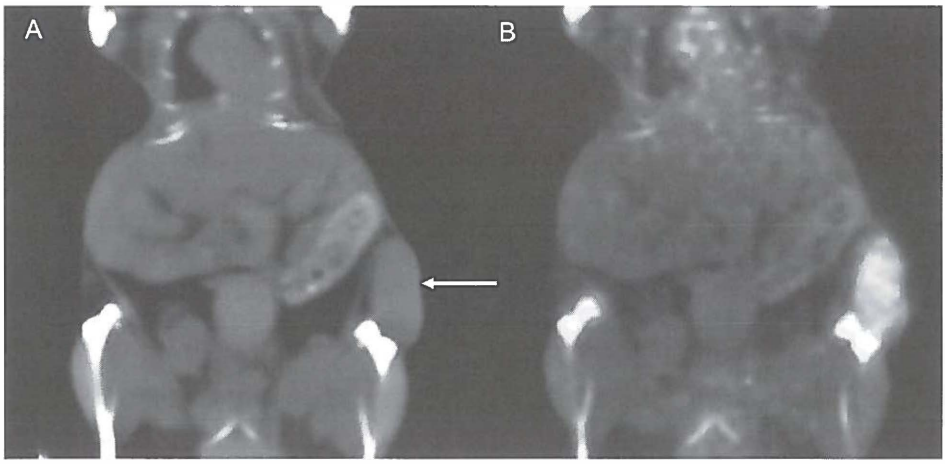

Figure 1. Coronal CT image (A) with clear subcutaneous localization of the SKOV-3 tumor (arrow). Fusion of MicroPET and CT images (B) (168 h post injection) enables adequate quantitative measurement of ^{89}Zr-bevacizumab in the tumor. (see page 151 for color figure)

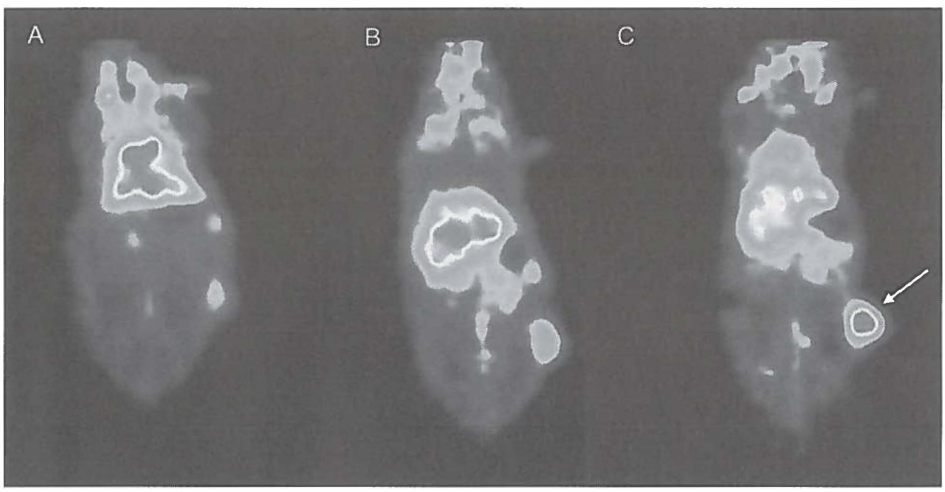

Figure 2. Coronal planes of MicroPET images 24 (A), 72 (B) and 168 h (C) post injection of ^{89}Zr-bevacizumab. At 24 h most uptake is in the well-perfused organs. In time, relative uptake in the tumor (arrow) increases. (see page 151 for color figure)

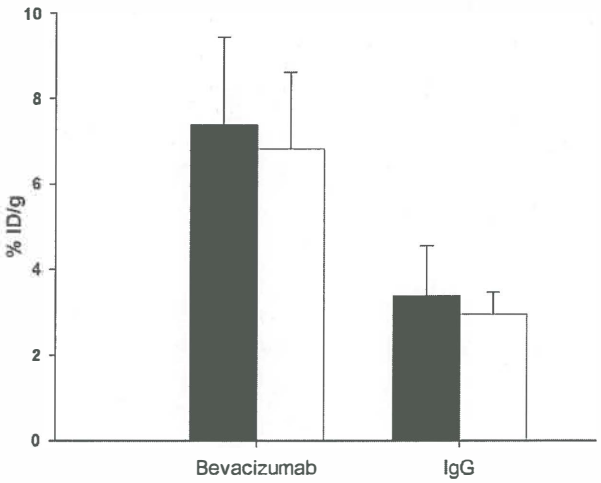

Figure 3. Comparison of tumor uptake of ^{89}Zr-bevacizumab and control ^{89}Zr-IgG as determined by non-invasive microPET imaging (■)(n=6) and by gamma counting of excised tumors (□) (n=6) 168 h post injection. Data is presented as %ID/g ± (SD), assuming a tissue density of 1 g/cm^3.

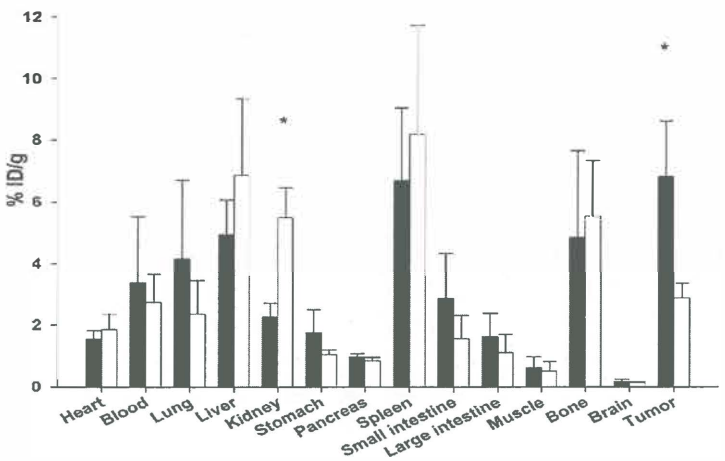

Figure 4. *Ex vivo* biodistribution of ^{89}Zr-bevacizumab (n=6) (■) and control ^{89}Zr-IgG (n=6) (□) 168 h post injection. Uptake of ^{89}Zr-bevacizumab within the tumor is significantly higher than control ^{89}Zr-IgG (p=0.006). Data is presented as %ID/g ± (SD). * $P \leq 0.05$.

Table 1. *Ex vivo* biodistribution of mice receiving ^{89}Zr-bevacizumab and ^{111}In-bevacizumab. Data presented as %ID/g ± (SD).

	24 h (n=5)		72 h (n=5)		168 h (n=5)	
	^{89}Zr-bev.	^{111}In-bev.	^{89}Zr-bev.	^{111}In-bev.	^{89}Zr-bev.	^{111}In-bev.
Heart	3.43 ± (0.99)	4.34 ± (1.22)	2.31 ±(0.93)	3.60 ± (0.95)	2.11 ± (0.66)	3.09 ± (1.30)
Blood	9.54 ± (5.12)	11.87± (6.19)	5.60 ± (3.20)	8.50 ± (1.84)	3.75 ± (2.24)	5.99 ± (2.01)
Lung	6.22 ± (4.39)	7.58 ± (4.86)	3.50 ± (1.57)	5.24 ± (1.88)	2.75 ± (0.84)	3.56 ± (0.89)
Liver	5.01 ± (1.27)	4.91 ± (0.95)	3.98 ± (1.29)	5.17 ± (1.22)	3.93 ± (1.49)	3.30 ± (0.59)
Kidney	3.94 ± (0.91)	4.35 ± (1.01)	2.51 ± (0.93)	3.36 ± (0.56)	2.45 ± (0.44)	2.82 ± (0.63)
Stomach	2.01 ± (0.25)	2.37 ± (0.40)	1.33 ± (0.50)	1.94 ± (0.66)	1.15 ± (0.45)	1.30 ± (0.36)
Pancreas	1.83 ± (0.30)	2.33 ± (0.35)	0.99 ± (0.42)	1.49 ± (0.27)	0.93 ± (0.17)	1.06 ± (0.19)
Spleen	4.52 ± (1.92)	5.74 ± (2.76)	3.22 ± (1.41)	5.13 ± (2.91)	6.07 ± (4.80)	6.37 ± (4.54)
Small intestine	3.24 ± (2.11)	4.10 ± (2.72)	1.54 ± (0.99)	2.40 ± (1.79)	2.03 ± (1.86)	1.91 ± (1.35)
Large intestine	2.09 ± (0.45)	2.57 ± (0.64)	1.12 ± (0.41)	1.64 ± (0.60)	1.63 ± (1.12)	1.48 ± (0.64)
Muscle	1.02 ± (0.16)	1.23 ± (0.15)	0.60 ± (0.23)	0.90 ± (0.08)	0.61 ± (0.20)	0.82 ± (0.38)
Bone	3.00 ± (0.87)	3.05 ± (0.77)	2.77 ± (1.93)	2.29 ± (1.17)	5.75 ± (4.01)	2.48 ± (1.49)
Brain	0.33 ± (0.09)	0.41 ± (0.11)	0.21 ± (0.09)	0.31 ± (0.05)	0.22 ± (0.06)	0.26 ± (0.09)
Tumor	4.85 ± (1.55)	6.23 ± (2.03)	4.36 ± (2.80)	6.17 ± (1.30)	6.97 ± (2.41)	7.74 ± (1.99)

Two human anti-VEGF antibodies, VG76e and HumMV833, have been used previously for non-invasive VEGF imaging [25,27]. ^{125}I- and ^{124}I-labeled VG76e, an IgG1 mouse monoclonal anti-VEGF antibody which recognizes the 121, 165 and 189 isoforms of human VEGF-A, showed specific tumor targeting in a human fibrosarcoma xenograft mice model. Maximum uptake was seen after 24 h, declining at 48 h post injection. These results are in contrast to our results, in which radiolabeled bevacizumab did not show tumor clearance up to 168 h post injection, which increases the available time for imaging. Jayson et al. used ^{124}I-HuMV833, a humanized monoclonal IgG4$_k$ antibody that binds VEGF$_{121}$ and VEGF$_{165}$, to perform PET-imaging studies in patients with various progressive solid tumors. Tumor uptake of ^{124}I-HuMV833 was highly variable between and within patients. For example, there was high uptake of ^{124}I-HuMV833 in an ovarian tumor and low uptake in a poorly vascularized metastasis from colon cancer [27]. These differences may represent the variation in available target for the antibody between tumor types and lesions, which could have implications for anti-VEGF therapy [27]. The monoclonal antibody bevacizumab that we used in this study, with high binding affinity to all VEGF-A isoforms and proven clinical effectiveness, is more attractive and accessible for this approach. Another point of application in the evaluation of anti-VEGF therapy could be VEGF-receptor imaging. Cai et al. described the development of VEGF-receptor imaging with ^{64}Cu-DOTA-VEGF$_{121}$ [28]. They showed that VEGF-receptor imaging with ^{64}Cu-DOTA-VEGF$_{121}$ corresponded with immunohistochemical analysis in a human glioblastoma bearing mouse model. At this point, the correlation between levels of VEGF expression and VEGF-receptor expression are not elucidated. Therefore, *in vivo* VEGF-receptor imaging with ^{64}Cu-DOTA-VEGF$_{121}$ might facilitate the evaluation of VEGF-receptor expression, whereas radiolabeled bevacizumab could be used evaluating VEGF-levels. Both techniques could be complementary in the clinical evaluation of anti-angiogenic therapy.

In the present study we have shown that MicroPET en CT imaging, using ^{89}Zr-bevacizumab, did not only allow imaging up to 168 h post injection, but also enables quantitative measurement of the tracer in the tumor. Tumor uptake values as assessed by non-invasive MicroPET quantification of ^{89}Zr-bevacizumab were identical to uptake values as assessed by gamma counting of excised tumors, demonstrating the potential role of PET quantification beside *in vivo* visualization. Biodistribution of bevacizumab was previously investigated by Lin et al. in rabbits with ^{125}I-labeled bevacizumab, however the uptake of bevacizumab was only investigated in normal tissues [29]. The results were similar to our findings, with high uptake in heart and blood after 24 h, decreasing in time, and high uptake

in liver and spleen at later time points. Our study additionally demonstrated that the tumor is a major compartment, besides plasma, liver and spleen in bevacizumab distribution.

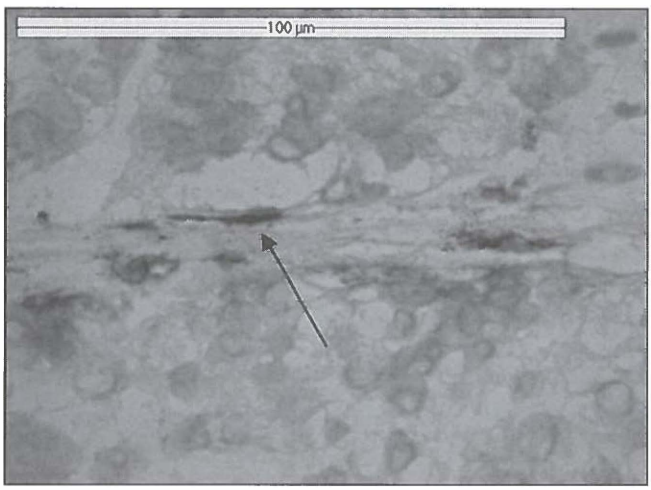

Figure 5. Anti-human IgG staining (arrow) in a tumor slice from mice receiving ^{89}Zr-bevacizumab. (see page 152 for color figure)

We used 100 µg of ^{89}Zr-bevacizumab for imaging and biodistribution studies. Smaller doses of bevacizumab could result in accelerated and increased clearance of ^{89}Zr- and ^{111}In-bevacizumab in the absence of IgG production by the nude mice [30]. As a control we used ^{89}Zr labeled human IgG, to provide evidence that ^{89}Zr-bevacizumab uptake is due to specific targeting in the tumor and not caused by blood perfusion and passive diffusion within the tumor. An other frequently used approach to show specificity is blocking with an excess the unlabeled agent [25]. However, the use of an excess of unlabeled bevacizumab (up to 10 fold) could induce functional changes and in this way change the perfusion and uptake of radiolabeled bevacizumab in the tumor at later time points [31]. Vascular changes after a single infusion of bevacizumab have been described earlier. Willet et al. showed a decreased micro vessel density in rectal cancer patients already 12 days after a single infusion of bevacizumab [31]. To exclude that these effects were present in our study, due to 100 µg of radiolabeled bevacizumab, the micro vessel density was determined in the tumors of the ^{89}Zr-bevacizumab and ^{89}Zr-IgG injected mice. There was no difference in micro vessel density between the tumors of the two groups. These findings substantiate the result that

high uptake of radiolabeled bevacizumab is due to specific targeting and not a result of vascular changes.

To obtain more detailed information regarding the localization of radiolabeled bevacizumab (humanized IgG1 antibody) in the tumor we performed anti-human IgG staining. Anti-human IgG was predominantly present in the blood vessels of the tumors. Cell surface binding of anti-human IgG was not clearly seen. From these results it is suggested that radiolabeled bevacizumab binds mainly to VEGF present in de blood vessels of the tumor. Binding to VEGF localized in the extra cellular matrix of tumor cells could not be demonstrated.

In the present study we used two isotopes for the development of radiolabeled bevacizumab. The PET isotope ^{89}Zr has got good characteristics for antibody imaging. The relatively long half life of 3.27 days makes imaging possible matching the pharmacokinetics of bevacizumab ($T_{1/2}$ 17-21 days), combined with the advantages of high resolution PET-imaging. Borjesson et al. described the first clinical application of ^{89}Zr, using labeled U36, an anti-CD44v6 antibody, to detect lymph node metastases in head and neck cancer patients [23]. ^{89}Zr will be soon commercially available. ^{89}Zr might give a relatively high radiation exposure to patients, due to the high-energy, high abundance γ-ray (909 keV, 99.9%) and low abundance β^+ (22%) emitted during the decay of ^{89}Zr [32]. However, the clinical dose for adequate ^{89}Zr-bevacizumab PET-imaging has yet to be established. Increased sensitivity of new generation PET-cameras could further reduce the radiation exposure. As an alternative for PET-imaging, we also developed ^{111}In labeled bevacizumab for SPECT imaging, as we described previously for trastuzumab, a HER-2 neu antibody [20]. *Ex vivo* biodistribution results for ^{111}In labeled bevacizumab were similar to ^{89}Zr-bevacizumab. Both ^{111}In-bevacizumab and ^{89}Zr-bevacizumab can be used clinically for non-invasive *in vivo* VEGF imaging, though the feasibility of ^{111}In-bevacizumab for *in vivo* quantification is not established by this study.

Conclusion

In conclusion, this study illustrates the potential of ^{89}Zr-bevacizumab and ^{111}In-bevacizumab as a specific VEGF tracer, with excellent *in vivo* quantitative measurement of ^{89}Zr-bevacizumab. Non-invasive measurement of VEGF levels in the tumor could provide essential information in the evaluation of anti-angiogenic therapy. This could lead to better understanding and patient tailored therapy.

References

1. Folkman, J. What is the evidence that tumors are angiogenesis dependent? *J. Natl. Cancer Inst.* 82, 4-6 (1990).
2. Folkman, J. & Klagsbrun, M. Angiogenic factors. *Science* 235, 442-447 (1987).
3. Ferrara, N. & Davis-Smyth, T. The biology of vascular endothelial growth factor. *Endocr. Rev.* 18, 4-25 (1997).
4. Ferrara, N. Vascular endothelial growth factor: basic science and clinical progress. *Endocr. Rev.* 25, 581-611 (2004).
5. Shibuya, M. Vascular endothelial growth factor receptor-2: its unique signaling and specific ligand, VEGF-E. *Cancer Sci.* 94, 751-756 (2003).
6. Crawford, S. E. Vascular interference: a blockade to tumor epithelial growth. *Hepatology* 39, 1491-1494 (2004).
7. Ferrara, N. Role of vascular endothelial growth factor in regulation of physiological angiogenesis. *Am. J. Physiol Cell Physiol* 280, C1358-C1366 (2001).
8. Gerber, H. P. & Ferrara, N. Pharmacology and pharmacodynamics of bevacizumab as monotherapy or in combination with cytotoxic therapy in preclinical studies. *Cancer Res.* 65, 671-680 (2005).
9. Akbulut, H. *et al*. Prognostic role of serum vascular endothelial growth factor, basic fibroblast growth factor and nitric oxide in patients with colorectal carcinoma. *Cytokine* 20, 184-190 (2002).
10. Shimanuki, Y. *et al*. Role of serum vascular endothelial growth factor in the prediction of angiogenesis and prognosis for non-small cell lung cancer. *Lung* 183, 29-42 (2005).
11. Yen, L. *et al*. Heregulin selectively upregulates vascular endothelial growth factor secretion in cancer cells and stimulates angiogenesis. *Oncogene* 19, 3460-3469 (2000).
12. Bergsland, E. K. Update on clinical trials targeting vascular endothelial growth factor in cancer. *Am. J. Health Syst. Pharm.* 61, S12-S20 (2004).
13. Wang, Y., Fei, D., Vanderlaan, M. & Song, A. Biological activity of bevacizumab, a humanized anti-VEGF antibody in vitro. *Angiogenesis.* 7, 335-345 (2004).
14. Yuan, F. *et al.* Time-dependent vascular regression and permeability changes in established human tumor xenografts induced by an anti-vascular endothelial growth factor/vascular permeability factor antibody. *Proc. Natl. Acad. Sci. U. S. A* 93, 14765-14770 (1996).
15. Fox, W. D. *et al.* Antibody to vascular endothelial growth factor slows growth of an androgen-independent xenograft model of prostate cancer. *Clin. Cancer Res.* 8, 3226-3231 (2002).
16. Hurwitz, H. *et al.* Bevacizumab plus irinotecan, fluorouracil, and leucovorin for metastatic colorectal cancer. *N. Engl. J. Med.* 350, 2335-2342 (2004).
17. Sandler, A. *et al.* Paclitaxel-carboplatin alone or with bevacizumab for non-small-cell lung cancer. *N. Engl. J. Med.* 355, 2542-2550 (2006).
18. Park, J. E., Keller, G. A. & Ferrara, N. The vascular endothelial growth factor (VEGF) isoforms: differential deposition into the subepithelial extracellular matrix and bioactivity of extracellular matrix-bound VEGF. *Mol. Biol. Cell* 4, 1317-1326 (1993).
19. Jain, R. K., Duda, D. G., Clark, J. W. & Loeffler, J. S. Lessons from phase III clinical trials on anti-VEGF therapy for cancer. *Nat. Clin. Pract. Oncol.* 3, 24-40 (2006).
20. Lub-De Hooge, M. N. *et al.* Preclinical characterisation of 111In-DTPA-trastuzumab. *Br. J. Pharmacol.* 143, 99-106 (2004).
21. Perik, P. J. *et al.* Indium-111-labeled trastuzumab scintigraphy in patients with human epidermal growth factor receptor 2-positive metastatic breast cancer. *J. Clin. Oncol.* 24, 2276-2282 (2006).
22. Verel, I. *et al.* Long-lived positron emitters zirconium-89 and iodine-124 for scouting of therapeutic radioimmunoconjugates with PET. *Cancer Biother. Radiopharm.* 18, 655-661 (2003).

23. Borjesson, P. K. *et al.* Performance of immuno-positron emission tomography with zirconium-89-labeled chimeric monoclonal antibody U36 in the detection of lymph node metastases in head and neck cancer patients. *Clin. Cancer Res.* 12, 2133-2140 (2006).
24. Ruegg, C. L. *et al.* Improved *in vivo* stability and tumor targeting of bismuth-labeled antibody. *Cancer Res.* 50, 4221-4226 (1990).
25. Collingridge, D. R. *et al.* The development of [(124)I]iodinated-VG76e: a novel tracer for imaging vascular endothelial growth factor *in vivo* using positron emission tomography. *Cancer Res.* 62, 5912-5919 (2002).
26. Keyes, K. A., Mann, L., Teicher, B. & Alvarez, E. Site-dependent angiogenic cytokine production in human tumor xenografts. *Cytokine* 21, 98-104 (2003).
27. Jayson, G. C. *et al.* Molecular imaging and biological evaluation of HuMV833 anti-VEGF antibody: implications for trial design of antiangiogenic antibodies. *J. Natl. Cancer Inst.* 94, 1484-1493 (2002).
28. Cai, W. *et al.* PET of Vascular Endothelial Growth Factor Receptor Expression. *J. Nucl. Med.* 47, 2048-2056 (2006).
29. Lin, Y. S. *et al.* Preclinical pharmacokinetics, interspecies scaling, and tissue distribution of a humanized monoclonal antibody against vascular endothelial growth factor. *J. Pharmacol. Exp. Ther.* 288, 371-378 (1999).
30. Sharkey, R. M., Natale, A., Goldenberg, D. M. & Mattes, M. J. Rapid blood clearance of immunoglobulin G2a and immunoglobulin G2b in nude mice. *Cancer Res.* 51, 3102-3107 (1991).
31. Willett, C. G. *et al.* Direct evidence that the VEGF-specific antibody bevacizumab has antivascular effects in human rectal cancer. *Nat. Med.* 10, 145-147 (2004).
32. Zalutsky, M. R. Potential of immuno-positron emission tomography for tumor imaging and immunotherapy planning. *Clin. Cancer Res.* 12, 1958-1960 (2006).

Chapter 5

^{89}Zr-bevacizumab PET imaging of early anti-angiogenic tumor response to treatment with HSP90 inhibitor NVP-AUY922

Wouter B. Nagengast[1], Maarten A. de Korte[1], Thijs H. Oude Munnink[1], Hetty Timmer-Bosscha[1], Wifred F. den Dunnen[4], Harry Hollema[4], Johan R. de Jong[3], Michael R. Jensen[6], Cornelia Quadt[7], Carlos Garcia-Echeverria[6], Guus A.M.S. van Dongen[5], Marjolijn N. Lub-de Hooge[2,3], Carolien P. Schröder[1], Elisabeth G.E. de Vries[1]

Departments of Medical Oncology[1], Hospital and Clinical Pharmacy[2], Nuclear Medicine and Molecular Imaging[3], Pathology[4], University of Groningen, Department of Nuclear Medicine and PET Research[5], VU Medical Center, Amsterdam, The Netherlands and Novartis Institutes for Biomedical Research[6] and Novartis Pharma AG[7], Basel, Switzerland.

Submitted

Abstract

Angiogenesis is a critical step in tumor development, in which VEGF is a key growth factor. Heat Shock Protein 90 (HSP90), a molecular chaperone, is essential for the activity of key proteins involved in VEGF transcription. There are currently no biomarkers to predict the effect of, or monitor, HSP90 inhibition therapy in individual patients. ^{89}Zr-bevacizumab PET imaging provides a non-invasive tool to monitor tumor VEGF levels. The aim of this study was to evaluate ^{89}Zr-bevacizumab PET imaging for early anti-angiogenic tumor response evaluation to treatment with the new HSP90 inhibitor NVP-AUY922. In xenografts of A2780 and its cisplatin resistant CP70 human ovarian cancer subline, ^{89}Zr-bevacizumab microPET was performed pre- and post NVP-AUY922 treatment and verified with histological response and *ex vivo* tumor VEGF levels. Two weeks of NVP-AUY922 treatment decreased ^{89}Zr-bevacizumab uptake with 44.4% (P=0.0003) in A2780 xenografts, while tumor uptake was not affected in CP70 xenografts compared to pre-treatment values. The same pattern was observed in A2780 and CP70 tumor VEGF levels, measured with ELISA, and mean vessel density (MVD) following NVP-AUY922 treatment. These findings coincided with reduction in the proliferation rate, assessed by Ki67 staining, in A2780 tumor tissue only.

In conclusion, ^{89}Zr-bevacizumab PET imaging was in line with the anti-angiogenic response and direct anti-tumor effects after NVP-AUY922 treatment, supporting the specificity of ^{89}Zr-bevacizumab PET as a sensitive technique to monitor the anti-angiogenic response of HSP90 inhibition *in vivo*.

Introduction

Angiogenesis, the formation of new blood vessels, is a critical factor involved in the development and growth of tumors [1]. An important factor involved in angiogenesis is vascular endothelial growth factor (VEGF). VEGF production by tumor cells is thought to be regulated by hypoxemia, growth factor signaling, cytokines and cell differentiation [1]. Over-expression of VEGF occurs in many human tumor types. Therefore, targeting angiogenesis is a rational treatment approach in many cancer types [2]. Currently, this can be done by VEGF neutralizing antibodies, small molecules blocking the VEGF receptor function or by drugs inhibiting cellular tumor signaling pathways affecting angiogenesis. Inhibition of Heat Shock Protein 90 (HSP90) is one way of affecting these pathways. HSP90 is a molecular chaperone, involved in maintaining the conformation, stability, cellular localization and activity of several key oncogenic client proteins [3,4]. HSP90 is constitutively expressed at 2 to 10 fold higher levels in cancer cells and present in active multi-chaperone complexes, conferring relative sensitivity to treatment with HSP90 inhibitors compared to their normal counterparts [3,5]. At this moment, several HSP90 inhibitors are being developed and investigated in pre-clinical and clinical studies. Of these, the geldanamycin analogue 17-allylamino-17-demethoxygeldanamycin (17-AAG; tanespimycin) has been studied most extensively and disease stabilizations and tumor responses have been observed in phase I/II clinical trials [6]. Another class of synthetic HSP90 inhibitors is the resorcinylic pyrazole/isoxazole amide analogues, of which NVP-AUY922, an improved isoxazole resorcinol, is the most potent yet described [6].

There are currently no biomarkers to predict the effect of, or monitor, HSP90 inhibition therapy in individual patients. One potential way to monitor HSP90 therapy is to prove its effect via changes in client proteins of HSP90. Client proteins of HSP90 include receptors and transcription factors like epidermal growth factor receptor 1 and 2 (EGFR and HER2), insulin-like growth factor type 1 receptor (IGF1-R1) and hypoxia inducible factor 1α (HIF1α) [3,7]. However, most of these client proteins can only be measured by collecting tumor biopsies. Therefore molecular imaging is an attractive alternative. It allows repetitive non-invasive follow up of specific targets. A suitable candidate is VEGF, a downstream product of various HSP90 client proteins [1,4]. Recently, it has been shown that HSP90 directed therapy leads to a reduction of VEGF secretion in tumor cell lines and a decreased mean vessel density (MVD) in tumor bearing animal models [7-11]. Due to the fact that larger isoforms of VEGF remain in the extra cellular tumor matrix before becoming active, these isoforms are attractive as imaging target [12,13]. Noninvasive measurement of VEGF in the tumor might give insight in the effect of HSP90 inhibition and thus assist in tumor response prediction.

Previously, we showed in a xenograft mouse model that bevacizumab, a monoclonal antibody against VEGF, radiolabeled with ^{89}Zirconium (^{89}Zr) and ^{111}Indium (^{111}In) can be used for *in vivo* VEGF visualization and quantification [13]. The advantage of ^{89}Zr-bevacizumab is that it allows high resolution and quantitative PET imaging. In addition, radiolabeled bevacizumab is currently used as GMP produced tracer in clinical development [14].

The aim of this study was to evaluate ^{89}Zr-bevacizumab PET for imaging of the early anti-angiogenic tumor response following treatment with the HSP90 inhibitor NVP-AUY922. To this end, an *in vivo* mouse model was used with xenografts from ovarian cancer cell lines A2780 and its cisplatin resistant subline CP70. ^{89}Zr-bevacizumab PET was performed before and after NVP-AUY922 treatment, and the imaging results were related to histological response and *ex vivo* tumor VEGF levels.

Materials and Methods

Cell lines and *in vitro* experiments

A2780 and its 7 fold cisplatin resistant subline CP70 were kindly provided by Dr. T.C. Hamilton (Fox Chase Cancer Center, Philadelphia, PA). All cells were cultured in RPMI 1640 (Invitrogen), supplemented with 10% heat inactivated fetal calf serum (FCS) (Bodinco BV) and 2 mM L-glutamine (Invitrogen) at 37°C in a fully humidified atmosphere containing 5% CO_2. Cells were subcultured three times per week.

For *in vitro* experiments, NVP-AUY922 was dissolved in DMSO at 10 mM, and stored at -80°C. A2780 and CP70 cells were plated (3 x 10^5 cells per well in 3 mL) and treated with 50 and 100 nM NVP-AUY922, relevant plasma levels in mice, or control medium ($n \geq 3$) [6,15]. After 24 h incubation, supernatant was collected and centrifuged at 180 g for 15 min. Supernatant samples were stored at -20°C until analysis. VEGF levels were determined with the human VEGF ELISA kit (R&D Systems) according to the manufactures protocol.

Conjugation and ^{89}Zr-labeling of bevacizumab

Conjugation and labeling of bevacizumab were performed as described previously [13,16]. In short, the chelate desferrioxamine B (Df) (desferal, Novartis) was succinylated (*N*-sucDf), temporarily filled with stable iron [Fe(III)], and coupled to the lysine residues of bevacizumab by means of a tetrafluorophenol-*N*-sucDf ester. Conjugation was performed at room temperature for 30 minutes at pH 9.5-9.7. After conjugation, the mixture was set to pH 4.2-4.4 (0.1 mol/L H_2SO_4) and 50 µL of 25 mg/mL ethylenediaminetetraacetic acid (EDTA) (Calbiochem) were added to remove Fe(III). The solution was incubated 30 min at 35°C, and purified by ultrafiltration, diluted in water for injection (5 mg/mL) and stored at -20°C.

Labeling was performed with ^{89}Zr ($T_{1/2}$ 3.27 days) produced by Cyclotron BV (Amsterdam, the Netherlands). In brief, the ^{89}Zr-oxalate solution was set at pH 3.9-4.2 and mixed for 3 min. With 4-(2-hydroxyethyl)-1-piperazineethanesulfonic acid (HEPES) (Sigma-Aldrich) buffer the solution was adjusted to pH 6.7-6.9. N-sucDf-bevacizumab was added and incubated for 45 min at room temperature. Before animal administration, extensive quality control of ^{89}Zr-bevacizumab was performed as described previously [13].

Animals

Tumor cells for xenografting were harvested by trypsinization and resuspended in RPMI 1640 and Matrigel™ (BD Bioscience). *In vivo* imaging and *ex vivo* biodistribution experiments were conducted using male nude Balb-c mice (Balb/cOlaHSD-foxn^{nu}) obtained from Harlan Nederland. At 6-8 weeks of age the mice were injected subcutaneously with $5x10^6$ A2780 or CP70 cells mixed with 0.1 mL Matrigel™. When the tumor measured between 6-8 mm in diameter (± 0.3 cm^3, for A2780 2 weeks after injection, for CP70 3-4 weeks after injection) *in vivo* studies were started.

MicroPET imaging and *ex vivo* biodistribution

^{89}Zr-bevacizumab (4 ± 0.27 MBq, ± 5 μg) was injected intravenously into the penile vein. During a scan sequence images were made 24 h and 144 h post injection of the tracer. Two scan sequences were performed, before and following NVP-AUY922 treatment. Animals were imaged using a MicroPET Focus 220 rodent scanner (CTI Siemens). Static images of 30 min acquisition time were obtained. After image reconstruction, *in vivo* quantification was performed with AMIDE Medical Image Data Examiner software (version 0.9.1, Stanford University, Stanford, CA) [17]. For the quantification of radioactivity within the tumor, 3D volumes of interest (VOIs) were manually drawn. The total injected dose was calculated by decay correction of the total activity present at 24 h after injection in the animal, at which time the clearance of the injected antibodies is considered to be almost negligible, as described earlier [13]. The data is presented as the percentage injected dose per gram tissue (%ID/g), assuming a tissue density of 1 g/cm^3. Animals were sacrificed after the last scan (144 h, second scan sequence) and organs and tissues were excised, rinsed for residual blood and weighed. Samples and primed standards were counted for radioactivity in a calibrated well-type LKB-1282-Compu-gamma system (LKB Wallac) and corrected for physical decay. Tissue activity is expressed as percentage of the injected dose per gram tissue (%ID/g). Harvested tumors were divided, immediately frozen at -80°C and paraffin embedded for further analysis.A2780 tumors are growing rapidly, with a doubling time of

3-6 days [6,18-20]. It was considered unachievable to maintain these tumors in the untreated animals for the duration of the drug treatment of the other animals, because the tumors would grow unacceptably large. Therefore, for *ex vivo* comparison non-treated control animals were sacrificed after the first administration of ^{89}Zr-bevacizumab, comparable to the pre-treatment scan of the NVP-AUY922 treated animals. Non-treated control animals (A2780 n=6, CP70 n=5) were injected with ^{89}Zr-bevacizumab (4 ± 0.27 MBq, ± 5 μg) and mice were sacrificed 144 h post injection of tracer. *Ex vivo* biodistribution was performed as described above.

All animal experiments were performed with isofluran inhalation anesthesia (induction 3%, maintenance 1.5%).

NVP-AUY922 treatment

NVP-AUY922 was formulated in water containing 5% glucose and administrated at 50 mg/kg twice weekly (2 qw) intraperitoneally (volume 6.5 ml/kg). Treatment was started immediately after the first (pre-treatment) scan sequence (A2780 n=8, CP70 n=6). Following 2 weeks of treatment, mice received a second administration of ^{89}Zr-bevacizumab and a second scan sequence was performed. NVP-AUY922 treatment was continued during this sequence.

All animal experiments were approved by the animal experiments committee of the University of Groningen.

Determination of anti-angiogenic response

From frozen tumors, 3 random samples were lysed manually using mammalian protein extraction reagent (M-PER, Pierce). Thereafter, mixtures were centrifuged at 20,000 g for 15 min and subsequently stored at -20°C until analysis. The protein concentration of the samples was determined by a Bradford assay [21]. VEGF levels were measured as described above. Data is presented as pg VEGF/mg protein.

Paraffin-embedded tumors were stained with antibodies against von Willebrand factor (vWf) and Ki67 (Dako) and hematoxylin and eosin staining (HE). The mean vessel density (MVD) was scored in 3 areas, defined as hot spot areas with the maximum number of microvessels, as described earlier [13]. The proliferation index was calculated by percentage of Ki67 positive cells in at least 3 high power fields (400x) using a calibrated grid. HE staining was performed to assess areas of necrosis. Areas were scored as percentage necrosis and vital tumor tissue per slide.

Statistical analysis. Data is presented as means ± standard error of the mean (SEM). Statistical analysis was performed using the Mann-Whitney test for non-parametric data and a paired sampled T-test for paired data (SPSS, version 14, Chicago, IL). A *P*-value ≤ 0.05 was considered significant.

Results

NVP-AUY922 decreases VEGF secretion in A2780 cells *in vitro*

Following 24 h incubation, VEGF levels in the culture medium of non-treated A2780 cells were higher (1.8 fold) compared to levels in the culture medium of non-treated CP70 cells (P=0.042). Treatment of the A2780 cells with 50 nM NVP-AUY922 for 24 h resulted in 43.2% (P=0.038) reduction of VEGF levels in the culture medium versus culture medium of non-treated cells (Figure 1). VEGF levels in the culture medium of CP70 cells were not significantly decreased (namely 23.8% lower, P=0.20). Increased doses of NVP-AUY922 up to 100 nM did not further reduce VEGF secretion by A2780 or CP70 cells.

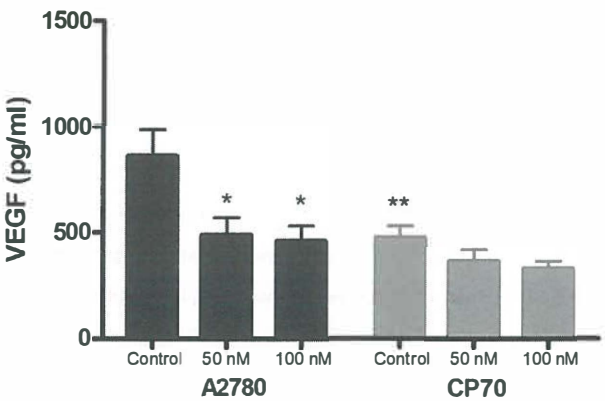

Figure 1. Effect of HSP90 inhibition by NVP-AUY922 on VEGF secretion. A2780 and CP70 tumor cells were incubated for 24 hours in 50 and 100 nM NVP-AUY922, or control medium (* $P < 0.05$). Control VEGF levels of A2780 cells were higher compared to control CP70 (** $P < 0.05$). *Data is presented as mean ± SEM.*

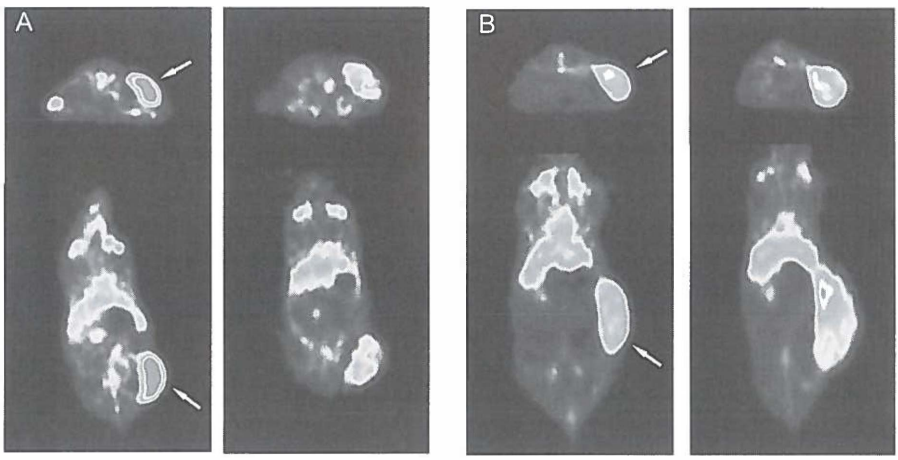

Figure 2. Representative transversal and coronal microPET images of ^{89}Zr-bevacizumab obtained pre-treatment of A2780 (A) and CP70 (B) xenografts (left panels), and following NVP-AUY922 treatment (right panels). Images were obtained 144 h after injection of ^{89}Zr-bevacizumab. Tumor is indicated by arrow. (see page 153 for color figure)

^{89}Zr-bevacizumab uptake decreases in A2780 tumors after NVP-AUY922 treatment

PET imaging 144 h post injection showed clear tumor localization of ^{89}Zr-bevacizumab in the A2780 and CP70 xenograft model (Figure 2). ^{89}Zr-bevacizumab uptake was homogeneous within the tumor. Pre-treatment, ^{89}Zr-bevacizumab tumor uptake in A2780 xenografts (12.9 ± 2.2 %ID/g, 144 h post injection) was higher ($P < 0.0001$) than in CP70 xenografts (6.9 ± 1.0 %ID/g). Treatment with 50 mg/kg 2 qw NVP-AUY922 week decreased ^{89}Zr-bevacizumab uptake with 44.4% (P=0.0003) compared to pre-treatment, as quantified 144 h post injection of ^{89}Zr-bevacizumab by microPET (Figure 3). Similar results were seen in *ex vivo* biodistribution experiments, in which ^{89}Zr-bevacizumab uptake was 47.8% lower (P=0.029) in NVP-AUY922 treated versus non-treated animals (Figure 4A). A2780 tumors are reported to grow rapidly, with a doubling time of 3-6 days [6,18-20]. In our study, volumes (assessed by microPET, which correlated nicely with *ex vivo* tumor weight (r^2=0.95)) of NVP-AUY922 treated A2780 tumors increased only moderately (2.2 ± 0.2 fold) during the study period (3 weeks), indicating an effect of NVP-AUY922 on tumor growthIn contrast to A2780, treatment with NVP-AUY922 did not change ^{89}Zr-bevacizumab tumor uptake in CP70 xenografts compared to pre-treatment tumor uptake (namely an increase of 8%,

P=0.475) as quantified by microPET (Figure 3). Similar results were seen with *ex vivo* biodistribution studies of non-treated versus treated CP70 tumors (27% increase, *P*=0.125). Tumor volumes increased 2.1 ± 0.5 during the study period (3 weeks), which is comparable to the growth rate before the start of the study in that time. Treatment with NVP-AUY922 did not change normal organ (non-tumor) biodistribution of ^{89}Zr-bevacizumab between treated and non treated tumor bearing mice (all organs *P* > 0.05)(Figure 4C).

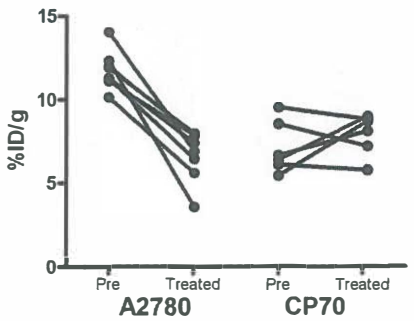

Figure 3. Individual microPET quantification of A2780 and CP70 xenografts pre- and following NVP-AUY922 treatment.

^{89}Zr-bevacizumab imaging corresponds with tumor VEGF levels in A2780 and CP70 xenografts pre and post NVP-AUY922 treatment

To verify that changes in ^{89}Zr-bevacizumab tumor uptake were VEGF driven, tumor VEGF levels of non-treated control mice were compared with VEGF levels of NVP-AUY922 treated (50 mg/kg, 2 qw) mice in both A2780 and CP70 xenografts by quantitative ELISA. In A2780 xenografts, tumor VEGF levels were 69% lower (*P*=0.041) after NVP-AUY922 treatment, while no significant change of VEGF levels was found in CP70 (20% reduction, *P*=0.608). These results correspond with ^{89}Zr-bevacizumab tumor uptake as assessed by biodistribution in these animals (Figure 4A). Both ^{89}Zr-bevacizumab tumor uptake and tumor VEGF levels are lower after NVP-AUY922 treatment in A2780 xenografts compared to controls, while this is not the case for CP70 xenografts. Furthermore, higher initial VEGF levels in A2780 versus CP70 are in line with the ^{89}Zr-bevacizumab biodistribution findings in these animals. In the present study microPET quantification was comparable with *ex vivo* biodistribution (Figure 4B), as described earlier [13]. Therefore, these results demonstrate that

changes in ^{89}Zr-bevacizumab microPET imaging correspond with changes in tumor VEGF levels by NVP-AUY922 mediated HSP90 inhibition.

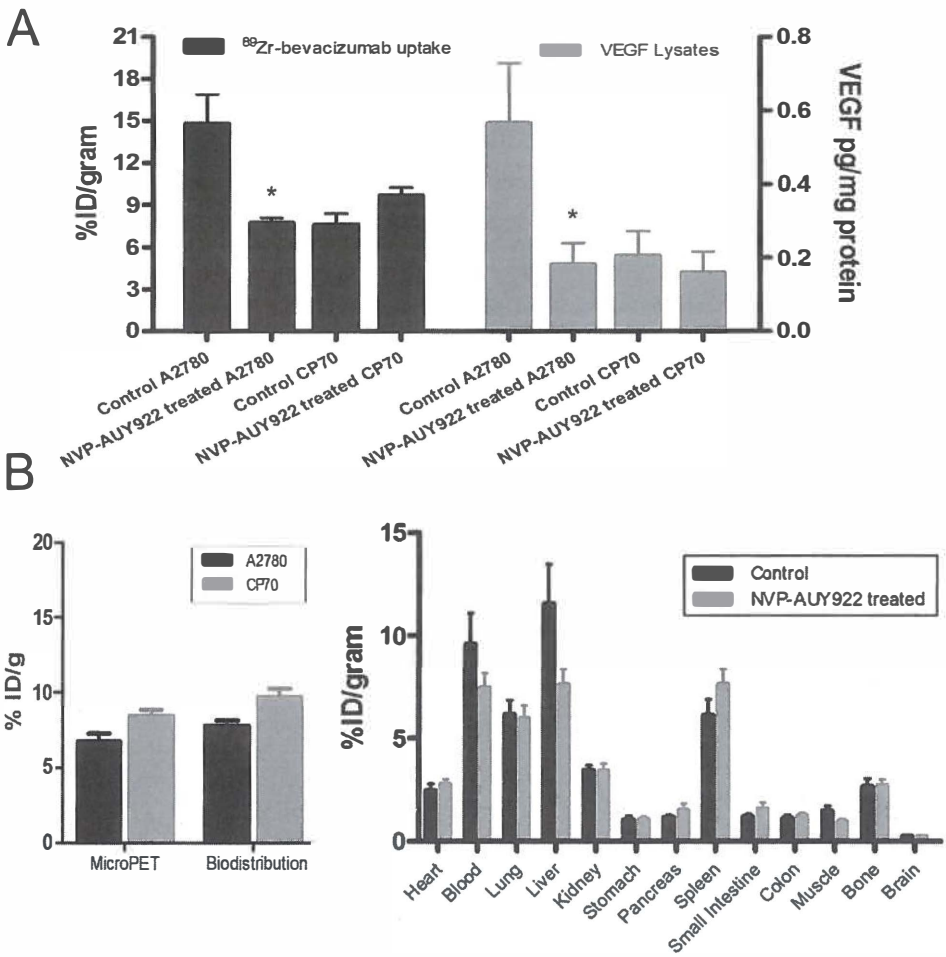

Figure 4. (A) *Ex vivo* tumor biodistribution of ^{89}Zr-bevacizumab and tumor lysate VEGF levels in control and NVP-AUY922 treated A2780 and CP70 xenografts (* $P < 0.05$). (B) MicroPET quantification and *ex vivo* biodistribution of ^{89}Zr-bevacizumab after NVP-AUY922 treatment, and *ex vivo* organ biodistribution (right) of ^{89}Zr-bevacizumab in control (n=11) and NVP-AUY922 treated (n=14) animals. *Data is presented as mean ± SEM.*

NVP-AUY922 treatment decreases MVD and Ki67 staining in responding A2780 tumors

The MVD was 60% lower (P=0.005) in NVP-AUY922 treated A2780 tumors compared to non-treated tumors (Figure 5). This shows that in A2780 tumors a decrease in VEGF secretion is accompanied by an anti-angiogenic effect in A2780, as determined histological, after NVP-AUY922. Additionally, anti-proliferative effects were seen in A2780 xenografts (proliferation index reduced by 35%, P=0.023), indicating that also a direct tumor effect occurred parallel to anti-angiogenic effects after NVP-AUY922 treatment (Figure 5). In CP70 tumors no differences in MVD (P=0.720) and proliferation rate (P=0.688) were observed, which is compatible with the findings on ^{89}Zr-bevacizumab PET imaging and tumor VEGF levels in this tumor cell line (data not shown).

Furthermore, in neither A2780 nor CP70 xenografts, two weeks of NVP-AUY922 treatment resulted in increased tumor necrosis as shown by HE staining. In NVP-AUY922 treated as well as non-treated xenografts at least 80% of the tumor consisted of vital areas (Figure 5). Therefore, decreased ^{89}Zr-bevacizumab tumor uptake in A2780 was not due to increased tumor necrosis.

Discussion

In the present study, we have demonstrated that the anti-angiogenic effect of HSP90 inhibition can be adequately monitored *in vivo* using ^{89}Zr-bevacizumab PET. The specificity of the technique is illustrated by the fact that a decreased ^{89}Zr-bevacizumab uptake is related to the presence of an anti-angiogenic response (confirmed by means of decreased VEGF levels and MVD) in the A2780 model, while no change in ^{89}Zr-bevacizumab uptake was observed in the nonresponsive CP70 model. Additionally, the extent of anti-angiogenic response was related to the anti-proliferative effect of the NVP-AUY922 treatment. Thus, ^{89}Zr-bevacizumab PET allows *in vivo* visualization and quantification of early anti-angiogenic tumor response to treatment with HSP90 inhibition. As such, it may be used as an early biomarker for the effect of HSP90 inhibition.

It is thought that reduction of VEGF secretion by tumor cells following HSP90 inhibition is mediated via multiple pathways. For example, HSP90 inhibition by 17-AAG reduced EGF, IGF-1, betacellulin, transforming growth factor α (TGF-α) and heregulin β1 induced VEGF secretion by tumor cells in vitro [7,9,11]. In prostate cancer cells geldanamycin treatment decreased HIF1α levels which corresponded with lower VEGF levels *in vitro* [8].

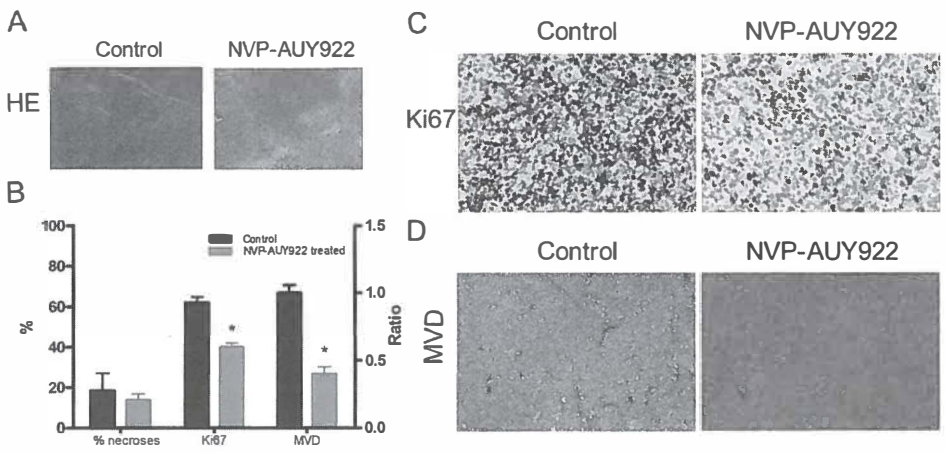

Figure 5. (A) Representative HE staining, (C) representative Ki67 staining, (B) % necroses, Ki67 staining and MVD (right Y-axis) (*$P < 0.05$) and (D) representative vWf staining for MVD of control and NVP-AUY922 treated A2780 xenograft. *Data is presented as mean ± SEM.* (see page 153 for color figure)

In addition, HSP90 inhibition has demonstrated anti-angiogenic effect *in vivo*. We observed in our A2780 xenograft model, a decreased MVD after NVP-AUY922 treatment. Similar effects were observed in a human glioblastoma xenograft model [6]. Furthermore, it was shown that NVP-AUY922 inhibited endothelial cell (EC) function and migration, decreased VEGF-R2 levels on ECs and reduced HIF1α levels in a human glioblastoma xenograft model [6]. These results are comparable to the effects seen with other HSP90 inhibitors. Treatment with 17-AAG and 17-(dimethylaminoethyl-amino)-17-demethoxygeldanamycin (17-DMAG; alvespimycin), a water soluble geldanamycin analogue, decreased MVD in gastric, colon and hepatocellular carcinoma xenograft models [7,11,22,23]. Additionally, 17-DMAG down-regulated VEGF-R2 protein expression on ECs, inhibited VEGF-A induced Erk and Akt activation, and down-regulated total-Akt expression [24]. Furthermore, treatment with 17-DMAG decreased PDGF-Rβ expression and function on vascular smooth muscle cells [24]. All these results signify the anti-angiogenic effect of HSP90 inhibition in cancer. In the present study we investigated whether this anti-angiogenic effect by HSP90 inhibition could be monitored by ^{89}Zr-bevavizumab PET imaging. Previously, it was shown that NVP-AUY922 treatment induced HSP70 and decreased CRAF and cyclin-dependent kinase 4 (CDK4) in A2780 cells, indicating sufficient sensitivity of this cell line to HSP90 inhibition [6].

We treated A2780 and CP70 tumor bearing mice with comparable dosing schemes which showed efficiency in other xenograft models [6,15]. Daily dosing of 50 mg/kg NVP-AUY922 during 7 days reduced tumor growth by 90% in A2780 xenografts compared to non-treated animals [6]. We showed with microPET quantification a vast decrease of ^{89}Zr-bevacizumab tumor uptake in A2780 xenografts, whereas no decrease in ^{89}Zr-bevacizumab uptake was seen in CP70 xenografts. Previously, we showed that ^{89}Zr-bevacizumab accumulates in tumor blood vessels and its extracellular matrix, presumably due to localization of large VEGF isoforms [12,13]. To verify whether changes in ^{89}Zr-bevacizumab uptake also reflect changes in total tumor VEGF levels, we assessed VEGF levels in tumor lysates. The *ex vivo* VEGF ELISA we used, detects both extra- and intra cellular VEGF in tumor lysates. Most likely, equilibrium is present between extracellular and intracellular VEGF. VEGF levels in A2780 xenograft were higher compared to CP70 xenografts and they decreased after HSP90 inhibition, whereas VEGF levels in CP70 did not change. These results are in line with our ^{89}Zr-bevacizumab imaging results and demonstrate that ^{89}Zr-bevacizumab microPET imaging can quantify non-invasively both absolute differences between VEGF levels in tumors, as well as changes in VEGF levels after therapy.

These *in vivo* results mimic our in vitro experiments, in which initial CP70 VEGF secretion levels were lower compared to A2780 VEGF secretion and no significant effect of HSP90 therapy was observed. It is not completely clear why CP70 did not respond to HSP90 inhibition, and why initial VEGF levels were lower compared to A2780. Several studies have demonstrated a complex interaction between cisplatin and HSP90. Cisplatin can bind to the C-terminal domain of HSP90 promoting a conformational change in HSP90, whereas HSP90 inhibitors interact with the N-terminal domain of HSP90 [25]. Combined treatment of cisplatin and HSP90 inhibition has shown additive as well as antagonistic effects in colon and ovarian tumor cell lines [18,26,27]. For instance, in A2780 tumor cells concomitant administration of 17-AAG and carboplatin was antagonistic *in vitro*, while 17-AAG followed by carboplatin or vice versa was additive both in vitro and *in vivo* [18]. Future studies should elucidate the interaction between cisplatin and HSP90 therapy in both cisplatin sensitive and resistant models. This complexity does however point to the relevance of an early predictive factor [28].

Other client proteins that have been used for non-invasive monitoring of HSP90 therapy are HER2 and EGFR. Smith-Jones et al. demonstrated that the early degradation of HER2 (-50%) during 17-AAG therapy could be monitored by microPET imaging in a BT474 breast cancer xenograft model, using ^{68}Ga-DCHF, a F(Ab')$_2$ fragment of the HER2 antibody trastuzumab [29,30]. Furthermore, decreased HER2 expression measured by microPET

corresponded with reduced tumor growth. In contrast, tumor uptake of ^{18}FDG (the most widely used tumor tracer which visualizes glucose uptake) did not change after HSP90 therapy [30]. Likewise, ^{64}Cu-DOTA-cetuximab was used to monitor EGFR degradation by 17-AAG in a PC-3 prostate cancer xenograft model [31]. Uptake of ^{64}Cu-DOTA-cetuximab in 17-AAG treated animals was lower (-39%) compared to non-treated animals 48 hours after the last administration of 17-AAG, which corresponded with a decreased EGFR staining in tumor samples. In contrast to EGFR and HER2, that are abundantly expressed in a selected group of cancer patients, VEGF plays an important, universal role in cancer and therefore ^{89}Zr-bevacizumab imaging might be more widely applicable to monitor HSP90 inhibition. Exploration of ^{89}Zr-bevacizumab PET imaging in phase II studies as an early predictive marker during HSP90 inhibition has been started.

Acknowledgments

This study was supported by a personal grant to W.B. Nagengast and grants RUG 2007-3739 and RUG 2009-4273 of the Dutch Cancer Society.

References

1. Ferrara, N. & Davis-Smyth, T. The biology of vascular endothelial growth factor. *Endocr. Rev.* 18, 4-25 (1997).
2. Gerber, H. P. & Ferrara, N. Pharmacology and pharmacodynamics of bevacizumab as monotherapy or in combination with cytotoxic therapy in preclinical studies. *Cancer Res.* 65, 671-680 (2005).
3. Xu, W. & Neckers, L. Targeting the molecular chaperone heat shock protein 90 provides a multifaceted effect on diverse cell signaling pathways of cancer cells. *Clin. Cancer Res.* 13, 1625-1629 (2007).
4. Neckers, L. Heat shock protein 90: the cancer chaperone. *J. Biosci.* 32, 517-530 (2007).
5. Kamal, A. *et al.* A high-affinity conformation of Hsp90 confers tumour selectivity on Hsp90 inhibitors. *Nature* 425, 407-410 (2003).
6. Eccles, S. A. *et al.* NVP-AUY922: a novel heat shock protein 90 inhibitor active against xenograft tumor growth, angiogenesis, and metastasis. *Cancer Res.* 68, 2850-2860 (2008).
7. Sanderson, S. *et al.* Benzoquinone ansamycin heat shock protein 90 inhibitors modulate multiple functions required for tumor angiogenesis. *Mol. Cancer Ther.* 5, 522-532 (2006).
8. Alqawi, O., Moghaddas, M. & Singh, G. Effects of geldanamycin on HIF-1alpha mediated angiogenesis and invasion in prostate cancer cells. *Prostate Cancer Prostatic. Dis.* 9, 126-135 (2006).
9. Lang, S. A. *et al.* Targeting heat shock protein 90 in pancreatic cancer impairs insulin-like growth factor-I receptor signaling, disrupts an interleukin-6/signal-transducer and activator of transcription 3/hypoxia-inducible factor-1alpha autocrine loop, and reduces orthotopic tumor growth. *Clin. Cancer Res.* 13, 6459-6468 (2007).
10. Cao, X. *et al.* Non-invasive MRI tumor imaging and synergistic anticancer effect of HSP90 inhibitor and glycolysis inhibitor in RIP1-Tag2 transgenic pancreatic tumor model. *Cancer Chemother. Pharmacol.* (2008).
11. Lang, S. A. *et al.* Inhibition of heat shock protein 90 impairs epidermal growth factor-mediated signaling in gastric cancer cells and reduces tumor growth and vascularization *in vivo*. *Mol. Cancer Ther.* 6, 1123-1132 (2007).
12. Park, J. E., Keller, G. A. & Ferrara, N. The vascular endothelial growth factor (VEGF) isoforms: differential deposition into the subepithelial extracellular matrix and bioactivity of extracellular matrix-bound VEGF. *Mol. Biol. Cell* 4, 1317-1326 (1993).
13. Nagengast, W. B. *et al. In vivo* VEGF imaging with radiolabeled bevacizumab in a human ovarian tumor xenograft. *J. Nucl. Med.* 48, 1313-1319 (2007).
14. Nagengast, W. B. *et al.* Towards clinical VEGF imaging using the anti-VEGF antibody bevacizumab and Fab-fragment ranibizumab. Vol 26, No 15S, 2008-3547. 2008. Proc. Am. Soc. Clin. Oncology. Ann. Meeting. Ref Type: Generic
15. Jensen, M. R. *et al.* NVP-AUY922: a small molecule HSP90 inhibitor with potent antitumor activity in preclinical breast cancer models. *Breast Cancer Res.* 10, R33 (2008).
16. Verel, I. *et al.* Long-lived positron emitters zirconium-89 and iodine-124 for scouting of therapeutic radioimmunoconjugates with PET. *Cancer Biother. Radiopharm.* 18, 655-661 (2003).
17. Loening, A. M. & Gambhir, S. S. AMIDE: a free software tool for multimodality medical image analysis. *Mol. Imaging* 2, 131-137 (2003).
18. Banerji, U. *et al.* An in vitro and *in vivo* study of the combination of the heat shock protein inhibitor 17-allylamino-17-demethoxygeldanamycin and carboplatin in human ovarian cancer models. *Cancer Chemother. Pharmacol.* (2008).
19. Arts, J. *et al.* R306465 is a novel potent inhibitor of class I histone deacetylases with broad-spectrum antitumoral activity against solid and haematological malignancies. *Br. J. Cancer* 97, 1344-1353 (2007).

20. Taylor, S. A. *et al.* Combining the farnesyltransferase inhibitor lonafarnib with paclitaxel results in enhanced growth inhibitory effects on human ovarian cancer models in vitro and *in vivo*. *Gynecol. Oncol*. 109, 97-106 (2008).
21. Bradford, M. M. A rapid and sensitive method for the quantitation of microgram quantities of protein utilizing the principle of protein-dye binding. *Anal. Biochem*. 72, 248-254 (1976).
22. Moser, C. *et al.* Blocking heat shock protein-90 inhibits the invasive properties and hepatic growth of human colon cancer cells and improves the efficacy of oxaliplatin in p53-deficient colon cancer tumors *in vivo*. *Mol. Cancer Ther.* 6, 2868-2878 (2007).
23. Park, J. H. *et al.* Class II histone deacetylases play pivotal roles in heat shock protein 90-mediated proteasomal degradation of vascular endothelial growth factor receptors. *Biochem. Biophys. Res. Commun.* 368, 318-322 (2008).
24. Lang, S. A. *et al.* Targeting heat-shock protein 90 improves efficacy of rapamycin in a model of hepatocellular carcinoma in mice. *Hepatology* (2008).
25. Marcu, M. G. & Neckers, L. M. The C-terminal half of heat shock protein 90 represents a second site for pharmacologic intervention in chaperone function. *Curr. Cancer Drug Targets.* 3, 343-347 (2003).
26. Vasilevskaya, I. A., Rakitina, T. V. & O'Dwyer, P. J. Quantitative effects on c-Jun N-terminal protein kinase signaling determine synergistic interaction of cisplatin and 17-allylamino-17-demethoxygeldanamycin in colon cancer cell lines. *Mol. Pharmacol.* 65, 235-243 (2004).
27. Bagatell, R., Beliakoff, J., David, C. L., Marron, M. T. & Whitesell, L. Hsp90 inhibitors deplete key anti-apoptotic proteins in pediatric solid tumor cells and demonstrate synergistic anticancer activity with cisplatin. *Int. J. Cancer* 113, 179-188 (2005).
28. Oldenhuis, C. N., Oosting, S. F., Gietema, J. A. & De Vries, E. G. Prognostic versus predictive value of biomarkers in oncology. *Eur. J. Cancer* 44, 946-953 (2008).
29. Smith-Jones, P. M. *et al.* Imaging the pharmacodynamics of HER2 degradation in response to Hsp90 inhibitors. *Nat. Biotechnol.* 22, 701-706 (2004).
30. Smith-Jones, P. M., Solit, D., Afroze, F., Rosen, N. & Larson, S. M. Early tumor response to Hsp90 therapy using HER2 PET: comparison with 18F-FDG PET. *J. Nucl. Med.* 47, 793-796 (2006).
31. Niu, G., Cai, W., Chen, K. & Chen, X. Non-invasive PET imaging of EGFR degradation induced by a heat shock protein 90 inhibitor. *Mol. Imaging Biol.* 10, 99-106 (2008).

Chapter 6A

VEGF-SPECT with ^{111}In-bevacizumab in stage III/IV melanoma patients

Wouter B. Nagengast[1], Marjolijn N. Lub-de Hooge[3,5], Esther M.E. van Straten[1], Adrienne H. Brouwers[3], Wilfred F.A. den Dunnen[4], Johan R. de Jong[3], Harry Hollema[4], Rudi A. Dierckx[3], Nanno H. Mulder[1], Elisabeth G.E. de Vries[1], Harald J. Hoekstra[2], Geke A.P. Hospers[1]

Departments of Medical Oncology[1], Surgery[2], Nuclear Medicine and Molecular Imaging[3] Pathology[4] and Hospital Pharmacy[5], University Medical Center Groningen, The Netherlands

In progress

Abstract

Purpose: A feasibility study was performed to investigate the presence of VEGF in melanoma lesions by VEGF-SPECT with ^{111}In-bevacizumab. Additionally, VEGF-SPECT tumor visualization was compared with CT and FDG-PET imaging.

Patients and Methods: Eligible were patients with stage III/IV melanoma who presented with nodal recurrent disease. VEGF-SPECT was performed after administration of 100 Mbq ^{111}In-bevacizumab (8 mg) at days 0, 2, 4 and 7 post injection. Tumor visualization was compared with CT and FDG-PET imaging.

Results: Nine patients were included. FDG-PET and CT detected each in total 12 nodal lesions. All lesions were also visualized by VEGF-SPECT. VEGF-SPECT tumor visualization was optimal at day 4 post injection of ^{111}In-bevacizumab. A 3-fold difference in ^{111}In-bevacizumab tumor uptake was detected among tumor lesions. In addition, ^{111}In-bevacizumab uptake varied between tumor lesions within patients and within lesions.

Conclusion: VEGF-SPECT could visualize melanoma lesions, comparable to CT and FDG-PET. Future studies should elucidate the role of VEGF-SPECT in the selection of patients for anti-angiogenic therapy.

Introduction

Tumor angiogenesis, the forming of new blood vessels, is a continuous process which allows tumor cells to execute their critical growth by supplying the tumor with nutrients and oxygen, disposing of metabolic waste products and providing a route for metastatic spreading [1,2]. Vascular endothelial growth factor A (VEGF-A) is one of the key growth factors involved in the development and maintenance of tumor angiogenesis [3]. Bevacizumab, a fully humanized monoclonal antibody, binds to all VEGF-A isoforms with high affinity and thereby blocks ligand-receptor signaling [4]. Bevacizumab was the first anti-angiogenic therapy shown to be clinically effective in metastatic colon cancer, breast and lung cancer combined when with conventional chemotherapy [5-7].

Melanoma causes more than 75% of all skin cancer deaths. Melanoma features a specific metastatic spread from primary tumor to regional lymphatic beds and then distant metastases [8,9]. When patients present with lymph node or distant metastases their prognosis is worse, with 5 year survival rates of respectively 47% and 10% [10,11].

Several factors point to a role for VEGF in melanoma. Melanoma cells produce high amounts of VEGF-A which correlates with advanced disease, tumor burden, poor overall survival and probability of progression [12]. Furthermore, VEGF-A expression in nodal metastases is higher compared to primary tumors indicating the importance of a pro-angiogenic switch in the process of melanoma progression [8]. In addition, pre-clinical studies in mice have demonstrated up-regulation of pro-inflammatory chemokines in the lung parenchyma by VEGF-A production of the primary melanoma lesion, thereby contributing to the 'seed and soil' of metastasis [13,14]. For these reasons, the use of anti-VEGF targeted therapies is of potential interest in the treatment of melanoma patients. The first clinical studies in metastatic melanoma patients showed low activity of VEGF-A antibody bevacizumab combined with interferon-2α, but encouraging responses have been observed clinically when bevacizumab was combined with chemotherapy [15-17].

Currently, no biomarkers are available to determine the presence of a drug target for anti-angiogenic drugs across tumor lesions in patients to predict anti-tumor efficiency. A potentially attractive method is the use of non-invasive visualization of *in vivo* biological processes by nuclear medicine imaging techniques. A new option in this field is molecular VEGF imaging. VEGF consists of at least 4 splice variants, containing 121, 165, 189 and 206 amino acids [3]. $VEGF_{121}$ is freely soluble, $VEGF_{165}$ is partly secreted, while a significant fraction remains localized to the extra cellular matrix and cell surface, like $VEGF_{189}$ and $VEGF_{206}$ resulting in high concentrations in the tumor microenvironment [18-22]. These isoforms are attractive imaging targets for VEGF imaging as this could provide non-

invasively insight in the local VEGF status and thereby be useful to guide anti-angiogenic therapy. Recently, *in vivo* measurement of VEGF tumor levels was made possible by using radionuclide VEGF imaging [23-27].

In the present study we investigated the feasibility of VEGF visualization of melanoma lesions with SPECT using ^{111}In-bevacizumab as tracer. In addition, we compared VEGF-SPECT with standard CT and ^{18}F-FDG PET imaging [28].

Patients and Methods

Patients

All eligible patients who visited the outpatient clinics of the University Medical Center Groningen (UMCG) between November-2007 till June-2009 were offered participation in the trial. Eligible patients were ≥ 18 years of age, had a WHO performance status of 0-2, with stage III/IV melanoma who presented with nodal recurrent disease.. They were excluded in case of prior immuno- or chemotherapy for metastatic disease, prior radiotherapy on the involved area or major surgery within 28 days of start of the study, any investigational drug within 30 days before start of the study, or clinical evidence of brain metastases.

Routine staging included a complete history, physical examination, and blood chemistry profile, in addition to CT-scan and FDG-PET scan. The study was approved by the local medical ethics committee and written informed consent was obtained from all participants. The study was registered under trial number NTR1941.

Study design

In the first 3 patients after ^{111}In-bevacizumab administration VEGF-SPECT scanning was evaluated at day 0, 2, 4 and 7. Hereafter patients were scanned at day 0, 4 and 7 post injection.

^{111}In-ITC-DTPA-Bevacizumab SPECT

Bevacizumab was conjugated with the chelator 2-(4-Isothiocyanatobenzyl)-diethylenetriaminepentaacetic acid (ITC-DTPA) (Macrocyclics) as described previously [23]. One batch of ITC-DTPA-bevacizumab conjugate was produced. This batch was tested for conjugation ratio, efficiency of the labeling, pH, immunoreactive fraction, sterility, and apyrogenicity. The purified conjugated bevacizumab was diluted (10 mg/mL) in ammonium acetate and stored at -80°C. ^{111}In labeling was performed separately for each patient. The final product had a radiochemical purity of ≥ 95%, was sterile and free from pyrogenes. The conjugation and labeling procedures were validated and performed under good manufacturing practice (GMP) conditions.

Scintigraphy was performed after administration of 100 ± 3 Mbq ^{111}In-bevacizumab (8 mg bevacizumab). Planar whole body imaging was performed, using a two-headed gamma camera, equipped with parallel-hole medium-energy collimators, at a scan speed of 10 cm/min (day 0 and 2 post injection (pi)) or 5 cm/min (day 4 and 7 pi) and stored digitally in a 256 x 1024 matrix. SPECT images were obtained from pre-defined tumor lesions, using 180 degrees sampling with 32 projections per head, 45 sec acquisition time per projection and a 128x128 matrix size.

Image and Data Analysis

SPECT reconstructions were performed with the ordered subset expectation maximization algorithm (OSEM). VEGF SPECT images were fused with conventional CT images to validate regions of increased ^{111}In-bevacizumab uptake. Tumor uptake quantification was performed with AMIDE Medical Image Data Examiner software (version 0.9.1, Stanford University) [29]. Quantification was performed using the day 4 scan which showed optimal tumor to background ratios. For the quantification of radioactivity within the tumor, 3D volumes of interest (VOIs) were drawn within the fused VEGF SPECT/CT image. ^{111}In-bevacizumab tumor accumulation was quantified as arbitrary counts per voxel. Both maximum uptake and mean tumor uptake were assessed. The mean reflects the mean value over all voxels, and the max reflects the maximum voxel value in the tumor. ^{18}F-FDG quantification was performed as described previously using the AMIDE Medical Image Data Examiner software; the Standardized Uptake Value was calculated according the following formula: SUV = radioactivity concentration in the tissue (bq/kg)/ (injected dose (bq)/ patient weight (kg)) [30]. Three dimensional VOIs were placed semi-automatically by using a threshold of 40% of the maximum value (SUVmax) in a pre-selected region.

Immunohistochemistry

Primary melanoma samples were obtained at initial diagnosis (n=9). Single and double immunofluorescence staining was performed on 3 μm-thick paraffin-embedded tumor slides with selected combinations of the primary antibodies rabbit anti-VEGF-A (1:50, Santa Cruz). Immunosignals were visualized using combinations of goat anti-mouse AlexaFluor 660 antibodies, donkey anti-rabbit AlexaFluor 488 antibodies or goat anti-mouse AlexaFluor 488 antibodies (1:400, all from Invitrogen). Nuclear staining was performed with bisbenzimide H 33258 fluorochrome (1:5000, Merck, Darmstadt, Germany). Slides were analyzed using a Leica DMRXA immunofluorescence microscope equipped with appropriate excitation and emission filters for maximum separation of Alexa Fluor 488 (e.g.

FITC), Alexa Fluor 660 (e.g. TRITC), and H33258 (e.g. DAPI). Images were captured with a Leica DC350 FX camera. Leica QWinPro software was used for evaluation of the slides (all from Leica Microsystems, Wetzlar, Germany). VEGF-A intensity (value 1-5) was scored at 400x magnification.

Statistics

Data is presented as means ± standard error of the mean (SEM). Statistical analysis was performed using the Mann-Whitney test for non-parametric data or a paired sampled T-test for paired data (SPSS, version 14). Associations between parameters were evaluated using Pearson's Correlation Test. A double side *P*-value ≤ 0.05 was considered significant.

Results

Patients characteristics

Nine patients were included. In these patients, 12 lymph node lesions were detected with CT and FDG PET imaging. No discrepancy existed between these imaging modalities. Six patients had 1 melanoma lesion, three patients had 2 lesions. In patients with more than 1 lesion, melanoma lesions were located in the same region of the body. No distant metastases, like liver or bone metastases, were detected. 4.6 fold differences existed between SUV FDG PET uptake among lesions, suggesting large differences in metabolic activity.

^{111}In-bevacizumab tumor visualization

Directly after administration, ^{111}In-bevacizumab was mainly located in the circulation and well perfused organs like heart and liver. As shown in Figure 1A, ^{111}In-bevacizumab activity in the circulation decreased from day 0 to day 7, whereas ^{111}In-bevacizumab tumor uptake increased resulting in clear tumor visualization. Tumor lesions became clearly visible from day 2 onwards, with increasing tumor to background ratios over time. At day 7, decay of ^{111}In resulted in relatively low count rates and therefore inferior image quality compared to day 4. For this reason, we concluded that day 4 after ^{111}In-bevacizumab injection was optimal for visualization and quantification of ^{111}In-bevacizumab uptake in the tumor. No infusion related reactions or adverse events were noticed during the study.

VEGF-SPECT imaging detected all known CT and FDG PET lesions. The smallest tumor lesion in a patient was 12 mm in diameter as measured by CT, located lateral at the thigh of a patient (Figure 2A). No new lesions were detected by VEGF-SPECT.

Quantification of ^{111}In-bevacizumab SPECT

A linear relation between maximum and mean ^{111}In-bevacizumab uptake was observed (respectively r^2=0.96, P < 0.0001). For this reason further analysis was performed using maximum tumor uptake value, which is not influenced by individual drawing of VOIs.

When we quantified the ^{111}In-bevacizumab tumor uptake, 3-fold differences in ^{111}In-bevacizumab maximum tumor uptake were observed between patients, suggesting large differences in VEGF levels (Figure 3A). Moreover, in individual patients, 40% difference in maximum ^{111}In-bevacizumab tumor uptake existed between tumor lesions. In addition, in one patient VEGF-SPECT demonstrated inhomogeneous tumor uptake within a melanoma lesion, 5.4 x 3.2 cm in size on CT (Figure 2C). No correlation existed between the ^{111}In-bevacizumab uptake and the ^{18}F-FDG tumor uptake (r^2=0.38, P=0.10).

Immunohistochemistry

All primary melanomas had a positive VEGF-A staining, though staining intensities ranged from weak to strong between patients (Figure 4). Five patients had a weak staining (score 1-2), two patients a moderate staining (score 3) and two patient a strong staining (score 4-5). No correlation was found between the VEGF-A staining in the tumor samples and the ^{111}In-bevacizumab uptake (P=0.38).

Discussion

In the present study we demonstrated that VEGF-SPECT visualized all known melanoma lymph node lesions identified by CT and FDG-PET imaging. A large variation in ^{111}In-bevacizumab tumor uptake was detected between patients, across lesions within patients and within lesions. This suggests differential presence of drug target for anti-VEGF targeted drugs between melanoma patients. Future studies should elucidate the role of VEGF-SPECT in the selection of patients who benefit of anti-angiogenic therapy.

To date, two anti-VEGF antibodies have been used for the clinical VEGF imaging: HumMV833 and bevacizumab [23,24,30,31]. Jayson et al used ^{124}I-HuMV833, a humanized monoclonal $IgG4_k$ antibody that binds $VEGF_{121}$ and $VEGF_{165}$, to perform PET-imaging studies in patients with various progressive solid tumors [30]. Tumor uptake of ^{124}I-HuMV833 was highly variable between and within patients. For example, there was high uptake of ^{124}I-HuMV833 in an ovarian tumor and low uptake in a poorly vascularized metastasis in a colon cancer patient [30]. These differences likely reflect the variation in VEGF secretion among tumor types and lesions. ^{111}In- and ^{89}Zr-bevacizumab showed specific tumor uptake in human ovarian, colon and melanoma xenograft models [23,24,26].

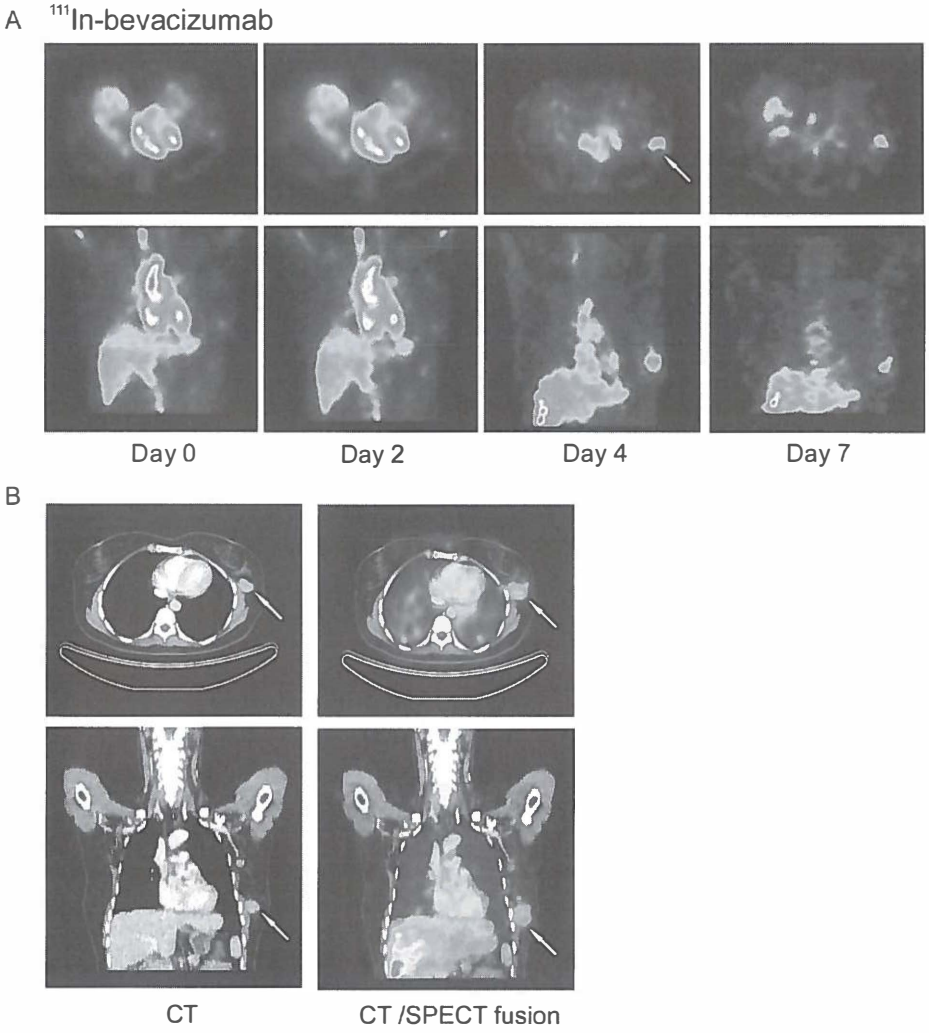

Figure 1. (A) Transversal and coronal VEGF-SPECT images at day 0, 2, 4 and 7 post injection of the tracer. In time, ^{111}In-bevacizumab accumulates in the tumor with optimal tumor to background ratio 4 days post injection. (B) Transversal and coronal CT image and VEGF SPECT/CT fusion 4 days post injection. (see page 154 for color figure)

In the present study we observed optimal tumor to background ratios 4 days post injection of ^{111}In-bevacizumab in melanoma patients, which is in concordance which ^{111}In radiolabeled trastuzumab, reflecting the relatively slow pharmacokinetics of monoclonal antibodies [32]. Directly after injection, ^{111}In-bevacizumab is mainly present in the circulation and well perfused organs. Non-specific liver uptake was seen for ^{111}In-bevacizumab, and was comparable to other radiolabeled antibodies, for example ^{111}In-trastuzumab [32]. Due to the

relatively slow clearance of ^{111}In-bevacizumab, extended tumor exposure takes place which results in maximal tumor accumulation whereas non-specific uptake in other organs decreases over time. In addition, the high production of VEGF by the tumor and subsequent high VEGF concentration in the micro-environment presumably lead to sensitive detection of tumor lesions by VEGF-SPECT. For these reasons, even lesions of around 1 cm in diameter were detectable. Most likely, radiolabeled bevacizumab binds to all VEGF-A isoforms located on the cell surface and the extra cellular matrix as has been proven pre-clinically in $VEGF_{165}$ and $VEGF_{189}$ over-expressing melanoma xenografts [26].

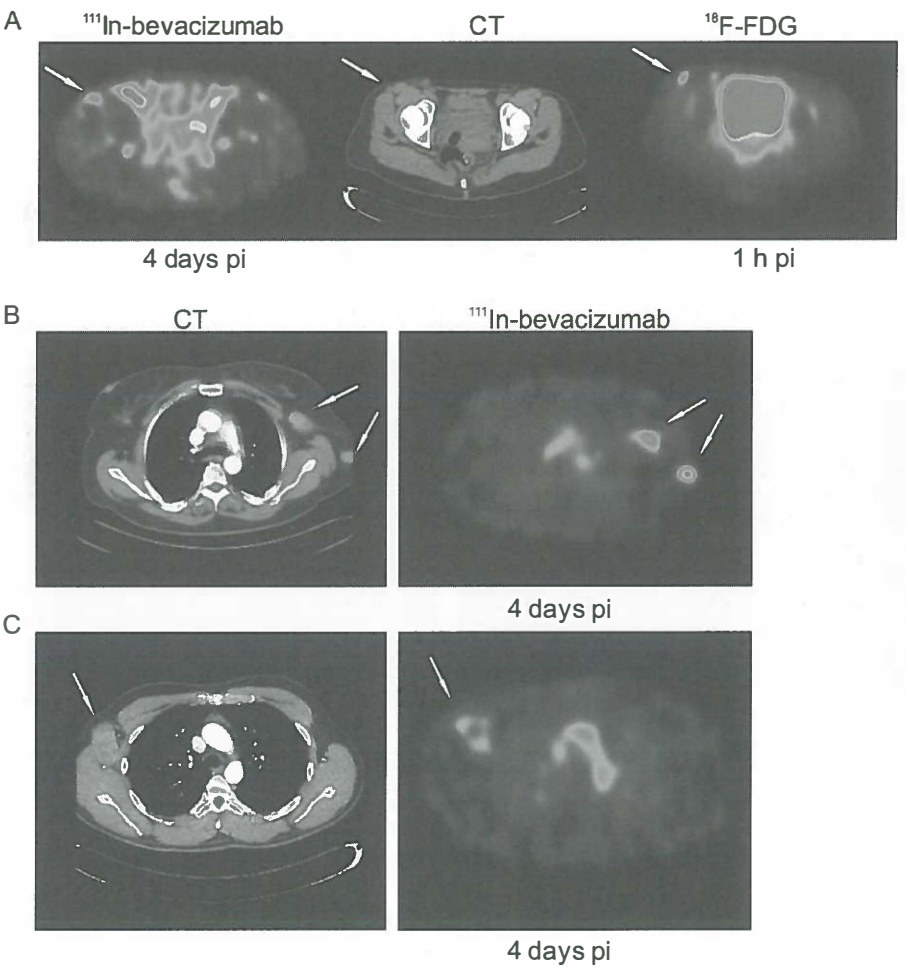

Figure 2. (A) Small melanoma lesions (white arrow), 12 mm in diameter on CT, detection by ^{111}In-bevacizumab, CT imaging and FDG imaging. (B) Differential ^{111}In-bevacizumab uptake between two melanoma lesions. (C) Inhomogeneous ^{111}In-bevacizumab tumor uptake in melanoma lesion. (see page 155 for color figure)

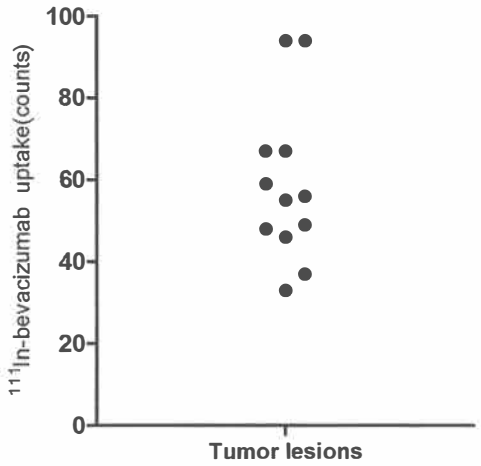

Figure 3. Maximal ^{111}In-bevacizumab tumor uptake per tumor lesion expressed as arbitrary counts per voxel at day 4 post injection of ^{111}In-bevacizumab.

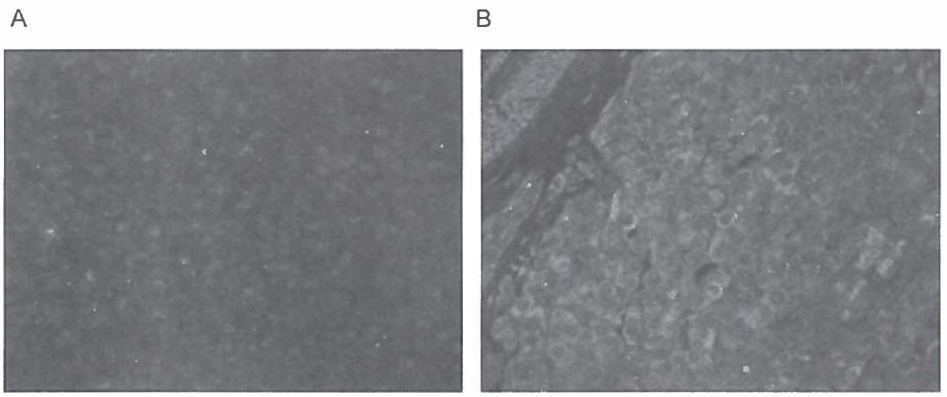

Figure 4. Weak (A) and strong (B) VEGF-A immunofluorescent staining of primary melanoma lesions. (see page 156 for color figure)

We did not observe a correlation between the VEGF staining in the primary melanoma and ^{111}In-bevacizumab uptake in the lymph node metastases. This could be due to the time between the biopsy of the primary tumor and disease progression (range 3 months-7 years). For example, it has been shown that VEGF-A expression in nodal metastases is higher compared to primary tumors [8].

When we looked at individual tumor lesions, large differences were detected in ^{111}In-bevacizumab uptake. This could be of interest since it has been shown that VEGF and VEGF-receptor expression in melanomas are associated with disease progression and response to anti-angiogenic treatment [33,34]. For instance, in melanoma patients response to sorafinib, an pan-VEGFR tyrosine kinase inhibitor, was associated with high VEGFR2 expression in the tumor before treatment as measured by immunohistochemistry [33]. Unfortunately, few tumor lesions are accessible for biopsy. Therefore there is a need for a non-invasive method to assess the angiogenic state of the tumor. VEGF imaging could facilitate in this. Future studies should elucidate the potential of VEGF imaging in the selection of high VEGF expressing tumors of individual patients at start of anti-angiogenic treatment. In this, ^{89}Zr-bevacizumab, allowing high resolution whole body quantitative PET imaging could further potentiate this imaging modality [23].

In conclusion, VEGF-SPECT is a feasible clinical imaging modality for the visualization of melanoma lymph node metastasis. VEGF imaging is a potential non-invasive biomarker in the selection of tumors that have high expression levels of VEGF.

References

1. Folkman, J. What is the evidence that tumors are angiogenesis dependent? *J. Natl. Cancer Inst.* 82, 4-6 (1990).
2. Folkman, J. & Klagsbrun, M. Angiogenic factors. *Science* 235, 442-447 (1987).
3. Ferrara, N. & Davis-Smyth, T. The biology of vascular endothelial growth factor. *Endocr. Rev.* 18, 4-25 (1997).
4. Gerber, H. P. & Ferrara, N. Pharmacology and pharmacodynamics of bevacizumab as monotherapy or in combination with cytotoxic therapy in preclinical studies. *Cancer Res.* 65, 671-680 (2005).
5. Gaudreault, J., Fei, D., Rusit, J., Suboc, P. & Shiu, V.. Preclinical pharmacokinetics of Ranibizumab (rhuFabV2) after a single intravitreal administration. *Invest Ophthalmol. Vis. Sci.* 46, 726-733 (2005).
6. Miller, K. *et al.* Paclitaxel plus bevacizumab versus paclitaxel alone for metastatic breast cancer. *N. Engl. J. Med.* 357, 2666-2676 (2007).
7. Sandler, A. *et al.* Paclitaxel-carboplatin alone or with bevacizumab for non-small-cell lung cancer. *N. Engl. J. Med.* 355, 2542-2550 (2006).
8. Gorski, D. H., Leal, A. D. & Goydos, J. S. Differential expression of vascular endothelial growth factor-A isoforms at different stages of melanoma progression. *J. Am. Coll. Surg.* 197, 408-418 (2003).
9. Tas, F. *et al.* Circulating serum levels of angiogenic factors and vascular endothelial growth factor receptors 1 and 2 in melanoma patients. *Melanoma Res.* 16, 405-411 (2006).
10. Bastiaannet, E. *et al.* Impact of [18F]fluorodeoxyglucose positron emission tomography on surgical management of melanoma patients. *Br. J. Surg.* 93, 243-249 (2006).
11. Sekulic, A. *et al.* Malignant melanoma in the 21st century: the emerging molecular landscape. *Mayo Clin. Proc.* 83, 825-846 (2008).

12. Ugurel, S., Rappl, G., Tilgen, W. & Reinhold, U. Increased serum concentration of angiogenic factors in malignant melanoma patients correlates with tumor progression and survival. *J. Clin. Oncol.* 19, 577-583 (2001).
13. Psaila, B. & Lyden, D. The metastatic niche: adapting the foreign soil. *Nat. Rev. Cancer* 9, 285-293 (2009).
14. Hiratsuka, S., Watanabe, A., Aburatani, H. & Maru, Y. Tumour-mediated upregulation of chemoattractants and recruitment of myeloid cells predetermines lung metastasis. *Nat. Cell Biol.* 8, 1369-1375 (2006).
15. Varker, K. A. *et al.* A randomized phase 2 trial of bevacizumab with or without daily low-dose interferon alfa-2b in metastatic malignant melanoma. *Ann. Surg. Oncol.* 14, 2367-2376 (2007).
16. Gonzalez-Cao, M. *et al.* Preliminary results of the combination of bevacizumab and weekly Paclitaxel in advanced melanoma. *Oncology* 74, 12-16 (2008).
17. Terheyden, P., Hofmann, M. A., Weininger, M., Brocker, E. B. & Becker, J. C. Anti-vascular endothelial growth factor antibody bevacizumab in conjunction with chemotherapy in metastasising melanoma. *J. Cancer Res. Clin. Oncol.* 133, 897-901 (2007).
18. Ferrara, N. Vascular endothelial growth factor: basic science and clinical progress. *Endocr. Rev.* 25, 581-611 (2004).
19. Shibuya, M. Vascular endothelial growth factor receptor-2: its unique signaling and specific ligand, VEGF-E. *Cancer Sci.* 94, 751-756 (2003).
20. Crawford, S. E. Vascular interference: a blockade to tumor epithelial growth. *Hepatology* 39, 1491-1494 (2004).
21. Ferrara, N. Role of vascular endothelial growth factor in regulation of physiological angiogenesis. *Am. J. Physiol Cell Physiol* 280, C1358-C1366 (2001).
22. Park, J. E., Keller, G. A. & Ferrara, N. The vascular endothelial growth factor (VEGF) isoforms: differential deposition into the subepithelial extracellular matrix and bioactivity of extracellular matrix-bound VEGF. *Mol. Biol. Cell* 4, 1317-1326 (1993).
23. Nagengast, W. B. *et al. In vivo* VEGF imaging with radiolabeled bevacizumab in a human ovarian tumor xenograft. *J. Nucl. Med.* 48, 1313-1319 (2007).
24. Stollman, T. H. *et al.* Specific imaging of VEGF-A expression with radiolabeled anti-VEGF monoclonal antibody. *Int. J. Cancer* 122, 2310-2314 (2008).
25. Chang, S. K., Rizvi, I., Solban, N. & Hasan, T. *In vivo* Optical Molecular Imaging of Vascular Endothelial Growth Factor for Monitoring Cancer Treatment. *Clin. Cancer Res.* 14, 4146-4153 (2008).
26. Stollman, T. H. *et al.*. Tumor accumulation of radiolabeled bevacizumab due to targeting of cell- and matrix-associated VEGF-A isoforms. *Cancer Biother. Radiopharm.* 24, 195-200 (2009).
27. Scheer, M. G. *et al.*. Imaging liver metastases of colorectal cancer patients with radiolabelled bevacizumab: Lack of correlation with VEGF-A expression. *Eur. J. Cancer* (2008).
28. www.nccn.org. 2009. Ref Type: Generic
29. Loening, A. M. & Gambhir, S. S. AMIDE: a free software tool for multimodality medical image analysis. *Mol. Imaging* 2, 131-137 (2003).
30. Jayson, G. C. *et al.*. Molecular imaging and biological evaluation of HuMV833 anti-VEGF antibody: implications for trial design of antiangiogenic antibodies. *J. Natl. Cancer Inst.* 94, 1484-1493 (2002).
31. Collingridge, D. R. *et al.*. The development of [(124)I]iodinated-VG76e: a novel tracer for imaging vascular endothelial growth factor *in vivo* using positron emission tomography. *Cancer Res.* 62, 5912-5919 (2002).
32. Perik, P. J. *et al.* Indium-111-labeled trastuzumab scintigraphy in patients with human epidermal growth factor receptor 2-positive metastatic breast cancer. *J. Clin. Oncol.* 24, 2276-2282 (2006).
33. Jilaveanu, L. *et al.* Expression of sorafenib targets in melanoma patients treated with carboplatin, paclitaxel and sorafenib. *Clin. Cancer Res.* 15, 1076-1085 (2009).
34. Straume, O. & Akslen, L. A. Expresson of vascular endothelial growth factor, its receptors (FLT-1, KDR) and TSP-1 related to microvessel density and patient outcome in vertical growth phase melanomas. *Am. J. Pathol.* 159, 223-235 (2001).

Chapter 6B

Bevacizumab treatment and VEGF imaging in a hereditary hemorrhagic telangiectasia patient

New England Journal of Medicine. 2009;361:931-2.

To the Editor

Bose et al. (May 14 issue)[1] report on a patient with hereditary hemorrhagic telangiectasia (HHT) who was treated with bevacizumab for epistaxis. Our patient was a 55-year-old man with HHT (endoglin mutation P.LYS402.FS) with intractable pain and frequent episodes of pancreatitis related to pancreatic arteriovenous malformations. Surgery and embolization were not feasible. An indium-111–labeled bevacizumab single-photon-emission computed tomographic (CT) scan[2] showed elevated tracer uptake in the arteriovenous malformations. Bevacizumab at a dose of 5.0 mg per kilogram of body weight every 2 weeks was started 1 year ago. This treatment immediately stopped the epistaxis, the skin vascular signs became less pronounced, and the frequency and severity of pancreatitis diminished. After 5 months, the dose was increased to 7.5 mg per kilogram. Thereafter, morphine and tube feeding could be discontinued, and the patient resumed work. No change in the volume of the arteriovenous malformations was observed on CT. The patient still receives bevacizumab.

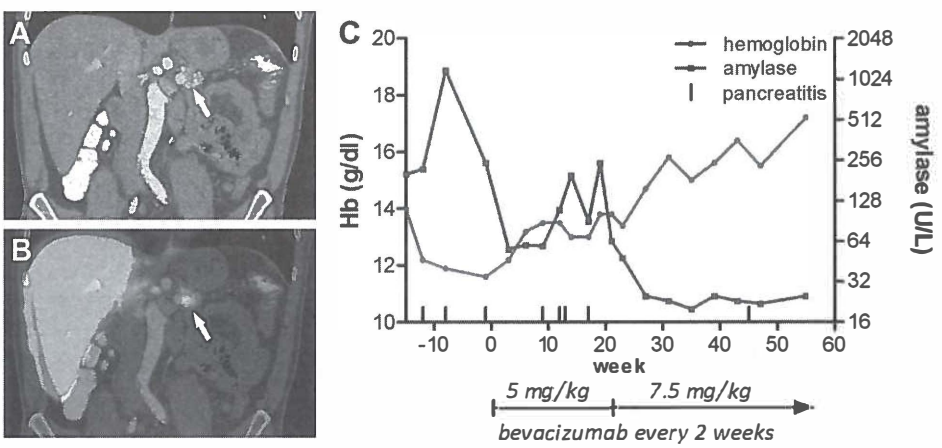

Figure 1. A. Coronal CT image of a patient with hereditary hemorrhagic telangiectasia with arteriovenous malformations (AVMs) in the pancreas (arrow). B. Fused coronal ^{111}In-bevacizumab SPECT/CT image . The SPECT image shows increased ^{111}In-bevacizumab uptake in an AVM (arrow) indicating increased local VEGF concentration. C. Changes in hemoglobin and serum amylase and pancreatitis episodes before and during treatment with bevacizumab. (see page 156 for color figure)

References

1. Bose P, Holter JL, Selby GB. Bevacizumab in hereditary hemorrhagic telangiectasia. *New Engl J Med* 2009;360:2143-4.
2. Nagengast WB, de Vries EG, Hospers GA, et al. *In vivo* VEGF imaging with radiolabeled bevacizumab in a human ovarian tumor xenograft. J Nucl Med 2007;48:1313-9.

Chapter 7

VEGF-PET imaging is a non-invasive biomarker showing differential dynamic angiogenic changes during sunitinib treatment

Wouter B. Nagengast[1], Marjolijn N. Lub-de Hooge[2,3], Sjoukje F. Oosting[1], Wilfred F.A. den Dunnen[4], Frank-Jan Warnders[1], Adrienne H. Brouwers[3], Johan R. de Jong[3], P. Price[6], Harry Hollema[4], Geke A.P. Hospers[1], Philip H. Elsinga[3], Jan Willem Hesselink[5], Jourik A. Gietema[1], Elisabeth G.E de Vries[1].

Departments of Medical Oncology[1], Hospital and Clinical Pharmacy[2], Nuclear Medicine and Molecular Imaging[3], Pathology[4], Surgery[5], University of Groningen and University Medical Center Groningen, The Netherlands and Academic Department of Radiation Oncology[6], The Christie Hospital, Manchester, United Kingdom.

Submitted

Abstract

Many questions exist regarding heterogeneity of tumor response, adaptation and resistance to anti-angiogenic drugs like sunitinib. Vascular endothelial growth factor (VEGF), excreted by tumor cells, plays a key role in angiogenesis. Therefore, we investigated the effect of sunitinib treatment and withdrawal on the tumor with ^{18}F-FDG PET,^{15}O-water PET and the new VEGF-PET tracer ^{89}Zr-ranibizumab in human xenograft tumor models. In contrast to ^{18}F-FDG and ^{15}O-water PET, VEGF-PET demonstrated dynamic changes within the tumor with a strong decline in signal in the tumor center and only minimal reduction in tumor rim, with a pronounced rebound after sunitinib discontinuation. VEGF-PET results corresponded with tumor growth, immunohistochemical vascular- and tumor-markers. Therefore, VEGF-PET allows non-invasive follow-up of responding and non-responding tumor areas and opens up new opportunities for whole body monitoring of anti-angiogenic therapies in patients.

Introduction

Angiogenesis, the formation of new blood vessels, is one of the hallmarks of carcinogenesis. Anti-angiogenic drugs, as single agent or combined with chemotherapy have improved disease outcome in several tumor types. However, this benefit is modest and often of limited duration. Vascular endothelial growth factor (VEGF), mainly produced by tumor cells, and its receptors on endothelial cells, are important players in the regulation of angiogenesis and provide targets for anti-angiogenic agents [1]. Currently, many questions exist regarding heterogeneity of tumor response and tumor adaptation and resistance to anti-angiogenic therapies. Drugs blocking the VEGF/VEGF-receptor pathway, such as the clinically used receptor tyrosine kinase inhibitor (TKI) sunitinib can, apart from blocking angiogenesis in the primary tumor, also lead to increased invasiveness at the tumor boundary and promote metastases [2].

This complex and dynamic interaction between tumor cells and their micro-environment may be an important reason why until now, investigated biomarkers failed to predict response to anti-angiogenic therapy. Quests for biomarkers were especially directed at circulating markers and visualizing anatomic tumor changes during anti-angiogenic treatment. This response to anti-angiogenic treatment is presumably dynamic over time and diverse within the tumor. Therefore molecular imaging, visualizing *in vivo* biological processes, might provide a better insight into how a tumor responds to anti-angiogenic treatment. Well known techniques for molecular imaging are measurement of glucose uptake with ^{18}F-FDG positron emission tomography (PET) and perfusion measurements with ^{15}O-water PET. A new option is non-invasive molecular imaging of VEGF-A, which is overexpressed by many cancer types. Larger VEGF-A isoforms ($VEGF_{165, 189, 206}$) remain in the extracellular matrix resulting in high concentrations in the tumor microenvironment [1,3]. These isoforms are therefore rational targets for serial imaging of VEGF-A [4,5]. Previously, we demonstrated VEGF-A driven tumor uptake of the anti-VEGF-A monoclonal antibody bevacizumab labeled with ^{89}Zirconium (^{89}Zr), though maximum uptake took 4-7 days post injection (pi) [5]. To gain a more detailed insight in the dynamic tumor response during anti-angiogenic treatment with shorter intervals, we developed the VEGF-PET tracers ^{18}F- and ^{89}Zr-ranibizumab. Ranibizumab, a Fab fragment with high affinity for all VEGF-A isoforms is used to treat macular degeneration[6]. Radiolabeled ranibizumab allows fast and sequential follow-up scans, as its serum half-life is only 2-6 h compared to 21 days for bevacizumab. We choose ^{18}F and ^{89}Zr as these are both clinically used PET isotopes (half-life respectively 110 min and 78 h), allowing high resolution quantitative PET imaging.

Sunitinib is used in an intermittent dosing schedule for the treatment of metastatic renal cell cancer and imatinib mesylate-resistant gastrointestinal stromal tumor[7]. We investigated the effect of sunitinib treatment and its withdrawal on tumor behavior with ^{18}F-FDG, ^{15}O-water and VEGF-PET in human xenograft tumor models.

VEGF-PET showed a pronounced reduction in uptake in the tumor center, a minimal reduction and transient effects of sunitinib in the rim, with a strong rebound after discontinuation. These results are validated with corresponding histological and immunohistochemical methods. In addition, we show the clinical applicability of VEGF-PET in a patient with metastatic renal cell cancer (RCC).

VEGF-PET proved to be a valid biomarker of dynamic angiogenic changes in tumors during sunitinib treatment and therefore is an ideal tool for non-invasive follow up by means of VEGF monitoring of tumor lesions during anti-angiogenic therapy in patients.

RESULTS

Sunitinib diminishes tumor growth, but rapid regrowth after discontinuation

Sunitinib treatment was evaluated in the human ovarian cancer A2780 and human colon cancer Colo205 model. Both models were chosen for their angiogenic profile and constant growth rate [7,8]. In A2780 bearing mice, tumor growth diminished after 7 days of daily sunitinib treatment from a baseline volume of 100% to 123.7 ± 16.0%, compared to 182.0 ± 18.1% in non-treated animals (Figure 1a). Thereafter the animals were taken off sunitinib for 7 d and tumor growth accelerated to 190 ± 10.8% on d 14. Tumor growth was slower when sunitinib was continued, resulting in a tumor volume of 140.0 ± 16.1% at d 14 compared to d 0 (P=0.067).

In the Colo205 model, sunitinib induced tumor stabilization at d 7 after daily sunitinib treatment. When sunitinib was withdrawn, tumors showed a regrowth from a volume of 86.6 ± 12.9% on d 7 to 132.9 ± 26.8% on d 14 (P = 0.096) (Figure 1b).

Molecular imaging with ^{18}F-FDG PET and ^{15}O-water PET

Effects on glucose uptake following sunitinib were studied in A2780 tumor bearing animals using ^{18}F-FDG. At baseline, ^{18}F-FDG PET showed a homogeneous tumor uptake (Figure 1c). Seven days sunitinib resulted in a 55% homogeneous decrease in ^{18}F-FDG uptake compared to non-treated animals (Figure 1c and d). When sunitinib treatment was stopped, ^{18}F-FDG uptake on d 14 was slightly higher than on d 7.

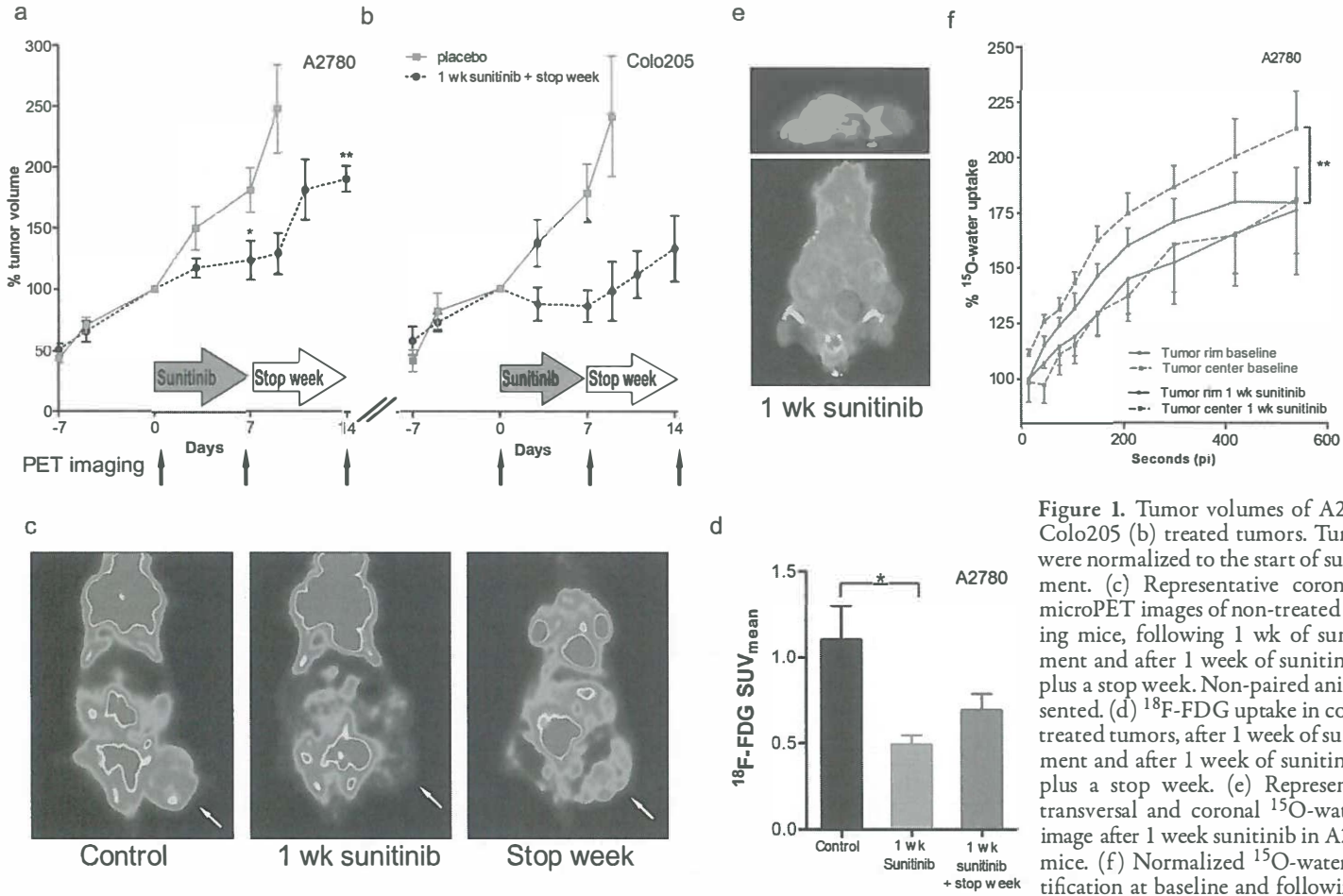

Figure 1. Tumor volumes of A2780 (a) and Colo205 (b) treated tumors. Tumor volumes were normalized to the start of sunitinib treatment. (c) Representative coronal ^{18}F-FDG microPET images of non-treated A2780 bearing mice, following 1 wk of sunitinib treatment and after 1 week of sunitinib treatment plus a stop week. Non-paired animals are presented. (d) ^{18}F-FDG uptake in control A2780 treated tumors, after 1 week of sunitinib treatment and after 1 week of sunitinib treatment plus a stop week. (e) Representative fused transversal and coronal ^{15}O-water PET/CT image after 1 week sunitinib in A2780 bearing mice. (f) Normalized ^{15}O-water PET quantification at baseline and following 1 week of sunitinib. * $P < 0.05$, ** $P < 0.01$. *Data presented as SEM.* (see page 157 for color figure)

^{15}O-water PET in A2780 tumors showed at baseline a 3-8 fold lower tumor ^{15}O-water uptake than well perfused organs such as heart and kidneys resulting in suboptimal tumor visualization (Figure 1e). At baseline, ^{15}O-water PET tumor uptake was 15.8% higher in the center compared to the tumor rim (Figure 1f). At d 7 of sunitinib, tumor uptake tended to decrease in the center compared to baseline (-16.8 ± 7.7% (P = 0.11)). No difference between tumor rim and center was observed.

Similar bioluminescence signal following sunitinib treatment and placebo treatment

To assess non-invasively vitality of tumor cells, bioluminescence experiments were conducted using A2780^{luc+} tumor cells. No difference in bioluminescence signal was observed after 7 and 14 d sunitinib compared to non-treated tumors, indicating vitality of most tumor cells (data not shown).

Molecular tumor imaging using ^{18}F and ^{89}Zr-ranibizumab PET

First we evaluated characteristics of newly developed ^{89}Zr- and ^{18}F-ranibizumab as specific VEGF tracers in the SKOV-3 model, previously used for radiolabeled bevacizumab imaging[5]. Within 3 h pi of ^{89}Zr-ranibizumab clear tumor visualization was seen (Figure 2a), with a plateau at 24 h pi (Figure 2a and c). At 24 h ^{89}Zr-ranibizumab tumor uptake was 2.54 fold higher than ^{89}Zr-Fab-IgG (3.96 ± 1.00 %ID/g versus 1.56 ± 0.38 %ID/g, P=0.034), signifying VEGF-A specificity of ^{89}Zr-ranibizumab uptake. ^{18}F-ranibizumab uptake was also significantly higher compared to ^{18}F-Fab-IgG (P=0.013) (supplement 3 and 4), though absolute uptake was 2.9 fold lower compared to ^{89}Zr-ranibizumab uptake (P=0.027).

^{89}Zr-ranibizumab tumor uptake could be blocked by increasing doses of unlabeled ranibizumab, till the uptake level of ^{89}Zr-Fab-IgG (Figure 2b). Furthermore, organ biodistribution revealed rapid blood clearance of ^{89}Zr-ranibizumab from 8.44 ± 2.19 %ID/g 1 h pi to 0.38 ± 0.38 %ID/g 24 h pi resulting in tumor/blood ratios of even > 10 (supplement 2). For these reasons, ^{89}Zr-ranibizumab was selected as optimal VEGF-tracer for the follow up of sunitinib treatment.

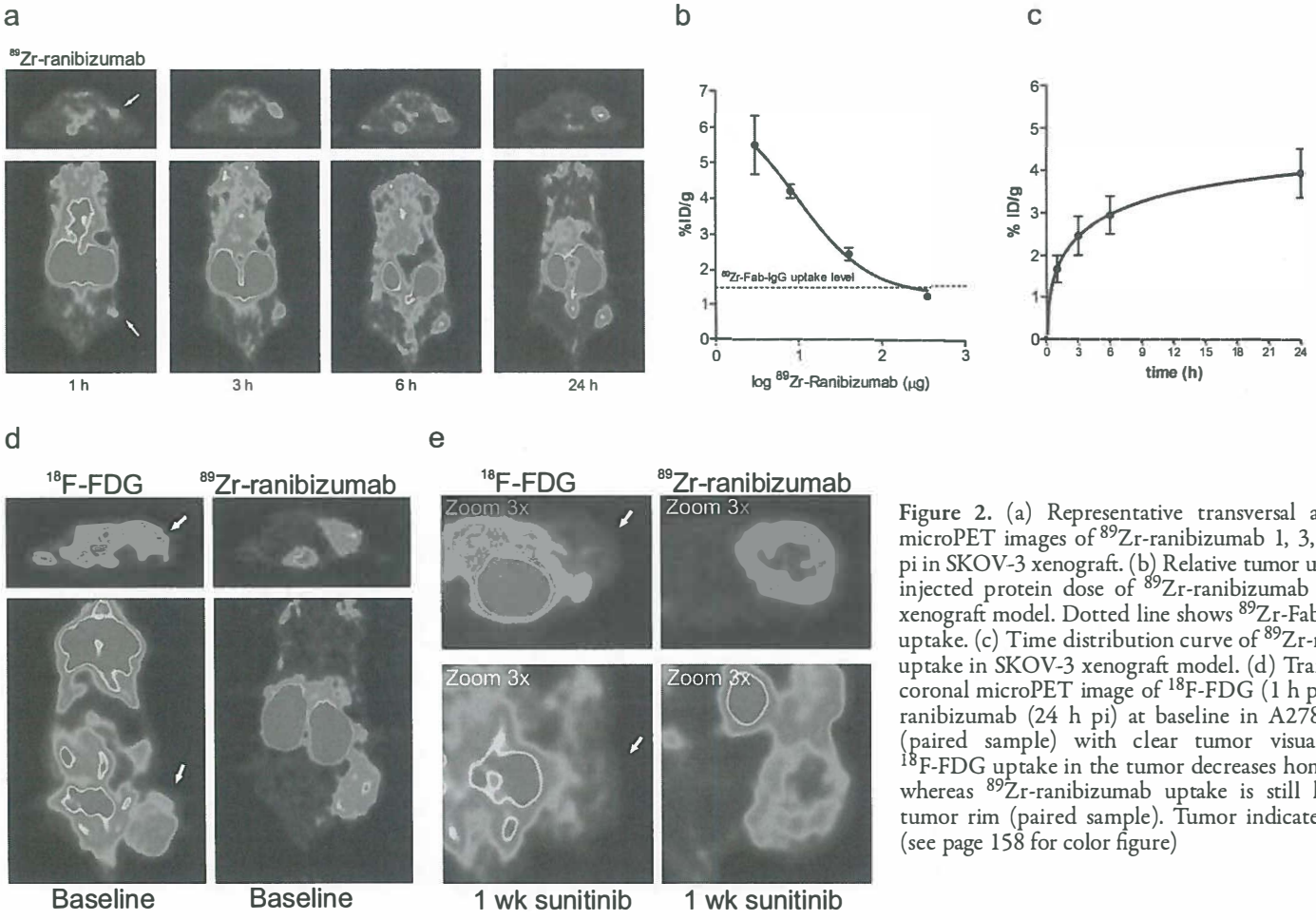

Figure 2. (a) Representative transversal and coronal microPET images of ^{89}Zr-ranibizumab 1, 3, 6 and 24 h pi in SKOV-3 xenograft. (b) Relative tumor uptake versus injected protein dose of ^{89}Zr-ranibizumab in SKOV-3 xenograft model. Dotted line shows ^{89}Zr-Fab-IgG tumor uptake. (c) Time distribution curve of ^{89}Zr-ranibizumab uptake in SKOV-3 xenograft model. (d) Transversal and coronal microPET image of ^{18}F-FDG (1 h pi) and ^{89}Zr-ranibizumab (24 h pi) at baseline in A2780 xenograft (paired sample) with clear tumor visualization (e) ^{18}F-FDG uptake in the tumor decreases homogeneously whereas ^{89}Zr-ranibizumab uptake is still high in the tumor rim (paired sample). Tumor indicated by arrow. (see page 158 for color figure)

Sunitinib decreases ^{89}Zr-ranibizumab tumor uptake especially in the tumor center with a rebound after discontinuation

In the next experiments ^{89}Zr-ranibizumab quantification was performed 24 pi unless otherwise stated. At baseline, ^{89}Zr-ranibizumab uptake was slightly lower (8.75%, P=0.055) in the tumor rim than in the center, comparable to findings seen with ^{15}O-water PET. In A2780 placebo treated mice, ^{89}Zr-ranibizumab (%ID/g) tumor uptake remained constant between baseline and 1 week (Δ 8%, P=0.229). However after 7 d of sunitinib in both A2780 and Colo205 a pronounced reduction of ^{89}Zr-ranibizumab tumor uptake occurred in the center with minimal reduction in the tumor rim, whereas ^{18}F-FDG decreased homogeneously (Figure 2d and e). In the A2780 tumor, ^{89}Zr-ranibizumab uptake decreased only 19.5 ± 5.1% in the rim whereas a vast decrease of 45.4 ± 5.9% was found in the center versus baseline (Figure 3d). In addition, control experiment with ^{89}Zr-Fab-IgG, which reflects non specific extravasation and clearance of Fab fragments, showed only a minimal decrease in uptake at d 7 following sunitinib treatment in A2780, indicating just small changes in non-specific uptake of Fab fragments following sunitinib treatment. However alterations in ^{89}Zr-ranibizumab were 3.2 fold higher than in control ^{89}Zr-Fab-IgG experiments, (Figure 3f) signifying VEGF specific tumor uptake of ^{89}Zr-ranibizumab. Interestingly, in A2780 tumors treated for 14 d, ^{89}Zr-ranibizumab uptake in the rim increased 46% at d 14 versus d 7 (Figure 3e), while in the center the uptake remained low compared to baseline. These results indicate dynamic adaptation of local VEGF levels during sunitinib treatment.

VEGF-PET scans made 7 days after stopping sunitinib showed higher ^{89}Zr-ranibizumab tumor uptake in both models, which exceeded baseline values. In A2780, ^{89}Zr-ranibizumab tumor rim uptake increased 69.5 ± 18.3% versus 7 d sunitinib, and 34.6 ± 11.4% (P=0.056) versus baseline (Fig. 4d). Likewise, uptake in the center increased and returned to baseline. Comparable results were obtained in Colo205 tumors, where ^{89}Zr-ranibizumab uptake in the center also exceeded baseline values (31.7 ± 9.9%, P=0.033) 7 d after discontinuation (supplement 5 and 6). Control experiments using ^{89}Zr-Fab-IgG showed some enhancement in passive tumor uptake, but 2.83 fold lower than with ^{89}Zr-ranibizumab, again indicating VEGF-A driven specificity of ^{89}Zr-ranibizumab uptake (Figure 3f).

Differential tumor response on VEGF-PET scan between rim and center corresponds with microscopic changes

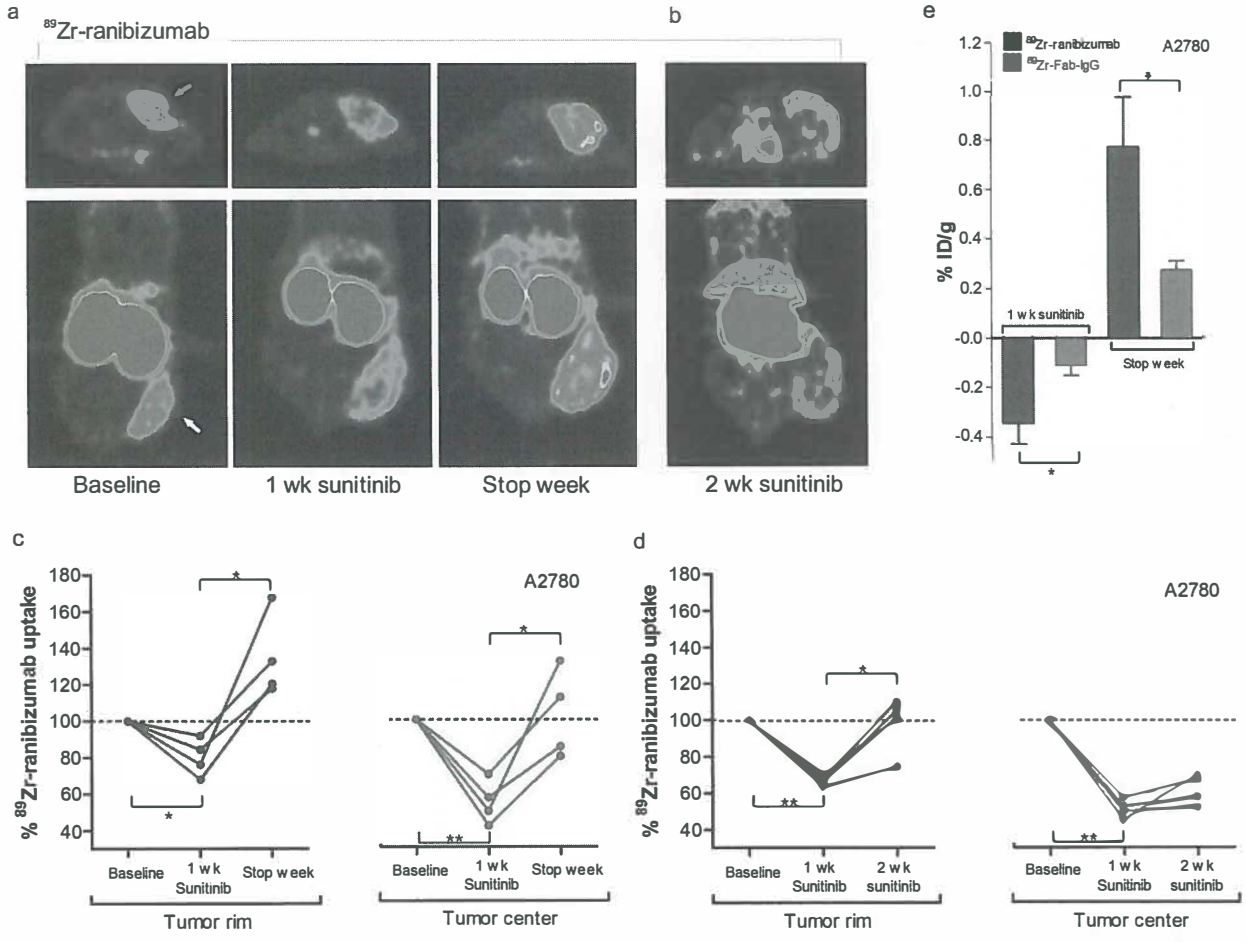

Figure 3. Transversal and coronal microPET images of ^{89}Zr-ranibizumab at 24 h post injection of the tracer (a) High tumor to background ratios clearly visualize a more pronounced reduction in the tumor center compared with the tumor rim after 7 d of sunitinib treatment. After 7 d of discontinuation, ^{89}Zr-ranibizumab uptake increases (paired samples). (b) At d 14 of sunitinib treatment, ^{89}Zr-ranibizumab uptake returns to baseline in the tumor rim while remaining low in the tumor center. ^{89}Zr-ranibizumab quantification of tumor rim and center of mice treated with sunitinib for 1 week at d 7 and following a stop week (c) and after 14 days of sunitinib treatment (d). Individual tumor uptake values are normalized relative to baseline. (e) Change in average tumor uptake (both rim and center) of ^{89}Zr-ranibizumab and ^{89}Zr-Fab-IgG after 7 d of sunitinib and after a stop week in A2780 xenograft model. * $P < 0.05$, ** $P < 0.01$. *Data presented as SEM.* (see page 159 for color figure)

Histological examination also revealed a differential effect of sunitinib on the tumor rim and center. After 7 d sunitinib non-affected blood vessels were present in the tumor rim mainly. Tumor tissue surrounding these vessels retained a high proliferation rate, and low HIF1α and GLUT-1 expression (Figure 4a). Tumor tissue surrounding affected vessels in the center had a low tumor proliferation rate, high HIF1α and GLUT-1 expression. The tumor center contained predominantly vital areas with some areas of necrosis, which is in concordance with the bioluminescence imaging results (supplement 7). Seven days of sunitinib resulted in a reduction of all vascular markers and decreased tumor cell proliferation, which was most pronounced in the center, resembling VEGF-PET findings (table supplement 8). Interestingly, at d 14 the vessel diameter returned to baseline and increased tumor proliferation rate was observed in the tumor rim, which coincided with increased VEGF-A staining and increase in VEGF-PET signal. Interestingly, no changes in vascular markers or, tumor and endothelial proliferation were observed (table 1) in the tumor center compared to d 7, in concordance to the VEGF-PET signal.

Tumor Rim	d 7 versus baseline	d 14 versus d 7	Stop week versus d 7
MVD	↓	≠	↑
Vessel diameter	↓	↑	↑
VEGFR2 expression	↓	≠	↑
Ki67 vessel proliferation (%)	↓	≠	↑
Ki67 tumor proliferation (%)	↓	↑	↑
VEGF-A staining	↓	↑	↑
VEGF PET (%)	↓	↑	↑

Tumor Center	d 7 versus baseline	d 14 versus d 7	Stop week versus d 7
MVD	↓	↓	↑
Vessel diameter	↓	↓	↑
VEGFR2 expression	↓	≠	↑
Ki67 vessel proliferation (%)	↓	≠	↑
Ki67 tumor proliferation (%)	↓	≠	↑
VEGF-A staining	↓	≠	↑
VEGF PET (%)	↓	≠	↑

Other	d 7 versus baseline	d 14 versus d 7	Stop week versus d 7
Necrosis (%)	↑	≠	↓
Stromal vessel diameter	≠	≠	≠
HIF1α	↑	≠	↓
Glut-1	↑	≠	↓
Tumor growth	≠	≠	↑
Plasma human VEGF	↓	↑	↑

↓decrease, $P < 0.05$, ↑increase $P < 0.05$, ≠ unchanged, $P > 0.05$

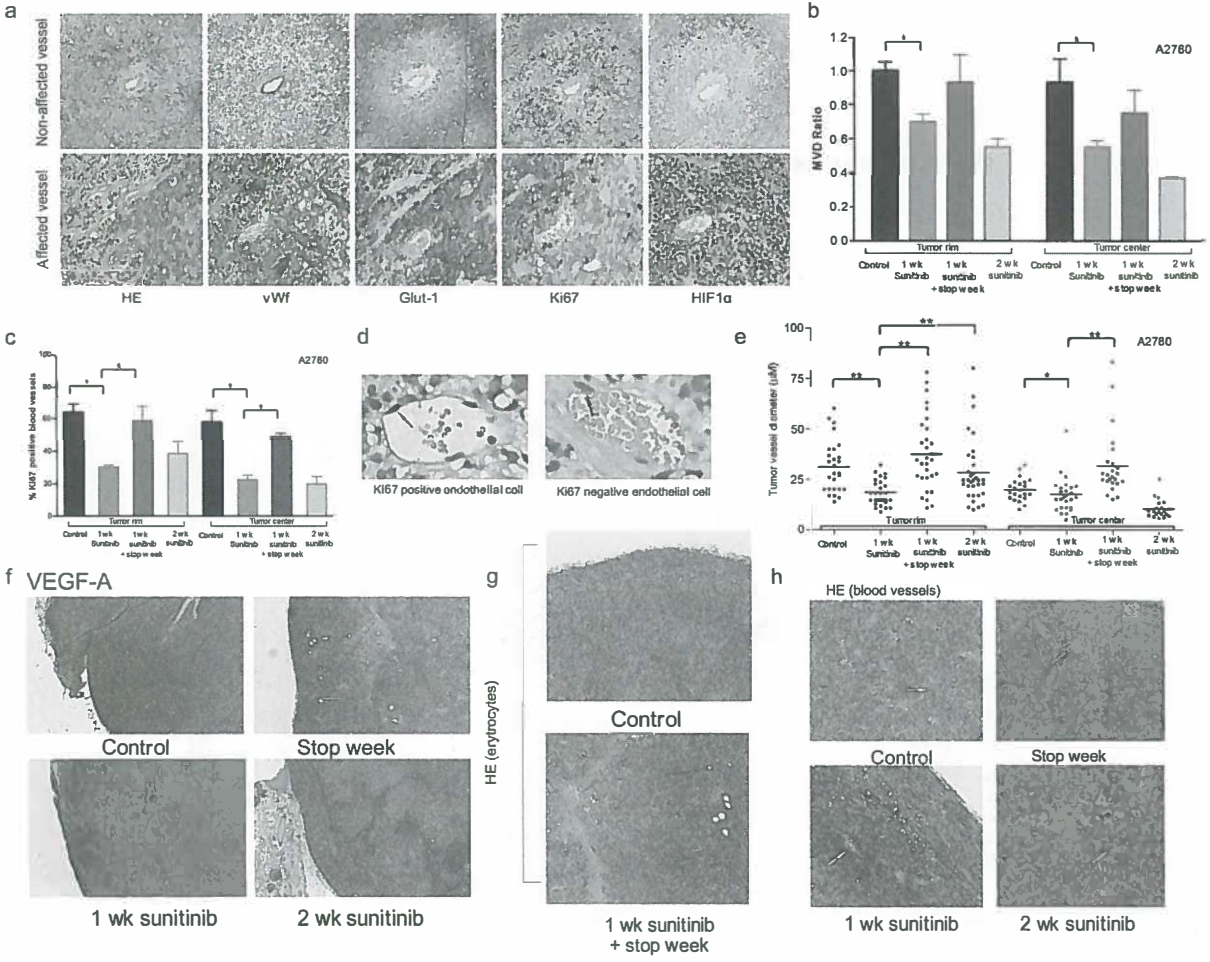

Figure 4. (a) Representative examples A2780 of affected and non-affected tumor vessels following 7 d of sunitinib treatment. Non-affected vessels demonstrates clear vWf staining with low Glut-1 expression, high Ki67 staining and low HIF1α expression in the surrounding tumor tissue which is the opposite for affected tumor vessels. (b) MVD quantification of the tumor rim and center. (c) Percentage of tumor vessels containing Ki67 positive endothelial cells in tumor rim and center. (d) Example of Ki67 positive and negative endothelial cell. (e) Tumor vessel diameter of tumor rim and center. (f) Representative VEGF-A staining. (g) Example of pelioses, randomly distributed red blood cells throughout the tumor at baseline and after stopping sunitinib. (h) Representative examples of blood vessel distribution in the tumor. * $P < 0.05$, ** $P < 0.01$. *Data presented as SEM.* (see page 160 for color figure)

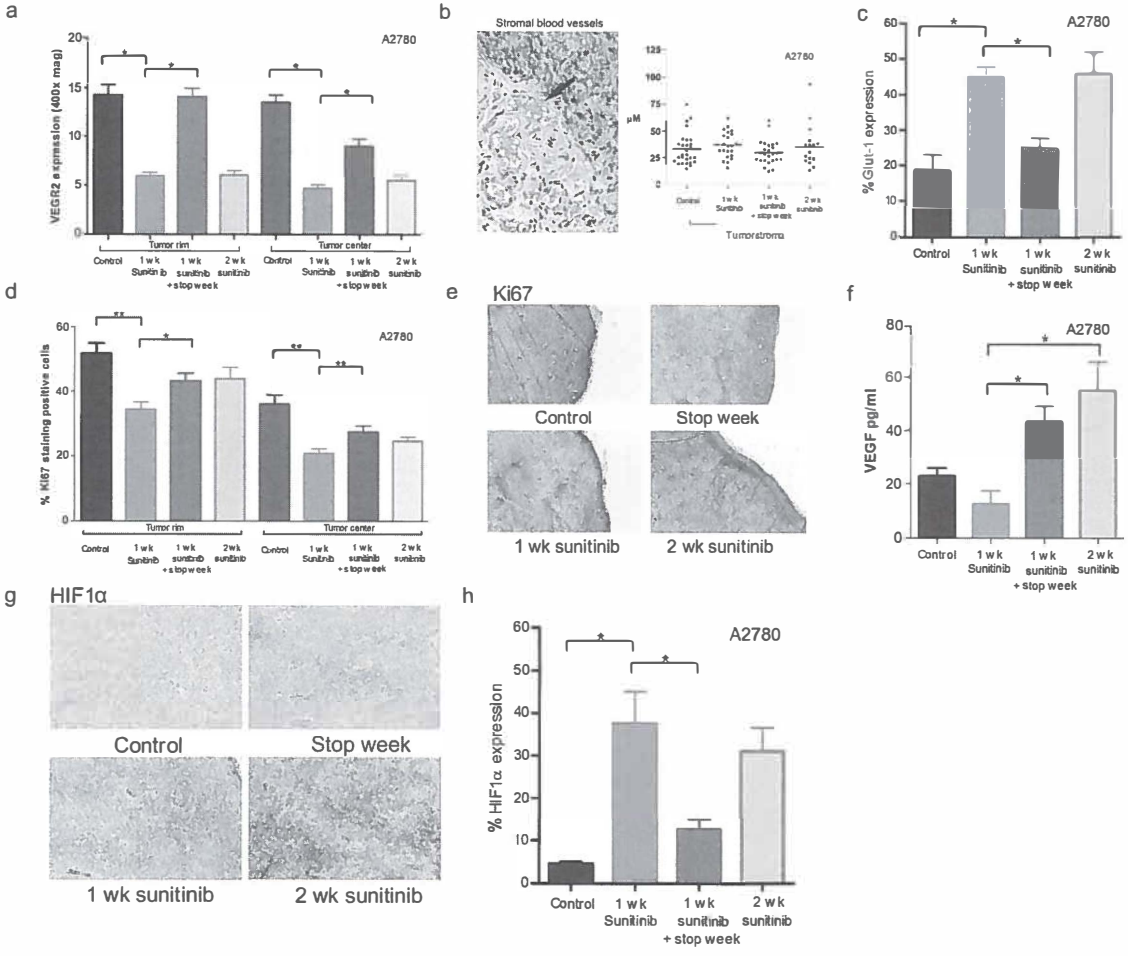

Figure 5. (a) VEGFR2 staining in the tumor rim and center. (b) Peritumoral stromal blood vessels adjacent to the tumor rim and stromal blood vessel diameter. (c) Whole tumor Glut-1 expression. (d) Tumor proliferation rate at the tumor rim and center. After 7 d of sunitinib overall tumor proliferation decreases, though it remains high at the rim. (e) representative examples of Ki67 staining. (f) Human VEGF plasma levels of sacrificed A2780 bearing animals. (g) Representative examples of HIF1α expression. (h) Tumor HIF1α expression. * $P < 0.05$, ** $P < 0.01$. *Data presented as SEM.* (see page 161 for color figure)

After a 7 d drug-free period, all vascular makers recovered and the tumor vessel diameter even exceeded baseline. In addition, HIF1α and Glut-1 expression decreased while an increased VEGF-A expression and tumor proliferation was observed (Figure 4 and 5). Furthermore, large areas of so-called pelioses, randomly distributed multiple blood-filled areas were present at baseline and after discontinuation in parallel with high endothelial proliferation (Figure 4g). All together, these findings indicate rapid tumor revascularization after stopping sunitinib which closely matches *in vivo* VEGF-PET findings.

Changes in tumor derived human plasma VEGF levels

After 7 d sunitinib, tumor derived human VEGF plasma levels decreased by 60% (Figure 5f), while after 14 d sunitinib there was a 6.61 fold increase compared to d 7 following sunitinib treatment. After 7 d drug-free period a 4.79 fold increase was observed.

Clinical VEGF-PET imaging

VEGF-PET imaging showed clear visualization of known lung, skeletal and brain lesions in a patient with metastatic RCC (Figure 6).

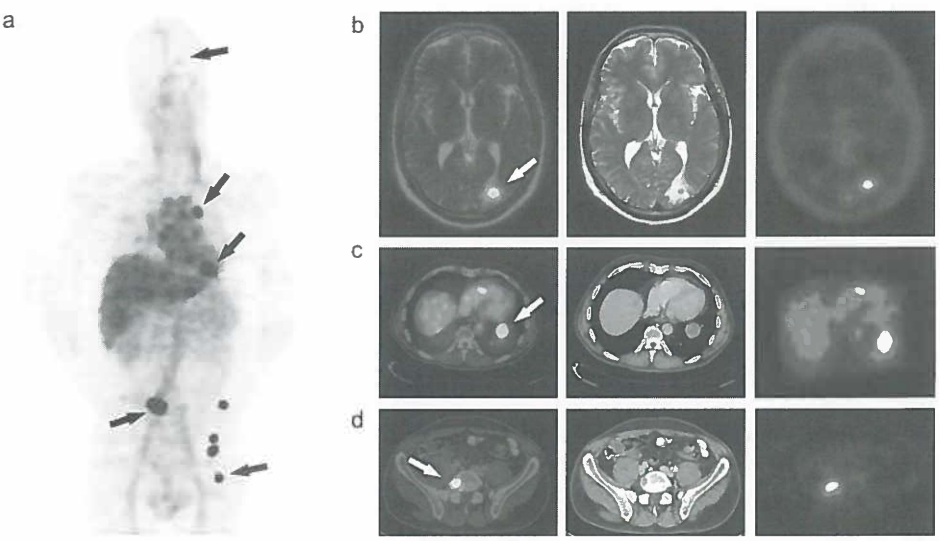

Figure 6. (a) Representative clinical VEGF-PET whole body image 4 days post injection of 37 mBq ^{89}Zr-bevacizumab in a metastatic RCC patient. PET/CT image, CT and PET images of brain (b), lung (c) and vertebral (d) metastatic lesions. Tumors indicated by arrow. (see page 162 for color figure)

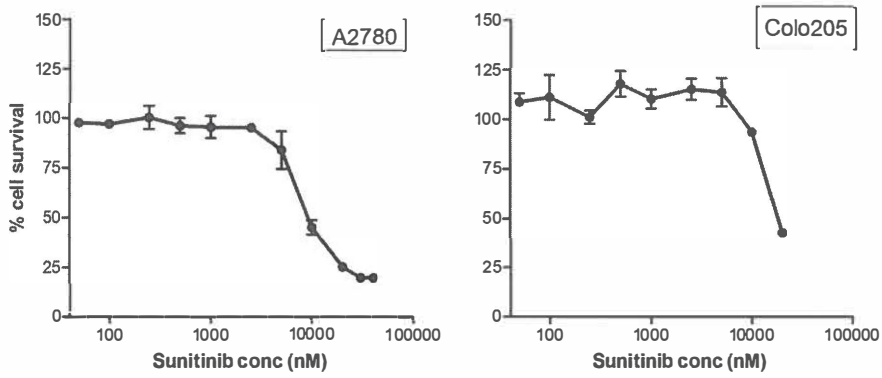

Supplement 1. MTT survival assay of A2780 and Colo205 tumor cells after 4 days of sunitinib incubation. In vitro no cytotoxicity occurred at sunitinib levels (0-5,000 nM) which are relevant plasma levels in mice. *Data presented as SEM.*

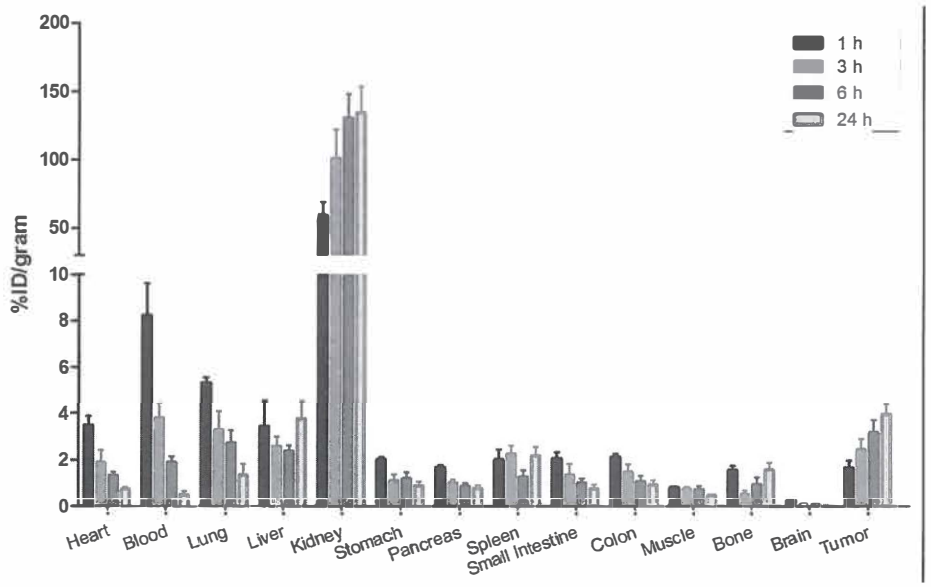

Supplement 2. *Ex vivo* biodistribution of ^{89}Zr-ranibizumab at 1, 3, 6 and 24 h post injection in SKOV-3 xenograft model. *Data presented as SEM.*

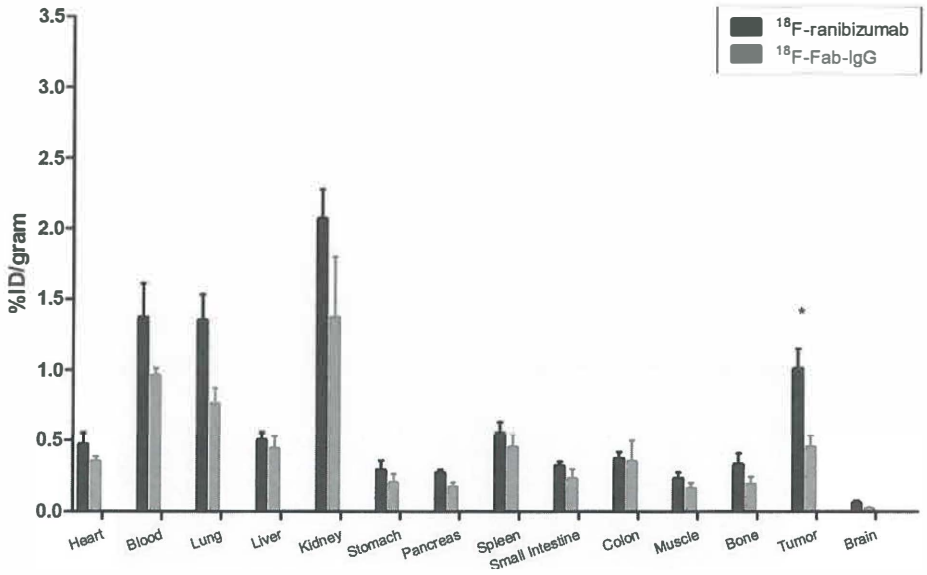

Supplement 3. *Ex vivo* biodistribution of ^{18}F-ranibizumab and control ^{18}F-Fab-IgG 6 h post injection in SKOV-3 xenograft model. * $P < 0.05$. *Data presented as SEM.*

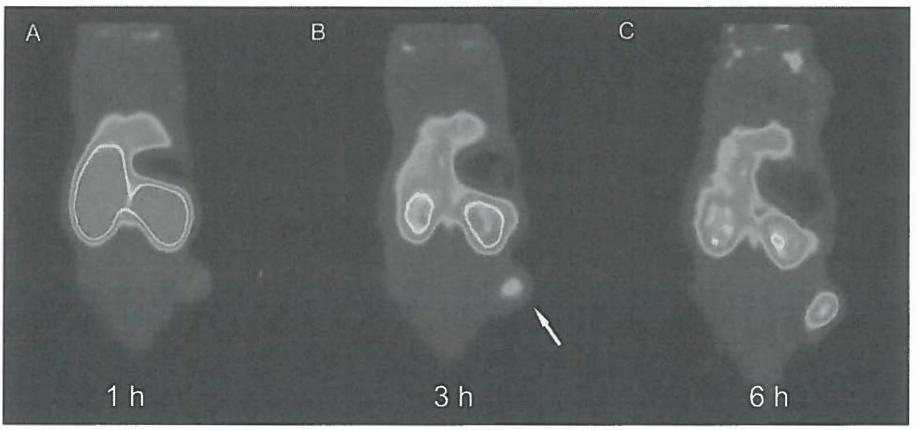

Supplement 4. Coronal microPET images of ^{18}F-ranibizumab 1, 3 and 6 h post injection. In time, ^{18}F-ranibizumab accumulates in the tumor whereas uptake in well perfused organs decreases. Tumor indicated by arrow. (see page 162 for color figure)

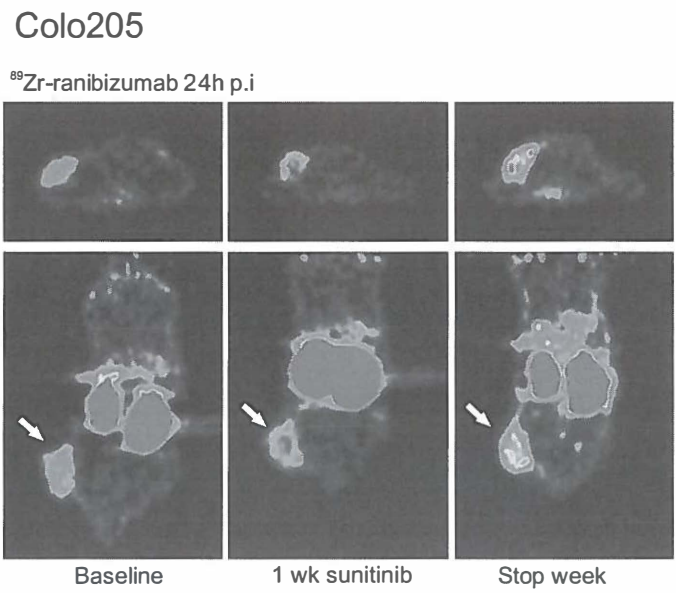

Supplement 5. Transversal and coronal microPET images of ^{89}Zr-ranibizumab at baseline, following 1 week of sunitinib treatment and after 1 stop week. After 1 week of sunitinib treatment ^{89}Zr-ranibizumab uptake decreases, mainly in the center of the tumor. After 1 week of discontinuation, ^{89}Zr-ranibizumab uptake increases. (see page 163 for color figure)

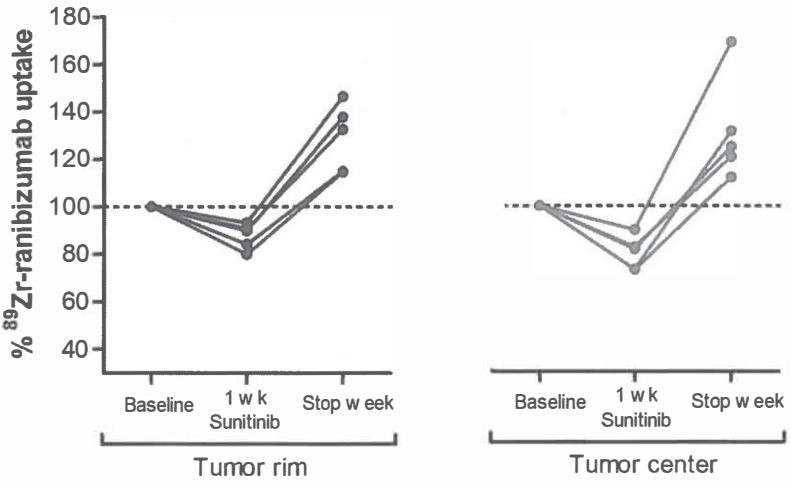

Supplement 6. ^{89}Zr-ranibizumab quantification of tumor rim and center of Colo205 mice treated with sunitinib for 1 week at d 7 and following a stop week. (see page 163 for color figure)

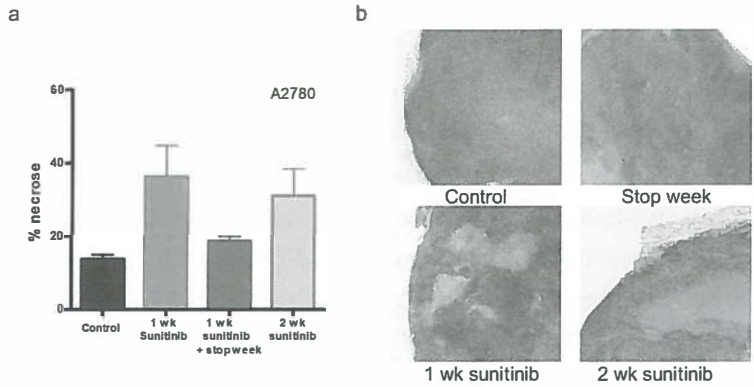

Supplement 7. (A) percentage necrosis of A2780 tumors at baseline, following 1 week of sunitinib treatment, after 1 stop week and after 2 weeks of sunitinib treatment. Individual tumor uptake values are normalized relative to baseline. (B) Representative HE staining at baseline, following 1 week of sunitinib treatment, after 1 stop week and after 2 weeks of sunitinib treatment. (see page 164 for color figure)

Discussion

We investigated the effect of sunitinib treatment and its withdrawal on tumor behavior with ^{18}F-FDG, ^{15}O-water and ^{89}Zr-ranibizumab VEGF-PET in human xenograft tumor models to select the molecular imaging technique which would best reflect intratumoral VEGF changes and/or angiogenesis during sunitinib and after discontinuation. ^{89}Zr-ranibizumab VEGF-PET and not ^{18}F-FDG or ^{15}O-water PET corresponded with findings observed by tumor histology and immunohistochemistry. Strikingly, VEGF-PET demonstrated that sunitinib treatment caused a clear decline in the tumor center with only minimal reduction of VEGF levels in the the tumor rim, and a pronounced rebound after discontinuation. These VEGF-PET imaging findings coincided with tumor growth, tumor cell proliferation and microscopically determined tumor vascularization.

We analyzed in detail and validated the effect of sunitinib and its withdrawal on plasma VEGF, bioluminescence and immunohistochemical tumor analyses and focused on the striking difference between tumor rim and center as illuminated by VEGF-PET. In concordance with reduced tumor growth, sunitinib treatment resulted in a decrease of angiogenic markers like mean vessel density (MVD), as seen in other tumor models [7], vessel diameter and VEGFR2 expression. In addition, true inhibition of angiogenesis is

underscored by reduced endothelial proliferation and the absence of pelioses. We showed that the inhibition of angiogenesis coincided with hypoxia, cellular stress and reduced tumor cell proliferation as indicated by a high HIF1α and Glut-1 expression by tumor cells and negative Ki67 staining. All these effects were more pronounced in the tumor center than in the rim. Interestingly, VEGF-A staining was also less intense in the tumor center, although we had expected an increase as a result of hypoxia caused by VEGF receptor inhibition. When we analyzed the plasma level of tumor derived human VEGF in these mice, we observed an initial decrease after 7 days sunitinib, which matches the results assessed with VEGF-PET and underlines the striking finding of initial drop in VEGF expression by tumor cells during sunitinib treatment that has not been reported before. A potential explanation for the initial decrease of VEGF is an off target effect of sunitinib. Apart from blocking VEGFR signaling, sunitinib binds over seventy other kinases [9]. For instance, recent studies have shown that sunitinib inhibits STAT3 activity, an activator of VEGF transcription, which could explain the initial VEGF reduction [10,11]. In contrast to our findings, Ebos et al. measured already elevated human plasma VEGF levels after 1 week sunitinib in a PC-3 xenograft model [12]. However, after 2 weeks of sunitinib we observed an enhancement in VEGF-PET signal in the tumor rim, which corresponded microscopically with more intense VEGF-A staining, a raise in blood vessel diameter, tumor cell proliferation and raise in plasma VEGF levels. These results suggest transient anti-tumor effects as well as dynamic changes in the VEGF pathway resulting in tumor adaptation to sunitinib treatment. These data are in concordance with vessel normalization already 8 days following initiation of the pan-VEGFR TKI cediranib in a glioblastoma model [13]An explanation for the differences observed between the tumor rim and center might be that tumor cells located at the tumor rim are likely not only dependent on tumor blood vessels, but also benefit from adjacent peritumoral blood vessels. Indeed, we did not observe changes in peritumoral blood vessels during sunitinib. This is in contrast with findings of Kamoun et al. who observed even a large increase in peritumoral blood vessel diameter following cediranib in their glioblastoma model [13]. All together, our findings emphasize that differences exist in response to anti-angiogenic therapy among tumor areas. The interest for biological processes occurring at the edge of the tumor is also attracted by the phenomenon of epithelial mesenchymal transition (EMT) in tumors. EMT contributes to tumor progression and enhances the metastatic potential of tumor cells. It has been proposed that induction of hypoxia is one of the instigators [2,15,16]. Indeed, sunitinib has showed to increase invasiveness at the tumor boundary and enhanced the forming of metastases [2]. VEGF-PET enables non-invasive follow up of this process in the primary tumor as well as in all metastatic lesions.

Previously, pre-clinical immunohistochemical analyses have demonstrated rapid revascularization after stopping the VEGFR TKI AG-013736 [17]. In addition, regrowth of lymph node metastases and flare up of clinical symptoms have been reported during the sunitinib free period or rapidly after discontiniation [18,19]. The strong rebound in VEGF-PET signal and tumor regrowth which we observed after sunitinib discontinuation therefore reflects what is seen in the clinic. Changes in VEGF-PET corresponded with microscopic revascularization, but also increased tumor cell proliferation and decreased HIF1α expression in both tumor models. In addition, the VEGF-PET signal 1 week after discontinuation, which even exceeded baseline, suggests increased VEGF expression. In fact, sustained elevated expression of pro-angiogenic factors following initial hypoxia/HIF1α expression induced by anti-angiogenic therapy has been described, even when acute hypoxia is no longer detectable [14].

Currently especially MRI and PET, are used to visualize anti-angiogenic treatment effects [3,20,21]. Promising pre-clinical and clinical results have been reported using MRI, although high variability during follow up of anti-angiogenic treatment hampers the predictive value for individual patients [13,22]. PET imaging can be additive as it has a higher sensitivity at the molecular level compared with MRI and allows whole body imaging, as we showed for VEGF-PET [23,24]. In our study, the clinically most frequently used tracer ^{18}F-FDG did not reflect intratumoral differences or rapid tumor revascularization and regrowth after stopping sunitinib. Furthermore, the homogeneous reduction in ^{18}F-FDG uptake did not correspond with the vitality seen with bioluminescence imaging and histology.

Despite clinical feasibility of ^{15}O-water PET to assess baseline tumor perfusion, no differences between tumor rim and center were observed in the present study with ^{15}O-water after sunitinib [25]. ^{15}O-water PET performance is partly hampered by the fact that tumor perfusion is relative low compared to well perfused organs. For example, in patients two fold lower perfusion rates were found in primary renal cell tumors versus normal kidneys [26].

VEGF-PET is a promising new imaging biomarker for the follow up of anti-angiogenic therapies as it visualizes one of the key players in angiogenesis. Rapid blood clearance of ^{89}Zr-ranibizumab and VEGF driven uptake resulted in high tumor to background ratios which enables rapid tumor follow up. Relatively high kidney uptake of ^{89}Zr-ranibizumab, as seen with other metal labeled proteins, is a consequence of glomerular filtration of the tracer followed by tubular reabsorption and subsequent lysosomal degradation [27,28].

Most likely, ^{89}Zr-ranibizumab binds to all VEGF-A isoforms located on the cell surface and the extra cellular matrix as has been demonstrated for ^{111}In-bevacizumab in $VEGF_{165}$ and $VEGF_{189}$ over expressing melanoma xenografts [29]. Our most important finding

however, is that ^{89}Zr-ranibizumab tumor uptake also reflected angiogenesis within the tumor at different time points during and after sunitinib treatment. Therefore VEGF-PET imaging gives insight in the activity of the VEGF pathway *in vivo* which is of interest both during tumor progression and the formation of metastasis, as well as during anti-angiogenic treatment. The possibility of back translation between pre-clinical and clinical VEGF-PET imaging will further broaden our knowledge.

In conclusion, VEGF-PET allows non-invasive follow-up of dynamic changes in angiogenesis in different tumor areas. This makes VEGF-PET a very useful candidate for preclinical and clinical follow-up and guidance of new treatment strategies, optimal dose finding and exploration of drug combinations to increase benefit of anti-angiogenic therapies.

Methods

Cell lines and *in vitro* experiments

The human ovarian tumor cell line A2780 was kindly provided by Dr. T.C. Hamilton (Fox Chase Cancer Center, Philadelphia, PA), the human ovarian cancer cell line SKOV-3 and the human colon cancer cell line Colo205 were obtained from the ATCC. Development of A2780^{luc+} has been previously described[30]. A2780, A2780^{luc+} and Colo205 were cultured in RPMI 1640 (Invitrogen), supplemented with 10% heat inactivated fetal calf serum (FCS) (Bodinco BV) and 2 mM L-glutamine (Invitrogen) at 37°C in a fully humidified atmosphere containing 5% CO_2. SKOV-3 was cultured in Dulbecco's Modified Eagles Medium (DMEM) with 4.5 g/ml glucose and 10% FCS. Cells were subcultured three times per week.

For *in vitro* experiments sunitinib (LC Laboratories) was dissolved in dimethyl sulfoxide (DMSO) at 40 mg/ml, and stored at -80 °C. The microculture tetrazolium test (MTT) was used to determine cytotoxicity of sunitinib in A2780 and Colo205 cells as described earlier [31]. Cells were seeded (A2780 3,750 cells/well, Colo205 3,000 cells/well) at optimum density to test cell survival after at least 2–3 cell divisions had taken place in the control cells. Cells were seeded in a 96-wells plate in quadruplicate for each sunitinib concentration (0-20,000 nM) and cultured for 4 days. In vitro no cytotoxicity occurred at sunitinib levels (0-5,000 nM) which are relevant plasma levels in mice (supplement 1).

^{18}F-FDG and ^{15}O-water synthesis

^{18}F-FDG was produced according to the method described earlier using the coincidence ^{18}F-FDG synthesis module [32]. Carrier-added [^{15}O]O_2 was produced by irradiation of a mixture of nitrogen and 1% of oxygen gas with 7 MeV deuterons from a Scanditronix MC-17 cyclotron. [^{15}O]O_2 was reacted with hydrogen gas at 400 °C to generate ^{15}O-water. The

^{15}O-water was trapped in a stervial with 2.5 ml of 0.9% NaCl and sterilized by filtration through a 22 micrometer Millex GP filter.

^{18}F labeling of ranibizumab and control Fab-IgG

N-Succinimidyl-4-18F-fluorobenzoate (^{18}F-SFB) was synthesized as described by Cai et al [33]. ^{18}F-SFB was added to 200 μg of ranibizumab in 250 μl sodium phosphate buffer pH 8.5. The mixture was incubated for 30 min at 37°C. Final purification was achieved using a PD-10 size exclusion column (GE Healthcare) with PBS as the mobile phase to separate protein bound and unbound ^{18}F-SFB . Fractions of 10 sec were collected. Primary quality control, before mixing ranibizumab peak fractions, was performed by instant thin layer chromatography (iTLC). ITLC was performed on silica gel strips using 0.15 mol/l citrate buffer (pH 6.0) as the mobile phase. Radioactivity was determined by an iTLC scanner (VCS-101, Veenstra Instruments). ^{18}F labeling resulted in labeling yields of 1-15%. Purification using a PD-10 column achieved a radiochemical purity of >95%. Specific activity was 550 ± 280 Mbq/mg for ^{18}F-ranibizumab. 6 h storage in 37 °C serum displayed no measurable decrease in protein-bound radioactivity and revealed adequate VEGF-A binding, comparable to unlabeled ranibizumab.

Conjugation and ^{89}Zr-labeling of ranibizumab and control Fab-IgG

Conjugation and labeling of ranibizumab (Lucentis®, Novartis) and control Fab-IgG were performed essentially as described for the antibody U36 [5,34]. In short, the chelate desferrioxamine B (Df) (Novartis Pharma) was succinylated (*N*-sucDf), temporarily filled with stable iron [Fe(III)], and coupled to the lysine residues of ranibizumab by means of a tetrafluorophenol-*N*-sucDf ester. Conjugation was performed at room temperature for 30 min at pH 9.5-9.7. After conjugation, the mixture adjusted to pH 4.2-4.4 (0.1 mol/l H_2SO_4) and 50 μl of 25 mg/ml ethylenediaminetetraacetic acid (EDTA)(Calbiochem) was added to remove Fe(III). The solution was incubated 30 min at 35°C, and purified by ultrafiltration, diluted in water for injection (5 mg/ml) and stored at -20°C. Labeling was performed with ^{89}Zr ($T_{1/2}$ 78 h) produced by Cyclotron BV. In brief, the ^{89}Zr-oxalate solution was adjusted pH 3.9-4.2 and mixed for 3 min. With 4-(2-hydroxyethyl)-1-piperazineethanesulfonic acid (HEPES) (Sigma-Aldrich) buffer the solution was adjusted to pH 6.7-6.9. N-sucDf-ranibizumab was added and incubated for 45 min at room temperature. Ranibizumab labeling with ^{89}Zr (specific activity (SA) 1500 MBq/mg) resulted in yields of > 95%. 24 h storage in 37 °C serum displayed no measurable decrease in protein-bound radioactivity and revealed adequate VEGF-A binding, comparable to unlabeled ranibizumab. Control

^{89}Zr-Fab-IgG is a humanized Fab-fragment comparable in size to ranibizumab. ^{89}Zr-Fab-IgG did not show any binding affinity towards VEGF-A. Therefore, ^{89}Zr-Fab-IgG was used as a control to get insight in the non-VEGF driven extravasation of Fab fragments into the tumor micro-environment.

Animal experiments

All animal experiments were performed with isofluran inhalation anesthesia (induction 3%, maintenance 1.5%). Tumor cells for xenografting were harvested by trypsinization and resuspended in culture medium and Matrigel™ (BD Bioscience). *In vivo* imaging and *ex vivo* biodistribution experiments were conducted using male nude HSD athymic mice obtained from Harlan Nederland. At 6-8 weeks of age the mice were injected subcutaneously with 1.0x105 SKOV3, 5x10^6 A2780, 5x10^6 A2780^{luc+} or 5x10^6 Colo205 cells mixed with 0.1 ml Matrigel™. When the tumor measured 6-8 mm in diameter *in vivo* studies were started.

Bioluminescence imaging

Imaging was conducted with the IVIS® Spectrum (Caliper Life Sciences) composed of a cooled charge-coupled device camera connected to a light-tight black chamber. Before *in vivo* imaging, animals were injected intraperitoneally (ip) with D-luciferin (150 mg/kg; Xenogen) reconstituted in sterile PBS. Mice were placed in prone position on a warmed stage (37°C) in the imaging chamber. Mice were imaged 15 min after luciferin administration using the IVIS system to determine total flux (photons/sec) of emitted light as a measure of the relative number of viable tumor cells in the tumor. Data were analyzed using Living Image 3.0 Software (Caliper Life Sciences)

MicroPET imaging and *ex vivo* biodistribution

^{18}F-FDG (5.0 ± 1.0 Mbq) was injected intravenously into the penile vein and images were made 1 h post tracer injection. Animals fasted for 12 h before ^{18}F-FDG administration. ^{15}O-water (78 ± 8.9 Mbq) was injected intravenously into the penile vein followed by 10 min dynamic PET imaging. Subsequent to ^{15}O-water PET imaging microCT images were made using a MicroCAT II (CTI Siemens) for anatomic localization. ^{89}Zr-ranibizumab (3.5 ±1.5 Mbq) and ^{18}F-ranibizumab (8 ± 4 Mbq) were injected intravenously into the penile vein. During a scan sequence images were made 0, 3, 6 and 24 h (only ^{89}Zr-ranizumab) pi of the tracer. Imaging was performed using a MicroPET Focus 220 rodent scanner (CTI Siemens). Static images of 30 min acquisition time were obtained.

After image reconstruction, *in vivo* quantification was performed with AMIDE Medical Image Data Examiner software (version 0.9.1, Stanford University) [35]. To quantify radioactivity within the tumor, 3D volumes of interest (VOIs) were drawn. ^{18}F-FDG is presented as Standardized Uptake Value (SUV), using mean tumor uptake per cm^3 divided by mean body uptake. ^{15}O-water is presented as percentage uptake per cm^3 relative to tumor uptake in the first frame (30 sec) of the scan. For ^{89}Zr-ranibizumab the total injected dose was calculated by decay correction of the total activity present at 0 h after injection in the animal. The data was quantified as %ID/g, assuming a tissue density of 1. Data is presented as the percentage uptake compared to baseline uptake and corrected for tumor volume. After being sacrificed, animal organs and tissues were excised, rinsed for residual blood and weighed. Samples and primed standards were counted for radioactivity in a calibrated well-type LKB-1282-Compu-gamma system (LKB Wallac) and corrected for physical decay. Tissue activity is expressed as percentage of the injected dose per g tissue (%ID/g). Harvested tumors were divided, immediately frozen at -80°C and paraffin embedded for further analysis.

Dose finding study and pharmacokinetics of ^{89}Zr-ranibizumab and ^{18}F-ranibizumab

Previously we evaluated ^{89}Zr-bevacizumab imaging in a SKOV-3 xenograft model [5]. Therefore we firstly used the SKOV-3 model to evaluate ^{89}Zr-ranibizumab characteristics enabling comparison with available ^{89}Zr-bevacizumab data[5]. In 4 groups of animals 4 doses (3, 8 and 40 μg (all n=4) and 350 μg (n=1)) of ^{89}Zr-ranibizumab were administered and the biodistribution of ^{89}Zr-ranibizumab in each group of mice was determined 24 h pi. Subsequently, four groups (n=4) of mice were injected with 5 μg of ^{89}Zr-ranibizumab and 1, 3, 6 and 24 h after injection, a group of mice was sacrificed and *ex vivo* biodistribution was performed. One group of mice (n=4) was injected with 5 μg of ^{89}Zr-Fab-IgG. *Ex vivo* biodistribution was performed 24 h pi.

One group of mice (n=6) was injected with 9 μg ^{18}F-ranibizumab and imaged after 1, 3 and 6 h post injection. *Ex vivo* biodistribution was performed after the last scan. One group of mice (n=5) was injected with 10 μg of ^{89}Zr-Fab-IgG. *Ex vivo* biodistribution was performed 6 h pi.

Sunitinib treatment in A2780 and Colo205 models

Sunitinib malate was dissolved in DMSO at 75 mg/ml. Before administration, sunitinib was diluted in phosphate-saline buffer (PBS; 140 mmol/l NaCl, 9 mmol/l Na_2HPO_4, 1.3 mmol/l NaH_2PO_4; pH = 7.4) and administrated once daily ip at 60 mg/kg (volume

6.5 ml/kg). Placebo treatment consisted of only vehicle. Sixty mg/kg sunitinib daily previously demonstrated anti-tumor efficacy in xenograft bearing mice and changes in tumor derived human VEGF plasma levels with minimal toxicity during long-term therapy[12]. Sunitinib treatment was evaluated in the human ovarian cancer A2780 and human colon cancer Colo205 model. Both models were chosen for their angiogenic profile and constant tumor growth rate [7,8]. Four different treatment schedules with once daily ip treatment were used. ^{18}F-FDG imaging was performed in A2780 bearing animals at baseline (n=4), d 7 (n=4) of sunitinib treatment and following a drug-free week (n=5). Serial ^{15}O-water PET was carried out in A2780 bearing animals (n=5) at baseline and following 7 d sunitinib. Serial ^{89}Zr-ranibizumab imaging (5 ± 1 μg) was performed in A2780 bearing mice treated with sunitinib for 1 week followed by a drug-free week (n=4), sunitinib ip for 2 weeks (n=4), sunitinib for 1 week (n=4) or placebo treatment (n=4) and Colo205 tumor bearing mice with sunitinib for 1 week followed by a drug-free week (n=5) at baseline, d 7 and d 14. To assess relative attribution of non-VEGF driven uptake, serial ^{89}Zr-Fab-IgG imaging was performed in A2780 bearing animals (n=5) at baseline, d 7 of sunitinib and following a drug-free week. Tumor volumes were assessed by external calibration along the longest axis (x-axis) and the axis perpendicular to the longest axis (y-axis). The tumor volume was calculated by the following formula: $(x \cdot y^2)/2$.

All animal experiments were approved by the animal experiments committee of the University of Groningen.

Plasma human VEGF analysis and tumor immunohistochemistry

Plasma VEGF levels of sacrificed A2780 bearing mice were determined with the human VEGF ELISA kit (R&D Systems). Paraffin-embedded tumors were stained with hematoxylin and eosin staining (HE) and antibodies against von Willebrand factor (vWf), Ki67 anti-human and anti-mouse, VEGFR2, GLUT-1, HIF1α (Dako), VEGF-A (Santa Cruz). The MVD and VEGFR2 were scored in 3 areas, defined as hot spot areas with the maximum number of micro vessels, as described earlier [5]. To assess changes in tumor vessel diameter, the shortest diameter of the largest vessels (≥ 5 per slide) were measured using computerized Aperio Image Software (Aperio Technologies Inc). Blood vessel proliferation was determined by calculating the percentage blood vessels with Ki67 positive endothelial cells. The proliferation index of the tumor was calculated by percentage of Ki67 positive cells in at least 4 high power fields (200x). MVD, tumor vessel diameter, VEGFR2, blood vessel proliferation and tumor proliferation were obtained for the tumor rim (area < 500 μm

of tumor margin) and tumor center (area > 500 μm of tumor margin). Glut-1 and HIF1α staining was scored manually as percentage positive of total tumor tissue per slide.

Clinical VEGF-PET imaging

^{89}Zr-bevacizumab was produced under GMP conditions as described previously[5]. 37 Mbq (5 mg) of ^{89}Zr-bevacizumab was administrated intravenously. Images were made 4 days pi of the tracer. Whole body imaging was performed in the three dimensional mode, 10 min per bed position (transmission time 20%) using an ECAT HR+ scanner (Siemens/CTI) for data acquisition. PET images were fused with CT images using AMIDE Medical Image Data Examiner software (version 0.9.1, Stanford University). Patient is recruited in trial NCT00831857 (www.clinicaltrials.gov).

Statistical analysis

Data is presented as means ± standard error of the mean (SEM). Statistical analysis was performed using the Mann-Whitney test for non-parametric data and a paired sampled T-test for paired data (SPSS, version 14). A double side *P* value ≤ 0.05 was considered significant.

Acknowledgements

We would like to thank T.H. Oude Munnink, T. Jones, E.M.E. van Straten for technical assistance and helpful comments on the manuscript.

This study was supported by a personal grant to W.B. Nagengast and grants RUG 2007-3739 and RUG 2009-4273 all of the Dutch Cancer Society.

Author contributions

W.B.N. designed the study, performed the experiments and wrote the manuscript; M.N.H. supervised GMP development of the PET tracers, designed the study and wrote the manuscript, S.O. and G.A.P.H. designed the study and wrote the manuscript, W.F.A.D. assisted and supervised immunohistochemical analyses and wrote the manuscript, F.W. assisted in the animal experiments and edited the manuscript, A.H.B. conducted the clinical VEGF PET imaging and edited the manuscript, J.R.J. assisted with PET quantifications and edited the manuscript, P.P. designed the study and wrote the manuscript, H.H. supported immunohistochemical analyses and edited the manuscript, P.H.E. supervised development of the PET tracers and edited the manuscript, J.W.H. performed the bioluminescence experiments, J.G. designed the study and wrote the manuscript, E.G.E.V. supervised the research, designed the study and wrote the manuscript.

References

1. Ferrara, N., Gerber, H. P. & LeCouter, J. The biology of VEGF and its receptors. *Nat. Med.* 9, 669-676 (2003).
2. Paez-Ribes, M. *et al.* Antiangiogenic therapy elicits malignant progression of tumors to increased local invasion and distant metastasis. *Cancer Cell* 15, 220-231 (2009).
3. Jubb, A. M., Oates, A. J., Holden, S. & Koeppen, H. Predicting benefit from anti-angiogenic agents in malignancy. *Nat. Rev. Cancer* 6, 626-635 (2006).
4. Park, J. E., Keller, G. A. & Ferrara, N. The vascular endothelial growth factor (VEGF) isoforms: differential deposition into the subepithelial extracellular matrix and bioactivity of extracellular matrix-bound VEGF. *Mol. Biol. Cell* 4, 1317-1326 (1993).
5. Nagengast, W. B. *et al. In vivo* VEGF imaging with radiolabeled bevacizumab in a human ovarian tumor xenograft. *J. Nucl. Med.* 48, 1313-1319 (2007).
6. Ferrara, N., Damico, L., Shams, N., Lowman, H. & Kim, R. Development of ranibizumab, an anti-vascular endothelial growth factor antigen binding fragment, as therapy for neovascular age-related macular degeneration. *Retina* 26, 859-870 (2006).
7. Christensen, J. G. A preclinical review of sunitinib, a multitargeted receptor tyrosine kinase inhibitor with anti-angiogenic and anti tumour activities. *Ann. Oncol.* 18 Suppl 10, x3-10 (2007).
8. Keyes, K. A., Mann, L., Teicher, B. & Alvarez, E. Site-dependent angiogenic cytokine production in human tumor xenografts. *Cytokine* 21, 98-104 (2003).
9. Stein, M. N. & Flaherty, K. T. CCR drug updates: sorafenib and sunitinib in renal cell carcinoma. *Clin. Cancer Res.* 13, 3765-3770 (2007).
10. Xin, H. *et al.* Sunitinib inhibition of Stat3 induces renal cell carcinoma tumor cell apoptosis and reduces immunosuppressive cells. *Cancer Res.* 69, 2506-2513 (2009).
11. Xu, Q. *et al.* Targeting Stat3 blocks both HIF-1 and VEGF expression induced by multiple oncogenic growth signaling pathways. *Oncogene* 24, 5552-5560 (2005).
12. Ebos, J. M., Lee, C. R., Christensen, J. G., Mutsaers, A. J. & Kerbel, R. S. Multiple circulating proangiogenic factors induced by sunitinib malate are tumor-independent and correlate with antitumor efficacy. *Proc. Natl. Acad. Sci. U. S. A* 104, 17069-17074 (2007).
13. Kamoun, W. S. *et al.* Edema control by cediranib, a vascular endothelial growth factor receptor-targeted kinase inhibitor, prolongs survival despite persistent brain tumor growth in mice. *J. Clin. Oncol.* (2009).
14. Casanovas, O., Hicklin, D. J., Bergers, G. & Hanahan, D. Drug resistance by evasion of antiangiogenic targeting of VEGF signaling in late-stage pancreatic islet tumors. *Cancer Cell* 8, 299-309 (2005).
15. Pennacchietti, S. *et al.* Hypoxia promotes invasive growth by transcriptional activation of the met protooncogene. *Cancer Cell* 3, 347-361 (2003).
16. Polyak, K. & Weinberg, R. A. Transitions between epithelial and mesenchymal states: acquisition of malignant and stem cell traits. *Nat. Rev. Cancer* 9, 265-273 (2009).
17. Mancuso, M. R. *et al.* Rapid vascular regrowth in tumors after reversal of VEGF inhibition. *J. Clin. Invest* 116, 2610-2621 (2006).
18. Burstein, H. J. *et al.* Phase II study of sunitinib malate, an oral multitargeted tyrosine kinase inhibitor, in patients with metastatic breast cancer previously treated with an anthracycline and a taxane. *J. Clin. Oncol.* 26, 1810-1816 (2008).
19. Desar, I. M. *et al.* The reverse side of the victory: Flare up of symptoms after discontinuation of sunitinib or sorafenib in renal cell cancer patients. A report of three cases. *Acta Oncol.* 1-4 (2009).
20. Cai, W. & Chen, X. Multimodality molecular imaging of tumor angiogenesis. *J. Nucl. Med.* 49 Suppl 2, 113S-128S (2008).
21. Jain, R. K. Lessons from multidisciplinary translational trials on anti-angiogenic therapy of cancer. *Nat. Rev. Cancer* 8, 309-316 (2008).

22. Hahn, O. M. *et al.* Dynamic contrast-enhanced magnetic resonance imaging pharmacodynamic biomarker study of sorafenib in metastatic renal carcinoma. *J. Clin. Oncol.* 26, 4572-4578 (2008).
23. Perini, R. *et al.* Non-invasive assessment of tumor neovasculature: techniques and clinical applications. *Cancer Metastasis Rev.* 27, 615-630 (2008).
24. Frangioni, J. V. New technologies for human cancer imaging. *J. Clin. Oncol.* 26, 4012-4021 (2008).
25. Saleem, A. & Price, P. M. Early tumor drug pharmacokinetics is influenced by tumor perfusion but not plasma drug exposure. *Clin. Cancer Res.* 14, 8184-8190 (2008).
26. Anderson, H. *et al.* Measurement of renal tumour and normal tissue perfusion using positron emission tomography in a phase II clinical trial of razoxane. *Br. J. Cancer* 89, 262-267 (2003).
27. Behr, T. M., Goldenberg, D. M. & Becker, W. Reducing the renal uptake of radiolabeled antibody fragments and peptides for diagnosis and therapy: present status, future prospects and limitations. *Eur. J. Nucl. Med.* 25, 201-212 (1998).
28. Backer, M. V. *et al.* Molecular imaging of VEGF receptors in angiogenic vasculature with single-chain VEGF-based probes. *Nat. Med.* 13, 504-509 (2007).
29. Stollman, T. H. *et al.* Tumor accumulation of radiolabeled bevacizumab due to targeting of cell- and matrix-associated VEGF-A isoforms. *Cancer Biother. Radiopharm.* 24, 195-200 (2009).
30. Duiker, E. W. *et al.* Enhanced antitumor efficacy of a DR5-specific TRAIL variant over recombinant human TRAIL in a bioluminescent ovarian cancer xenograft model. *Clin. Cancer Res.* 15, 2048-2057 (2009).
31. De Vries, E. G. *et al.* Resistance mechanisms in three human small cell lung cancer cell lines established from one patient during clinical follow-up. *Cancer Res.* 49, 4175-4178 (1989).
32. Hamacher, K., Coenen, H. H. & Stocklin, G. Efficient stereospecific synthesis of no-carrier-added 2-[18F]-fluoro-2-deoxy-D-glucose using aminopolyether supported nucleophilic substitution. *J. Nucl. Med.* 27, 235-238 (1986).
33. Cai, W. *et al.* PET imaging of colorectal cancer in xenograft-bearing mice by use of an 18F-labeled T84.66 anti-carcinoembryonic antigen diabody. *J. Nucl. Med.* 48, 304-310 (2007).
34. Verel, I. *et al.* Long-lived positron emitters zirconium-89 and iodine-124 for scouting of therapeutic radioimmunoconjugates with PET. *Cancer Biother. Radiopharm.* 18, 655-661 (2003).
35. Loening, A. M. & Gambhir, S. S. AMIDE: a free software tool for multimodality medical image analysis. *Mol. Imaging* 2, 131-137 (2003).

Chapter 8

Summary

Chemotherapeutic agents are the mainstay in systemic anti-cancer treatment. Therefore patients that die of metastatic disease do so because they do not respond or develop resistance towards these anti-cancer drugs. The occurrence of tumor resistance to several structurally unrelated classes of natural products, including anthracyclines, taxanes and epipodophyllotoxines, is often referred to as multidrug resistance (MDR). MDR can be caused by several mechanisms including increased expression of the ATP-binding cassette transporters (ABC-transporters) and drug efflux pumps like P-glycoprotein (P-gp) and multidrug resistance protein (MRP1). It was initially thought, that overcoming MDR would resolve the problem of intrinsic or acquired resistance for these drugs. This was aimed for by inhibiting drug efflux pumps like P-gp. However, randomized clinical studies in different groups of cancer patients evaluating the effect of P-gp modulators when added to chemotherapeutic drugs, have not shown any benefit in outcome. These and other findings let to the idea that the ceiling was reached with classical chemotherapeutic drugs. The abundance of knowledge from the preclinical research on dysregulated cellular pathways in tumor cells has resulted in new targeted agents. Therefore the use of the so-called new targeted agents, with or without chemotherapy, might be superior to circumvent MDR and enhance anti-tumor effects. Over the last decade numerous new targeted anticancer agents, specific for intra- and extra cellular tumor targets and antigens located in the extracellular matrix or at the blood vessels of tumors have been developed. There is increasing evidence that several of these agents (combined with chemotherapy) can increase antitumor efficacy.

A subgroup of these agents targets the so-called "process of angiogenesis". This process of new blood vessel formation is not only important for normal tissue development, but is also one of the hallmarks in carcinogenesis. Already 30 years ago it was recognized that tumors need blood vessels to allow tumor cells to execute their critical growth by supplying the tumor with nutrients and oxygen, enabling disposal of metabolic waste products and it provides a route for metastatic spreading. An important factor involved in angiogenesis is vascular endothelial growth factor A (hereafter referred as VEGF). It is released by tumor cells and it induces tumor neovascularization. Overexpression of VEGF occurs in many human tumor types which made VEGF a rational target for anti-angiogenic therapy. This has lead to interest in blocking the signaling of VEGF in human tumors. Antibodies binding to VEGF and its receptors, as well as chemical molecules which can block the tyrosine kinase function of VEGF-receptors, and drugs inhibiting cellular tumor signaling pathways affecting angiogenesis have been developed. Although anti-angiogenic treatment, either as single agent or combined with chemotherapy has improved disease outcome for several tumor types, such as renal cell cancer and colorectal cancer, benefit has been modest and

often only transient. Therefore it would be extremely helpful when a predictive marker would exist to select patients upfront. An option to achieve this might be the non-invasive use of molecular imaging.

This thesis aimed to circumvent drug resistance and develop new imaging modalities to evaluate targeted anti-cancer drugs, with a focus on the use of anti-angiogenic agents and the development and evaluation of VEGF PET tracers.

In chapter 2 an overview is presented on imaging modalities which can be used to visualize MDR and it addresses the possibility to image targets in the tumor for the follow up of targeted therapies. To overcome MDR and increase the efficacy of chemotherapy solely blocking drug efflux pumps proved unsuccessful in the clinic. Currently results indicate that an option for circumvention could be the addition of new targeted therapies. At this moment, blockade of specific growth factor receptors, intracellular targets and tyrosine kinase signaling has already increased the efficacy of classic chemotherapy in several cancer types. However, this success is limited as a lot of patients do not benefit of the addition of targeted agents. To select patients or to analyze treatment effects, new tracers and imaging modalities which represent specific changes in cellular tumor targets or antigens located in micro-environment during therapy might be helpful. We describe two examples of new imaging modalities, namely HER2 and VEGF imaging, as both can serve as target for drugs that can increase the effect of MDR drugs. The HER2 receptor is overexpressed in 20-30% of the breast tumors. The HER2 antibody trastuzumab potentiates the antitumor effect of the MDR drugs, the taxanes. As a consequence, trastuzumab reduces taxane resistance. The HER2 tumor expression can vary during the treatment of a patient and can differ across metastatic lesions within a patient. Therefore, there is a need for methods that are able to assess the HER2 status repeatedly, preferable in all lesions and non-invasively. Molecular imaging of the HER2 receptor could serve this need. In addition to this diagnostic purpose, HER2 imaging could also be used as an early predictive marker for the tumor response to HER2 targeted or HER2 degrading therapies. HER2 imaging starts with selecting a suitable HER2 targeted molecule. Currently available HER2 targeted molecules include full length monoclonal antibodies, Fab-fragments, $F(ab')_2$-fragments, diabodies, minibodies, affibodies, scFv-Fc and peptides. (Pre)-Clinically, these tracers have been shown to visualize HER2 overexpressing tumors and are able to follow up HER2 targeted therapies. HER2 imaging could therefore potentially be used to elucidate altered receptor-antibody interaction in trastuzumab resistant tumors.

As described above, VEGF is one of the key factors in angiogenesis. VEGF exists of at least five different isoforms A-E. VEGF-A is one of the most important growth factors

involved in tumor angiogenesis with different splice variants like VEGF 121, 145, 165, 189 and 206. $VEGF_{121}$ is freely soluble, whereas $VEGF_{165}$ is secreted, though a significant fraction remains localized at the extra cellular matrix, such as $VEGF_{189}$ and $VEGF_{206}$. VEGF is a downstream product which transcription is dependent on growth factor receptors like HER2, epidermal growth factor receptor 1, and intracellular proteins like hypoxia inducible factor 1α (HIF1α), mammalian target of rapamycin (mTOR) and HSP90. Therefore, VEGF imaging could serve as a read out modality of these treatments. To date, several radiolabeled anti-VEGF antibodies and Fab-fragments have been used for the development of VEGF imaging: VG76e, HumMV833, bevacizumab and ranibizumab. As shown in this thesis, these imaging tracers are a promising tool in the follow up of anti-angiogenic therapy.

Drug efflux pumps play an important role in the protection of the brain for toxic agents and may be an important reason why chemotherapeutic drugs fail to reach the brain tissue in adequate doses. The blood brain barrier (BBB) is formed by specialized capillary endothelial cells which have several properties, such as strong tight junctions with a high electrical resistance, absence of fenestrations and presence of efflux-pumps such as P-gp and MDR associated protein MRP1. Strategies to pass the BBB include therapies to change the physical properties of the capillary endothelium by hypertonic solutions or by bradykinin analogs. Other strategies are directed to inhibition of the efflux-pump function. At present the concept of efflux pump inhibition is most frequently studied for P-gp. Studies in rodents have shown that P-gp function can be inhibited with cyclosporine A. To circumvent toxic side effects of cyclosporine in patients, other therapies that influence P-gp function or expression should be utilized. In chapter 3 we describe such therapy, namely the effect of irradiation on the function and expression of P-gp. The effect was investigated in healthy rat brains using the radiolabeled P-gp PET substrate [^{11}C]carvedilol. Right hemispheres of rat brains were locally irradiated with single doses of 2 - 25 Gy followed by 10 mg/kg of the P-gp substrate cyclosporine intravenously, or with a single dose of 15 Gy followed by cyclosporine (10, 15 or 20 mg/kg), or with fractionated irradiation (4 x 5 Gy) followed by cyclosporine (10 mg/kg) 5 days later. Irradiation increased [^{11}C]carvedilol uptake dose dependently, to a maximum of 20% above the non-irradiated hemisphere. In addition, Cyclosporine as well increased [^{11}C]carvedilol uptake dose dependently in both hemispheres, but more in the irradiated hemisphere. Fractionated irradiation resulted in a complete loss of P-gp expression 10 days after the start of irradiation which coincided with increased [^{11}C]carvedilol uptake. Since brain irradiation is frequently applied to patients with brain metastases, it can be speculated that irradiation can lead to a temporary window allowing increased delivery to the brain of

chemotherapeutic drugs that are a substrate for P-gp. This could be considered as a tool in the treatment of brain metastases.

In Chapter 4-7 we describe the development and evaluation of new molecular VEGF tracers and their use in the follow up of new targeted therapies. Herein we focused on the development of molecular tracers which are able to non-invasively visualize and monitor the angiogenic state of the tumor. We hypothesized that this could lead to better patient selection and early response prediction of anti-angiogenic therapy. In chapter 4 we describe the development of radiolabeled bevacizumab for *in vivo* VEGF imaging. Bevacizumab, a humanized monoclonal antibody with high affinity for all VEGF-A isoforms was radiolabeled with the long lived isotopes ^{111}In and ^{89}Zr for SPECT and PET imaging. In vitro, stability testing and immunoreactivity demonstrated no alterations in binding affinity towards VEGF-A and optimal stability in serum during 168 h, ensuring adequate properties for *in vivo* imaging experiments. *In vivo*, clear tumor visualization was seen already 72 h post injection of the tracer. Maximal uptake occurred 168 h post injection. Tumor uptake was significantly higher compared to control ^{89}Zr-IgG, signifying VEGF driven uptake. Furthermore, microPET quantification of ^{89}Zr-bevacizumab was comparable to *ex vivo* biodistribution data, enabling non-invasive follow up of ^{89}Zr-bevacizumab. Histologically, ^{89}Zr-bevacizumab was mainly present within tumor blood vessels and its extra cellular matrix. ^{89}Zr-bevacizumab could for these reasons potentially be used for the treatment follow up of anti-angiogenic treatment.

In chapter 5 we used ^{89}Zr-bevacizumab for the early anti-angiogenic evaluation of HSP90 inhibitor NVP-AUY922. HSP90 is a molecular chaperone, involved in maintaining the conformation, stability, cellular localization and activity of several key oncogenic client proteins. HSP90 is constitutively expressed at 2 to 10 fold higher levels in cancer cells and present in active multi-chaperone complexes, conferring relative sensitivity to treatment with HSP90 inhibitors compared to their normal counterparts. There are currently no biomarkers to predict the effect of, or monitor, HSP90 inhibition therapy. One potential way to monitor HSP90 therapy is to prove its effect via changes in client proteins of HSP90. Client proteins of HSP90 include receptors and transcription factors like epidermal growth factor receptor 1 and 2 (EGFR and HER2), insulin-like growth factor type 1 receptor (IGF1-R) and hypoxia inducible factor 1α (HIF1α). However, most of these client proteins can only be measured by collecting tumor biopsies. Molecular imaging is an attractive alternative as it allows repetitive non-invasive follow up of specific targets. We hypothesized that VEGF is a suitable candidate, as it is a downstream product of various HSP90 client proteins. In ovarian cancer xenografts of A2780 and its cisplatin resistant CP70 human subline, ^{89}Zr-

bevacizumab microPET was performed pre- and post NVP-AUY922 treatment and verified with histological response and *ex vivo* tumor VEGF levels. Two weeks of NVP-AUY922 treatment decreased ^{89}Zr-bevacizumab tumor uptake with 44.4% in A2780 xenografts, while tumor uptake was not affected in CP70 xenografts compared to pre-treatment values. The same pattern was observed for A2780 and CP70 tumor VEGF levels, measured with ELISA, and mean vessel density. These findings coincided with reduction in the proliferation rate, assessed by Ki67 staining, in A2780 tumor tissue only. All together, ^{89}Zr-bevacizumab PET imaging results were in line with the anti-angiogenic response and direct anti-tumor effects after NVP-AUY922 treatment, supporting the specificity of ^{89}Zr-bevacizumab PET as a sensitive technique to monitor the anti-angiogenic response of HSP90 inhibition *in vivo*.

In chapter 6 we investigated the feasibility of VEGF-SPECT in stage III/IV melanoma patients. The feasibility of ^{111}In-bevacizumab single photon emission tomography (SPECT) VEGF imaging was compared with ^{18}F-FDG PET, a glucose analogue reflecting glucose uptake and metabolism of the tumor, and CT imaging in lymph node positive stage III and IV melanoma patients eligible for surgery. VEGF-SPECT visualized all known melanoma lymph node lesions (size 1-10 cm) identified by CT and FDG-PET imaging. We observed optimal tumor to background ratios 4 days post injection of ^{111}In-bevacizumab reflecting the relatively slow pharmacokinetics of monoclonal antibodies. Non-specific liver uptake was seen for ^{111}In-bevacizumab, comparable as seen for other radiolabeled antibodies, for example ^{111}In-trastuzumab. Due to the relatively slow clearance of ^{111}In-bevacizumab, extended tumor exposure takes place which results in maximal tumor accumulation whereas non-specific uptake in other organs decreases in time.

A large variation in ^{111}In-bevacizumab tumor uptake was detected between patients, across lesions within patients and within a lesion of a patient. Future studies should elucidate the role of VEGF imaging in the selection of tumors with high VEGF expression and individual dose finding of bevacizumab treatment.

In chapter 6b we describe the effect of long term treatment with bevacizumab in a patient with pancreatic arteriovenous malformations with hereditary hemorrhagic telangiectasia (HHT). A VEGF-SPECT scan showed before initiation of bevacizumab treatment an elevated tracer uptake in the arteriovenous malformations. Bevacizumab treatment immediately stopped the epistaxis, the skin vascular signs became less pronounced, and the frequency and severity of pancreatitis diminished and finally resolved. These results illustrate the potential of VEGF imaging and anti-VEGF treatment in diseases outside oncology.

Currently, many questions exist regarding heterogeneity of tumor response and tumor adaptation and resistance to anti-angiogenic therapies. Drugs blocking the VEGF/VEGF-

receptor pathway such as the clinically used receptor tyrosine kinase inhibitor sunitinib can, apart from anti-angiogenic effects on the primary tumor, also lead to increased invasiveness at the tumor boundary and enhance metastases. This complex and dynamic interaction between tumor cells and their micro-environment may be an important reason why all tested biomarkers until now failed to predict response to anti-angiogenic therapy. Therefore molecular imaging, visualizing *in vivo* biological processes, might well provide a better insight on how a tumor responds to anti-angiogenic treatment. In chapter 7 we investigated in an xenograft bearing mouse model the impact of sunitinib treatment and withdrawal with ^{18}F-FDG, ^{15}O-water PET for glucose metabolism and tumor perfusion measurements respectively and ^{89}Zr-ranibizumab VEGF-PET and compared imaging results with tumor growth, VEGF plasma levels and histological and immunohistochemical findings. In both the A2780 and the Colo205 xenograft model sunitinib inhibited tumor growth compared to non-treated animals. When sunitinib treatment was stopped rapid tumor regrowth occurred. While ^{18}F-FDG showed an homogeneous tumor response with 50% decrease in tracer uptake, ^{15}O-water PET did not clearly show differences in tumor perfusion, mainly due to a low sensitivity given the low tumor perfusion compared to other organs. Surprisingly, ^{89}Zr-ranibizumab VEGF-PET showed a minimal reduction (- 19%) and adaptation to sunitinib in the rim, but a vast decrease (- 45%) in the tumor center with a strong rebound (+ 65%) after discontinuation. To verify which PET technique reflects best angiogenic tumor response on sunitinib we analyzed in depth the effect of sunitinib and withdrawal on the tumor by bioluminescence and immunohistochemistry as well as plasma VEGF. Here we observed several prominent findings. As expected 7 days of sunitinib treatment resulted in a decrease of angiogenic markers like MVD, vessel diameter, VEGFR2 expression though more in the tumor center than the tumor rim. In addition, we observed decreased endothelial proliferation, increased Glut-1 expression and enhanced HIF1α expression. VEGF-A staining was at day 7 less intense in the tumor center than the tumor rim, and resembled the vascular state and coincided with tumor cell proliferation, which remained high at the tumor margin. The striking finding of an initial drop in VEGF expression by the tumor during sunitinib treatment, as detected immunohistochemically and with VEGF-PET, could be explained by the fact that sunitinib bounds apart from VEGFR2 also 73 other kinases, which will result in several, so- called "off target" effects, in addition to VEGFR blockade. Furthermore, we observed that the tumor response changed over time and rapid tumor revascularization occurred when the treatment was stopped, which coincided with VEGF-PET imaging. Therefore, VEGF-PET allows non-invasive follow of responding and non-responding tumor areas. In addition, we showed the feasibility of clinical VEGF-PET in

a metastatic renal cell carcinoma patient, visualizing lung, mediastinal, bone and also brain metastasis, which allows clinical translation of this technique. In this way, it can be used (pre)clinically for the follow up of new treatment strategies and optimal dose finding and drug combinations to increase benefit of anti-angiogenic therapies.

In conclusion, the development of two VEGF tracers has demonstrated the promising possibility to enable tumor detection and the subsequent follow up of anti-angiogenic therapy.

Chapter 9

Future perspectives

In this thesis we have developed two radiolabeled proteins to get insight in the local VEGF status of the tumor. In chapter 5 we demonstrated in xenograft bearing mice that ^{89}Zr-bevacizumab tumor uptake corresponds with tumor VEGF levels. In chapter 7 we elucidated by using VEGF imaging that tumors respond inhomogeneous to the VEGF-receptor tyrosine kinase inhibitor sunitinib. In addition, we observed large differences in ^{111}In-bevacizumab between patients in our melanoma trial, suggesting strong variation in tumor VEGF expression. Moreover, even lesions of around 1 cm in diameter were detected using VEGF-SPECT. In a metastatic renal cell carcinoma patient we visualized lung, skeletal, mediastinal and even brain lesions by VEGF-PET. All together, these results encourage further research to investigate the potential of this VEGF imaging other areas of oncology. In this chapter I will shortly address future exploration in which VEGF imaging could play a interesting role.

Early predictive marker

Although many angiogenic factors measured in the plasma of patients with solid tumors have shown to be prognostic markers, none of these have demonstrated predictive value for response to anti-angiogenic therapy in individual patients. VEGF is an important factor in angiogenesis and a downstream product of several factors. VEGF transcription is regulated by growth factor receptors like epidermal growth factor receptor 1 and 2 (EGFR and HER2), insulin-like growth factor type 1 receptor (IGF1-R1), intracullar pathways like PI3K and mTOR and transcription factors like hypoxia inducible factor 1α (HIF1α). In chapter 5 we demonstrated in the xenograft bearing mice model that the early effect of HSP90 treatment, which inhibits several client proteins involved in VEGF transcription, can be monitored by VEGF imaging. Potentially this scan can be used as an early predictive factor. This means that also other therapies which affect VEGF secretion deserve attention like for example the evaluation of mTOR inhibition on VEGF excretion. In an upcoming clinical phase II trial we will further test the potential of ^{89}Zr-bevacizumab imaging in the evaluation of HSP90 inhibition.

Fluorescent imaging

VEGF plays an important role in the early malignant transformation of breast cancer. Increased vascularization has been observed in all pre-invasive lesions and increased with lesion severity. Due to the fact that one tumor cell produces tens of thousands VEGF molecules, this could be an attractive imaging target for the detection of early breast cancer. Though, in case of screening, in most likely healthy subjects, a technique without radiation burden is preferable. A way to circumvent this is the use, instead of a radioactive label, a fluorescent label for

imaging. Bevacizumab can be labeled with a fluorescent probe, without affecting the binding characteristics of the antibody towards VEGF. After injection, fluorescent-bevacizumab will most likely accumulate in the target area comparable to the radiolabeled bevacizumab due to the fact that the pharmacokinetic and pharmacologic profile are not altered by the labeling. Subsequently, the fluorescent probe can be excitated by an external light beam which will lead to the emission of fluorescent light. Current breast cancer screening is performed by means of mammography. For screening of high risk individuals, magnetic resonance imaging (MRI) technique is increasingly emerging. However, there is still room for improvement. One could envision a potential role for fluorescent bevacizumab for breast cancer screening as VEGF plays an essential role in the malignant formation of breast cancer.

A second area of potential added value of fluorescent bevacizumab could be during surgical resection of a tumor to obtain a better insight in exact tumor margins. New fluorescent intra-operative imaging systems have recently reached the clinic. The second step is the development of specific imaging probes to give exact insight in the margins of tumors. As demonstrated in chapter 7, VEGF is highly expressed at the tumor margin. Therefore, fluorescent bevacizumab and ranibizumab are attractive options to evaluate in this setting.

Thirdly, fluorescent endoscopy could enhance the sensitivity and specificity of early (pre) malignant tumor detection and potentially minimize sampling errors of tumor biopsies. In several diseases, for example Barrett esophagus and familial adenomatous polyposis it is not always elucidated if lesions are benign or undergo a malignant transformation. Recently, fluorescent endoscopes have entered the clinic. To date, most studies have used auto-fluorescence or aspecific imaging probes. Fluorescent anti-VEGF probes could potentially non-invasively support detection of early malignant processes. All together, fluorescent imaging is an exciting imaging modality in which large clinical progress can be expected upcoming years.

Other targets

Carcinogenesis, angiogenesis and the forming of metastasis is an extremely complex process in which a countless number of cell types, receptors, growth factors and cytokines are involved. To get optimal insight in this process and increase our understanding it is necessary to use non-invasive methods. For this reason, expansion of new imaging probes will be necessary. The interaction between tumor cells and their micro-environment, like stromal, endothelial and inflammatory cells have particularly become of high interest. With the development of new imaging probes we will hopefully get a better understanding in this interaction.

Chapter 10

Nederlandse samenvatting

Chemotherapie is de hoeksteen in de systemische anti-kanker behandeling. Om deze reden sterven patiënten met uitgezaaide ziekte omdat ze niet reageren of resistentie ontwikkelen tegenover deze anti-kanker behandeling. Het voorkomen van tumor resistentie tegen verschillende structureel niet gerelateerde natuurlijke producten, zoals anthracyclines taxanes en epipodophyllotoxines, wordt vaak multidrug resistentie (MDR) genoemd. MDR kan worden veroorzaakt door verschillende mechanismen, zoals expressie van de ATP-bindende cassette transporters (ABC transporters) en drugs efflux pompen als P-glycoproteïne (P-gp) en het multidrug resistentie eiwit (MRP1). Aanvankelijk werd gedacht dat het overbruggen van MDR het probleem van intrinsieke of verworven resistentie voor deze geneesmiddelen zou oplossen, bijvoorbeeld door het uitschakelen van drugs efflux pompen als P-gp. Klinische studies in verschillende groepen van kankerpatiënten toonde echter dat toevoeging van P-gp modulatoren aan klassieke chemotherapie geen voordeel in overleving bewerkstelligde. Deze, en andere bevindingen, leidde tot het idee dat het maximum was bereikt met de klassieke chemotherapie. Echter, de schat aan nieuwe kennis, opgedaan bij preklinische onderzoek, van geactiveerde cellulaire routes in tumor cellen, heeft geleid tot de ontwikkeling van nieuwe geneesmiddelen gericht ("targeted") op deze routes. Het gebruik van deze "targeted middelen", met of zonder chemotherapie, zou wellicht beter MDR omzeilen en het antikanker effect verhogen. De afgelopen tien jaar zijn talrijke nieuwe "targeted" antikanker middelen, specifiek voor intra- en extra cellulaire tumor doelwitten, ontwikkeld. Op dit moment is er toenemend bewijs dat verscheidene van deze middelen (als monotherapie of in combinatie met chemotherapie) de antikanker effecten verhogen.

Een subgroep van deze stoffen is gericht tegen het zogenaamde proces van "angiogenese". Dit proces van nieuwe bloedvatvorming is niet alleen belangrijk in de ontwikkeling van normaal weefsel, maar is ook één van de pilaren in de vorming van kanker. Reeds dertig jaar geleden werd erkend dat kanker gezwellen bloedvaten nodig hebben voor hun groei vanwege de levering van voedingsstoffen en zuurstof, en het verwijderen van metabole afvalstoffen. Tevens bieden deze bloedvaten een route voor het verspreiden van uitzaaiingen elders in het lichaam. Een belangrijke factor betrokken bij angiogenese is vascular endothelial growth factor A (hierna genoemd als VEGF). VEGF wordt door vele verschillende vormen van kanker tot expressie gebracht en induceert kanker neovascularisatie. De verhoogde expressie van VEGF in vele kanker vormen maakt VEGF een rationeel doel voor anti-angiogene therapie (het tegengaan van bloedvatvorming). Antilichamen die zich binden aan VEGF, chemische moleculen die signalering van VEGF receptoren blokkeren alsmede geneesmiddelen die de intracellulaire tumor signaleringsroutes uitschakelen die van invloed zijn bij angiogenesis, zijn ontwikkeld. Hoewel anti-angiogene behandeling, hetzij als

monotherapie of in combinatie met chemotherapie heeft geresulteerd in verbetering in de behandeluitkomst voor verschillende tumor typen, zoals niercelkanker en darmkanker, is het effect bescheiden en vaak maar tijdelijk. Om deze reden zou het buiten gewoon nuttig zijn wanneer er een voorspellende test zou bestaan om patiënten te selecteren die baat hebben bij deze behandeling. Een optie hiervoor is het gebruik van moleculaire beeldvormende technieken.

Dit proefschrift is gericht op het omzeilen van geneesmiddelresistentie bij kanker en de ontwikkeling van nieuwe beeldvormende technieken om nieuwe behandelingen te evalueren, met name gefocust op het monitoren van anti-angiogene middelen en het ontwikkeling en evalueren van VEGF tracers.

In hoofdstuk 2 is een overzicht gegeven van de beeldvormende modaliteiten die kunnen worden gebruikt om MDR te visualiseren en de mogelijkheden om meer specifieke doelwitten in de tumor af te beelden voor de follow-up van "targeted" therapieën. Om MDR te overwinnen, en de werkzaamheid van chemotherapie te vergroten, middels het blokkereren van drugs efflux pompen, is niet succesvol gebleken in de kliniek. Op dit moment lijkt de toevoeging van nieuwe meer doelgerichte therapieën een betere optie om MDR te omzeilen. Het blokkeren van specifieke groeifactoren, intracellulaire doelwitten en receptorsignalering hebben de werkzaamheid van klassieke chemotherapie verhoogd in verschillende vormen van kanker. Dit succes is echter beperkt omdat veel patiënten geen baat hebben bij het toevoegen van deze nieuwe "targeted" geneesmiddelen. Om patiënten te selecteren, of om een behandeling te vervolgen, zijn nieuwe tracers en beeldvormende technieken nodig die specifieke veranderingen in de doelwitten van de kankercel of zijn micro-omgeving laten zien. Twee voorbeelden van hiervan zijn HER2 en VEGF imaging, aangezien beide een doelwit zijn voor geneesmiddelen die gebruikt kunnen worden om MDR tegen te gaan. De receptor HER2 komt tot overexpressie in 20 tot 30% van de borstkanker patiënten. Het HER2 antilichaam trastuzumab vergroot de antikanker effecten van MDR geneesmiddelen als de taxanen. Als gevolg hiervan vermindert trastuzumab taxane resistentie. Tussen tumoren kan de HER2 expressie variëren, zowel tijdens de behandeling als tussen laesies binnen één patiënt. Om deze reden is er behoefte aan een methode die de HER2 status non-invasief herhaaldelijk kan beoordelen. Moleculaire beeldvorming van de HER2 receptor zou voorzien in deze behoefte. Naast dit diagnostische doel, kan HER2 imaging ook gebruikt worden als een vroegtijdige voorspellende marker voor effectiviteit van HER2 verlagende behandelingen. HER2 imaging begint met het selecteren van een geschikte HER2 tracer. Op dit moment zijn verschillende HER2 gericht moleculen beschikbaar zoals monoklonale

antilichamen, Fab-fragmenten, $F(ab')_2$-fragmenten, diabodies, minibodies, affibodies, scFv-FC en peptiden. (Pre)-klinisch, hebben deze HER2 tracers aangetoond tumoren met HER2 overexpressie te kunnen visualiseren en is follow-up van HER2 gericht therapieën mogelijk. Klinische studies zullen snel volgen.

Zoals hierboven is beschreven, is VEGF een van de belangrijkste groeifactoren tijdens angiogenese. VEGF bestaat uit ten minste vijf verschillende isoformen (A-E). VEGF-A is een van de meest belangrijke groeifactoren die betrokken is bij tumor angiogenese en bestaat uit verschillende splice varianten, namelijk VEGF 121, 145, 165, 189 en 206. $VEGF_{121}$ is vrij oplosbaar, terwijl bij $VEGF_{165}$ een aanzienlijke deel gelokaliseerd blijft in de extracellulaire matrix, net als bij $VEGF_{189}$ en $VEGF_{206}$. VEGF is een downstream product waarvan de transcriptie gereguleerd wordt door onder andere groeifactor receptoren zoals de HER2 receptor, de epidermale groeifactor receptor 1 en intracellulaire eiwitten als hypoxia inducible factor 1α (HIF1α), mTOR en heat shock protein 90 (HSP90). Om deze reden kan VEGF imaging dienen als een uitleesmodaliteit voor behandelingen die deze factoren in de VEGF transcriptie moduleren. Tot op heden zijn verschillende radioactief gelabelde anti-VEGF antilichamen en Fab fragmenten gebruikt voor de ontwikkeling van VEGF imaging: VG76e, HumMV833, bevacizumab en ranibizumab. Zoals aangetoond in dit proefschrift zijn de tracers een veelbelovend instrument in de follow-up van de anti-angiogene therapie.

Drugs efflux pompen spelen een belangrijke rol in de bescherming van de hersenen tegen toxische stoffen en zijn wellicht een belangrijke reden waarom chemotherapeutica niet het hersenweefsel bereiken in adequate dosering. De bloed-hersenbarrière (BBB) wordt gevormd door gespecialiseerde capillaire endotheelcellen die verschillende eigenschappen hebben, zoals nauw aaneengesloten tot elkaar met een hoge elektrische weerstand, het ontbreken van openingen en de aanwezigheid van efflux pompen zoals P-gp en het MDR eiwit MRP1. Strategieën om de fysieke eigenschappen van het capillaire endotheel van de BBB te wijzigen zijn o.a. het gebruik van hypertone oplossingen en bradykinine analoga. Andere strategieën zijn gericht op het remmen van de functie van de efflux pompen. Op dit moment is dit concept het meest bij P-gp onderzocht. Studies bij knaagdieren hebben uitgewezen dat de P-gp functie kan worden geremd met cyclosporine A. Om de toxische bijwerkingen van cyclosporine A te omzeilen bij patiënten dienen ook andere therapieën die van invloed zijn op de P-gp functie en/of expressie te worden gebruikt. In hoofdstuk 3 beschrijven we een voorbeeld hiervan. De gevolgen van bestraling op de functie en expressie van P-gp zijn beschreven. Het effect is onderzocht in gezonde rattenhersenen met behulp van het radioactieve P-gp PET substraat [^{11}C]carvedilol. De rechterhemisfeer van de hersenen

werden lokaal bestraald met één dosis van 2-25 Gy, gevolgd door intraveneuze toevoeging van 10 mg/kg van het P-gp substraat cyclosporine A, enkelvoudige bestraling met een dosis van 15 Gy gevolgd door verschillende doseringen cyclosporine A (10, 15 of 20 mg/kg), of gefractioneerde bestraling (4 x 5 Gy) gevolgd door cyclosporine A (10 mg/kg) 5 dagen later. Bestraling van de hersenen verhoogde de [^{11} C]carvedilol opname dosis afhankelijk tot een maximum van 20% ten opzichte van de niet-bestraalde hersenhelft. Bovendien verhoogde cyclosporine A ook de [^{11} C]carvedilol opname dosis afhankelijk in beide hersenhelften, echter meer in de bestraalde hersenhelft. Gefractioneerde bestraling resulteerde in een volledig verlies van P-gp expressie 10 dagen na het begin van de bestraling wat samenviel met een toegenomen [^{11} C]carvedilol opname. Hersenenbestraling wordt vaak toegepast bij patiënten met uitzaaiingen in de hersenen. Om deze reden kan men speculeren dat bestraling kan leiden tot een tijdelijk venster dat tot verhoogde opname van chemotherapeutica lijdt die een P-gp substraat zijn.

In hoofdstuk 4 tot en met 7 hebben we de ontwikkeling en evaluatie van nieuwe VEGF tracers en het gebruik hiervan in de follow-up van "targeted" therapieën beschreven. Hierbij hebben we ons gericht op de ontwikkeling van moleculaire tracers, die non-invasief de angiogene status van de tumor in kaart brengen. Onze hypothese is dat deze beeldvorming .tot een betere selectie van patiënten en vroegtijdige voorspelling van het effect van anti-angiogene therapie lijdt. In hoofdstuk 4 hebben we de ontwikkeling van radioactief gelabeld bevacizumab beschreven. Bevacizumab, een gehumaniseerd monoklonaal antilichaam met hoge affiniteit voor alle VEGF-A isoformen, hebben we gelabeld met de lang levende isotopen ^{111}In en ^{89}Zr voor SPECT en PET imaging. In vitro testen toonde een stabiliteit gedurende minimaal 168 uur en onveranderde immunoreactiviteit tegen VEGF-A. Dit waarborgt optimale *in vivo* imaging. Bij *in vivo* experimenten werd een zeer goede tumor visualisatie waargenomen, vanaf 72 uur na injectie van de tracer. Maximale opname vond plaats 168 uur na injectie. Tumor opname was aanzienlijk hoger vergeleken met het niet-specifieke controle ^{89}Zr-IgG. Deze resultaten tonen aan dat de opname in de tumor VEGF gedreven is. Bovendien was microPET kwantificering van ^{89} Zr-bevacizumab vergelijkbaar met *ex vivo* biodistributie kwantificering, wat aantoont dat niet-invasieve follow-up van ^{89}Zr-bevacizumab mogelijk is. Histologische experimenten toonde vervolgens aan dat ^{89}Zr-bevacizumab zich met name bevindt in de tumor bloedvaten en de extracellulaire matrix. Deze resultaten lieten zien dat ^{89}Zr-bevacizumab mogelijk kan worden gebruikt voor de behandel follow-up van anti-angiogene behandeling.

In hoofdstuk 5 hebben we ^{89}Zr-bevacizumab gebruikt voor vroege anti-angiogene evaluatie van de HSP90 remmer NVP-AUY922. HSP90 is een moleculaire chaperone eiwit

dat betrokken is bij de handhaving van de stabiliteit, de conformatie en de lokalisatie van verschillende sleutel eiwitten die betrokken zijn in de progressie van kanker. HSP90 komt 2 tot 10 keer zoveel tot expressie in kankercellen en is actief in multi-chaperone complexen, waardoor kankercellen relatief gevoelig zijn voor behandeling met HSP90 remmers ten opzichte van gezond weefsel. Op dit moment zijn er geen biomarkers aanwezig die het effect van HSP90 remming kunnen voorspellen. Een manier om HSP90 therapie te monitoren is het volgen van veranderingen in cliënteiwitten van HSP90. Cliënteiwitten van HSP90 zijn o.a. groeifactorreceptoren zoals de epidermale groeifactor receptor 1 en 2 (EGFR en HER2) en transcriptie factoren als hypoxia inducible factor 1α (HIF1α). Helaas kunnen de meeste van deze cliënteiwitten alleen worden gemeten door het verzamelen van tumor weefsel. Om dit te omzeilen is moleculaire beeldvorming is een aantrekkelijk alternatief om zo herhaaldelijk follow-up van de specifieke targets mogelijk te maken. Onze hypothese is dat VEGF een geschikte kandidaat hiervoor is omdat het een downstream product is van verschillende HSP90 cliënteiwitten. In een A2780 ovariumkanker xenograft en een platinum resistente subcellijn CP70 hebben we ^{89}Zr-bevacizumab microPET uitgevoerd vóór en na behandeling met de HSP90 remmer NVP-AUY922. Vervolgens hebben we de imaging resultaten geverifieerd met de histologische respons en *ex vivo* tumor VEGF levels. Twee weken behandeling met NVP-AUY922 resulteerde in een 44.4% daling in de ^{89}Zr-bevacizumab tumor opname in de A2780 xenografts, terwijl de tumor opname niet beïnvloed werd door NVP-AUY922 in de CP70 xenografts vergeleken met de baseline waarden. Hetzelfde patroon werd waargenomen voor A2780 en CP70 tumoren bij de *ex vivo* VEGF tumor levels, gemeten met kwantitatieve ELISA, en de vaatdichtheid. Bovendien komen deze bevindingen overeen met een verminderde tumor proliferatie in het A2780 tumor weefsel, terwijl er geen verandering werd waargenomen in het CP70 tumor weefsel. Samenvattend, de ^{89}Zr-bevacizumab PET imaging resultaten zijn in overeenstemming met de anti-angiogene response en directe anti-tumor effecten van NVP-AUY922 behandeling. Deze resultaten ondersteunen dat ^{89}Zr-bevacizumab een specifieke techniek is voor het *in vivo* vervolgen van HSP90 remming.

In hoofdstuk 6 hebben wij de feasibility van VEGF imaging in stadium III/IV melanoom patiënten onderzocht. De feasibility van ^{111}In-bevacizumab SPECT VEGF imaging werd vergeleken met ^{18}F-FDG PET, een glucose analoog dat de glucose opname- en het metabolisme van de tumor afbeeld, en met CT imaging in lymf klier positieve stadium III en IV melanoom patiënten. VEGF SPECT visualiseerde alle bekende melanoom laesies (grootte 1-10 cm) die eerder geïdentificeerd waren door CT en ^{18}F-FDG PET imaging. Optimale tumor opname werd 4 dagen na injectie van ^{111}In-bevacizumab waargenomen

wat overeenkomt met de relatief langzame farmacokinetiek van monoklonale antilichamen. Niet-specifieke lever opname van ^{111}In-bevacizumab was vergelijkbaar als voor andere radioactieve antilichamen, zoals ^{111}In-trastuzumab. Door de relatief trage klaring van ^{111}In-bevacizumab is er maximale tumor blootstelling wat de accumulatie in de tumor ten goed komt terwijl niet-specifieke opname in andere organen afneemt in de tijd.

Een grote variatie in ^{111}In-bevacizumab tumor opname werd aangetroffen tussen patiënten, tussen laesies bij patiënten en binnen laesies van één patiënt. Toekomstige studies moeten verder de rol van VEGF imaging aantonen, bijvoorbeeld in het selecteren van laesies met hoge VEGF expressie en optimale "dose finding" van bevacizumab therapie in individuele patiënten.

In hoofdstuk 6B beschrijven we het effect van bevacizumab behandeling bij een patiënt met vaatmalformaties in de pancreas veroorzaakt door de erfelijke ziekte HHT. Een VEGF scan vóór start van de bevacizumab behandeling toonde een verhoogde opname in de vaatmalformaties. Direct na de start van de bevacizumab behandeling stopte de bloedneuzen, werden de vaattekenen van de huid minder uitgesproken en nam de frequentie en ernst van de pancreatitis geleidelijk af wat uiteindelijk verdween. Deze resultaten illustreren het potentieel van VEGF imaging en anti-VEGF behandeling bij ziekten buiten de oncologie.

Op dit moment zijn er veel vragen die betrekking hebben op de heterogeniteit van de tumor response en resistentie tegen anti-angiogene therapieën. Geneesmiddelen die de VEGF/VEGF-receptor interactie blokkeren zoals de klinisch gebruikte receptor tyrosine kinase remmer sunitinib kunnen, afgezien van de anti-angiogene effecten op de primaire tumor, ook leiden tot toegenomen invasiviteit aan de tumor rand en de vorming van nieuwe metastasen. Deze complexe en dynamische interactie tussen tumorcellen en hun micro-omgeving kan een belangrijke reden zijn waarom alle biomarkers die tot nu toe getest zijn falen om response op anti-angiogenic therapie te voorspellen. Moleculaire beeldvorming kan misschien een betere inzicht geven hoe een tumor op anti-angiogene behandeling reageert. In hoofdstuk 7 hebben we in twee xenograft muis modellen de impact van sunitinib behandeling en onthouding van behandeling onderzocht met een drietal beeldvormende technieken, namelijk met ^{18}F-FDG, ^{15}O water PET (voor tumor perfusie meting) en ^{89}Zr-ranibizumab VEGF PET. Hierna zijn de imaging resultaten vergeleken met tumor groei, VEGF plasma levels en histologische bevindingen. In zowel de A2780 als de Colo205 xenograft zorgde behandeling met sunitinib voor remming van de tumorgroei in vergelijking met niet-behandelde dieren. Wanneer sunitinib behandeling vervolgens werd gestopt, resulteerde dit in een snelle hervatting van de tumorgroei. Terwijl ^{18}F-FDG een homogene tumor response liet zien, met 50% vermindering van de opname ten opzichte van controle, liet ^{15}O water PET geen duidelijk verschillen

zien in tumor perfusie. Dit is waarschijnlijk vooral te wijten aan de lage gevoeligheid van deze techniek, gezien de lage tumor perfusie in vergelijking tot andere organen. Tot onze verassing liet ^{89}Zr-ranibizumab VEGF PET slechts een minimale afname (-19 procent) na sunitinib behandeling in tumor rand zien, maar een enorme daling (- 45 %) in het centrum van de tumor met een sterke opleving (+ 65 %) na stopzetting van de behandeling. Om te controleren welke PET-techniek het beste de angiogene tumor reactie na sunitinib behandeling en onthouding weergaf hebben we grondig de imaging resultaten vergeleken met bioluminescentie, immunohistochemie alsmede plasma VEGF levels. Dit leidde tot een aantal prominente bevindingen. Als verwacht leidde 7 dagen sunitinib behandeling tot een afname van een aantal angiogene markers zoals de vaatdichtheid, de vaatdiameter en de VEGFR2 expressie, echter meer in het centrum van de tumor dan in de tumor rand. Hiernaast was er een afname van de endotheel proliferatie, verhoogde GLUT-1 expressie en een verhoogde HIF1α expressie. VEGF-A kleuringen waren op dag 7 minder intense in het centrum van de tumor dan de tumorrand wat overeen kwam met de angiogene status van de tumor. Dit correspondeerde eveneens met de tumorcel proliferatie die hoog bleef aan de tumorrand na behandeling. De opvallende bevinding van een initiële VEGF daling tijdens behandeling met sunitinib, zoals gedetecteerd met immunohistochemie en VEGF PET, kan mogelijk worden verklaard door het feit dat sunitinib afgezien van de VEGFR's ook 73 andere kinases bindt, die leiden verschillende zogenaamde "off-target' effecten. Daarnaast constateerde we dat de tumor response veranderde gedurende de behandeling en dat er een snelle tumor revascularisatie optreedt na het staken van de behandeling, wat overeenkomt met de bevindingen van de VEGF PET. Deze resultaten demonstreren de mogelijkheid om met VEGF PET niet-invasief inzicht te krijgen in gebieden van de tumor die wel en niet reageren op anti-angiogene behandeling. Bovendien hebben we laten zien dat deze techniek ook haalbaar is in de klinische praktijk met als voorbeeld een patiënt met uitgezaaid niercelkanker waarbij VEGF PET long, mediastinale, bot en hersenlaesies aantoonde. Dit maakt translatie van deze techniek mogelijk wat gebruikt kan worden voor de follow-up van nieuwe behandel strategieën, optimale "dose finding" en evaluatie van nieuwe geneesmiddel combinaties om zo de effectiviteit van anti-angiogene therapieën te vergroten.

Samenvattend, de twee nieuw ontwikkelde VEGF tracers hebben veelbelovende mogelijkheden weergeven voor zowel het visualiseren van tumoren alsmede de follow-up van de anti-angiogene therapie.

Chapter 11

Dankwoord

Tijdens je promotieonderzoek zijn er tal van momenten dat je als een monnik te werk gaat. Alleen in de kelder van het UMCG, om 3 uur 's nachts, muizen scannen. De tijd gaat langzaam en je geest is niet meer zo helder. Of dat je met behulp van een computerprogramma tumoren intekent, millimeter voor millimeter, 20 plakjes per tumor, in totaal zo'n 200 tumoren. Dit is echter maar een gedeelte van je werkzaamheden. Het merendeel is met name een project dat je met vele collega's samen uitvoert, en wat je zonder hulp van anderen niet tot een goed einde kan brengen. Iedereen brengt hierbij zijn eigen kennis in. Dit heeft ons denk ik ver gebracht tijdens mijn promotietraject. Wat begon met het labelen van bevacizumab in het laboratorium, heeft na dierstudies geresulteerd in diverse klinische studies. Dit translationele karakter komt ook in uitdrukking in de verscheidenheid aan co-auteurs die hebben geholpen bij de verschillende hoofdstukken: 36 in totaal! Daarnaast hebben nog vele mensen geholpen in de ondersteuning van alle experimenten en de patiëntenstudies. Om 50 tot 100 personen persoonlijk te bedanken bij dit schrijven gaat helaas niet. Jullie weten echter goed hoe belangrijk jullie zijn geweest de afgelopen jaren voor ons onderzoek, bij deze veel dank! Graag wil ik echter een paar mensen er kort uitlichten.

Geachte Prof. Dr. E.G.E. de Vries, beste Liesbeth, iedereen die jou een beetje kent weet hoeveel ik hier kan opschrijven. Jouw gedrevenheid is onnavolgbaar. Met een enorme betrokkenheid begeleidt je vele projecten en weet je het beste uit onderzoekers te halen. Waar ik je echter met name voor wil bedanken is het enorme plezier dat je me gegeven hebt de afgelopen jaren. Je staat altijd open voor ideeën en hebt mij betrokken bij vele nieuwe projecten. Dit heeft mij enorm gestimuleerd. Om 6 uur 's ochtends vergaderen op ASCO was doorbijten. Het heeft me echter geleerd wat allemaal bij onderzoek doen komt kijken. Ik heb dit als zeer bijzonder ervaren. Ik kijk er naar uit om in de nabije toekomst nog vele projecten samen op te zetten.

Geachte Dr. M.N. Lub-de Hooge, beste Marjolijn, ik ben erg blij dat je mijn co-promotor bent. Als ziekenhuisapotheker was je van onschatbare waarde voor mijn onderzoek. Ondanks de 100-en-1 taken die je in het ziekenhuis hebt, ben je altijd bereikbaar geweest en heb je praktisch meegedacht over de experimenten. Samen hebben we de farmaceutische analyses van alle labelingen uitgevoerd. Zonder jouw kennis was het niet mogelijk geweest binnen 2 jaar een klinische studie uit te voeren. In tussentijd ben je ook nog moeder geworden van twee prachtige kinderen. Met veel respect en plezier denk ik terug aan deze tijd.

Geachte Dr. G.A.P. Hospers en Dr. A.H. Brouwers, beste Geke en Adrienne. Samen met Liesbeth en Marjolijn zijn jullie belangrijke begeleiders geweest tijdens mijn onderzoek en mijn co-promotoren. De patiëntenstudies zijn door jullie inzet een succes geworden. Geke, dank voor alle hulp bij de melanoomstudie. Adrienne, jouw kennis is cruciaal voor de translatie van onze dierstudies naar klinische nucleaire geneeskunde.
Geachte Prof. Dr. J.A. Gietema, Prof. Dr. N.H. Mulder, Dr. C.P. Schroder en Drs. S.F Oosting, beste Jourik, Nanno, Carolien en Sjoukje. Ik kijk met plezier terug op onze projecten! Met een heel team hebben we aan de manuscripten gewerkt. Jourik, jouw enthousiasme en inzicht inspireert enorm, veel dank hiervoor! Nanno, jouw scherpte en analytisch vermogen is erg verhelderend geweest. Carolien en Sjoukje, jullie schrijfstijl is fantastisch en hebben mijn stukken enorm geholpen.

Geachte Prof. Dr. H. Hollema, Prof. Dr. R.A. Dierckx, Prof. Dr. H.J. Hoekstra en Dr. W.F.A. den Dunnen, beste Harry, Rudi, Harold en Wilfred. Het multidisciplinaire karakter van ons onderzoek is erg belangrijk. Beste Harry en Wilfred, dank voor alle hulp en inzet bij het opzetten en beoordelen van de immunohistochemie. Dit gedeelte was onontbeerlijk voor het interpreteren van de imaging resultaten. Beste Rudi, dank voor het plezier en vertrouwen dat je mij hebt gegeven om onderzoek te doen op de afdeling Nucleaire Geneeskunde en Moleculaire Beeldvorming. Beste Harald, met veel inzet heb je onze melanoom studie tot een succes gebracht, hiervoor dank.

Beste Drs. T.H. Oude Munnink, Thijs, dat deze alinea hier pas staat doet geen recht aan de plaats die jij verdient in het dankwoord. Ik heb het enorm leuk gevonden dat jij 2 jaar geleden besloten hebt om bij de afdeling medische oncologie onderzoek te gaan doen. Na ons bestuursjaar bij Farmacie een mooie hereniging die wederom naar mijn mening erg gezellig en toch ook nog productief is verlopen. Dit is dan ook 1 van de dingen die ik het meeste mis aan het onderzoek. Ik ben trots dat jij mijn paranimf bent!

Beste Drs. E.C.F. Dijkers, beste Eli, samen zijn we begonnen met de ^{89}Zr labeling van de antilichamen. Alvorens ik begon had jij al bergen werk verzet. Dank voor alle begeleiding in het begin en succes met de laatste loodjes van jouw proefschrift.

Beste Dr. H. Timmer-Bosscha en Dr J. Meijer, Hetty en Coby, zonder jullie ondersteuning is het onderzoek op het lab niet mogelijk. Hetty en Coby, ondanks dat ik af en toe als "rupsje-nooit-genoeg" acute bestellingen plaatste en op zeer korte termijn cellen nodig had, mocht ik langs blijven komen.

Beste Kirsten, Esther, Sander, Nienke en Frank-Jan. Kirsten, met een fantastische inzet en veel kennis heb je Thijs en mij geholpen. Helaas voor ons vond jij een erg leuke baan dichter bij huis. We hebben je erg gemist! Esther, ter overbrugging heb je tijdelijk als analist op mijn project gewerkt. Voor mij heb je echter letterlijk bergen met werk verzet. Dank hiervoor en voor de gezellige samenwerking. Ik wens je alle succes met je huidige project op de afdeling medisch oncologie. Sander, samen met Thijs hebben we denk ik de HSP studies tot een goed einde gebracht. Daarnaast dank voor alle hulp bij de celkweken voor mijn dierstudies. Nienke en Frank-Jan, beide begonnen jullie zonder enige voorkennis als student op een oncologisch project. Na enkele weken konden jullie echter zelfstandig vele experimenten uitvoeren. Frank-Jan, jouw kennis en kunde bleef niet alleen bij ons onopgemerkt, maar ook in Engeland maakte je indruk! Beide succes met de rest van jullie studie!

Beste collega's van MOL de Vitrine! Ondanks dat ik het merendeel van mijn tijd heb doorgebracht op het laboratorium van de Nucleaire Geneeskunde heb ik me wel altijd onderdeel van "de groep" gevoeld. Ik heb een erg leuke tijd gehad waarbij het denk ik bijzonder is dat altijd iedereen voor elkaar klaar staat. Ook naast het werk, zoals tijdens de congresbezoeken in de Verenigde Staten, heb ik veel plezier met jullie beleefd. Ik zal dit erg missen nu ik begonnen ben in de kliniek.

Beste collega's van de afdeling Nucleaire Geneeskunde en Moleculaire Beeldvorming. Het is niet altijd gemakkelijk om met zoveel mensen van andere afdelingen samen te werken. Desondanks hebben we met elkaar mooie resultaten weten te behalen. Beste Hans, dank voor het scannen van de patiënten, zelfs op feestdagen was dit voor jou geen probleem! Ik drink graag samen nog een keer een glas wijn als dank. Beste Johan en Philip, dank voor het aanvullen van mijn fysische en chemische kennis, het heeft denk ik tot mooie resultaten geleid.

Beste vrienden, de afgelopen jaren heb ik helaas vaak weinig tijd gehad. Hopelijk is er de komende tijd weer meer tijd om te fietsen, te hockeyen en om elkaar op te zoeken. Beste Bjorn, wat samen begon als ons bijvak Farmacie is uitgemond in mijn promotie. Ik geniet van onze uurtjes filosoferen en ben trots dat jij mijn paranimf bent! Beste Wouter, Ramon, Sander en Martijn, zelfs mij op het vliegtuig zetten tijdens onze fietsvakantie omdat ik een dierstudie moest af maken was geen probleem voor jullie. Ik denk dat het fantastisch is wat we samen hebben en kijk uit naar onze 10e gezamenlijke vakantie!

Lieve (schoon)familie, lieve pap en mam. Al vanaf jongs af aan hebben jullie Annemiek, Marleen en mij gestimuleerd en vrij gelaten in onze keuzes. Ook mijn keuze om na mijn studie Farmacie nog Geneeskunde te gaan studeren en te gaan promoveren hebben jullie met 100% gesteund. De komende tijd is er hopelijk weer wat meer tijd om met elkaar dingen te ondernemen. Pap, komend jaar gezellig samen op congres?!

Lieve Maartje, mede dankzij jouw optimisme en steun is deze promotie zo goed verlopen. Ondanks het feit, dat ik het liefst alle dagen vakantie met jou zou willen hebben, wist jij zelfs de werkmomenten die we samen hadden in kleine "feestjes" om te zetten. Het samen lekker fietsen, de weekendjes weg en het samen opknappen van onze nieuwe "Casa" in de spaarzame vrije tijd die we hadden waren fantastisch! Het komende jaar zal ik je net zo goed proberen te helpen bij het afronden van jouw promotie! Lieve Maartje, met jou is 1 + 1 = 3.

Wouter

Appendix

Color figures

Chapter 2

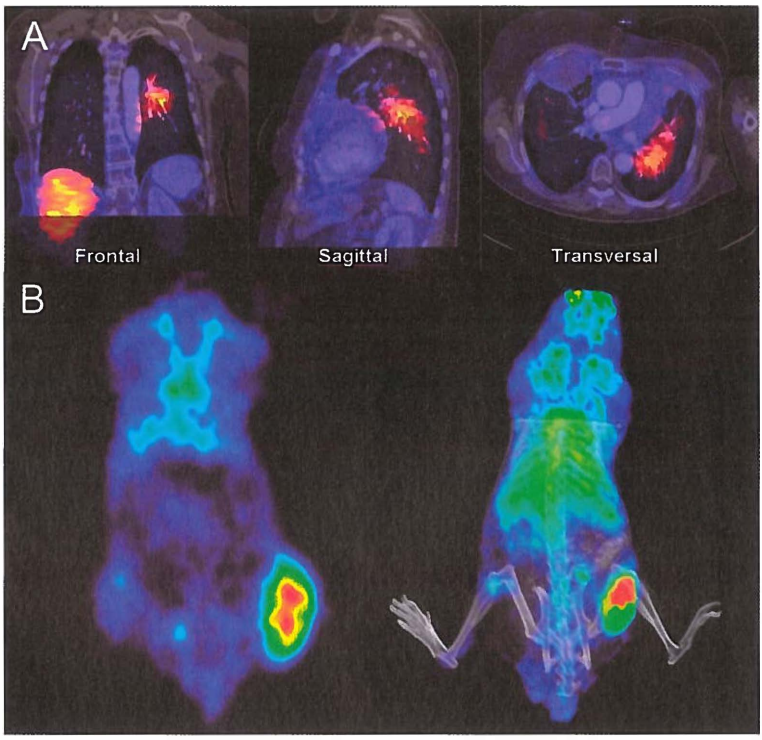

Figure 1. (A) Fused computed tomography (CT) with indium-111–diethylenetriamine penta-acetic acid anhydride (111In-DTPA) –trastuzumab single-photon emission tomography (SPECT) image (96 h after tracer injection). Tumor indicated by arrow. *Reproduced with permission of The Journal of Clinical Oncology*. (B) Coronal ^{89}Zr-bevacizumab MicroPET image and fused 3D ^{89}Zr-bevacizumab/CT image 144 h post injection. (see page 21)

Chapter 4

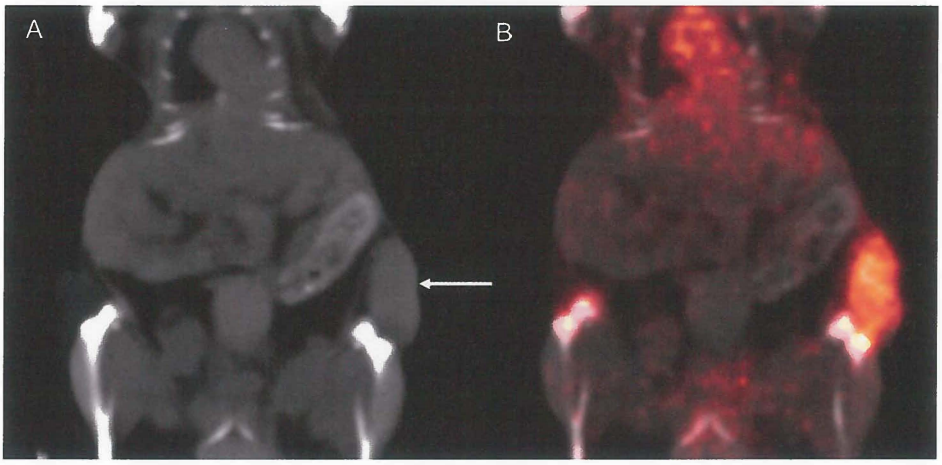

Figure 1. Coronal CT image (A) with clear subcutaneous localization of the SKOV-3 tumor (arrow). Fusion of MicroPET and CT images (B) (168 h post injection) enables adequate quantitative measurement of ^{89}Zr-bevacizumab in the tumor. (see page 54)

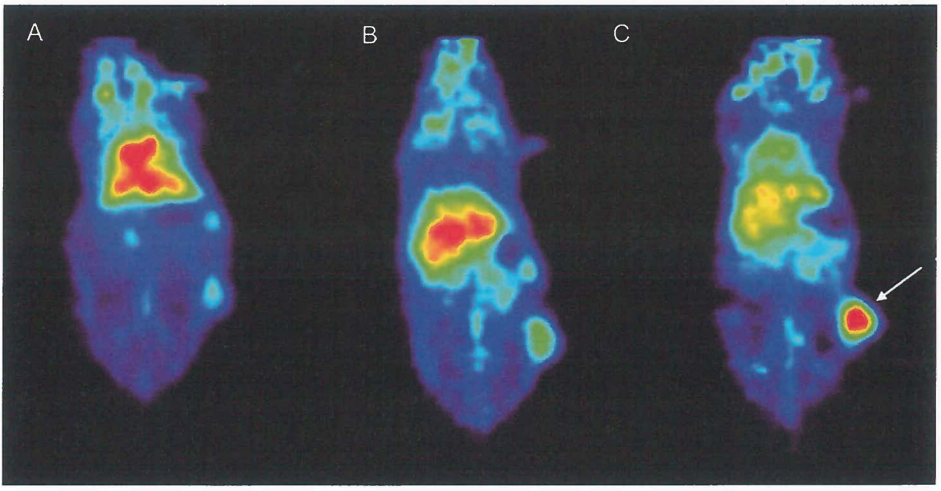

Figure 2. Coronal planes of MicroPET images 24 (A), 72 (B) and 168 h (C) post injection of ^{89}Zr-bevacizumab. At 24 h most uptake is in the well-perfused organs. In time, relative uptake in the tumor (arrow) increases. (see page 54)

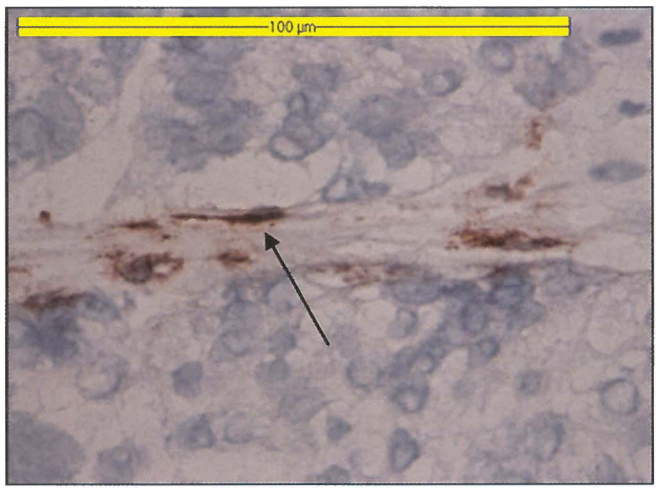

Figure 5. Anti-human IgG staining (arrow) in a tumor slice from mice receiving ^{89}Zr-bevacizumab.
(see page 58)

Chapter 5

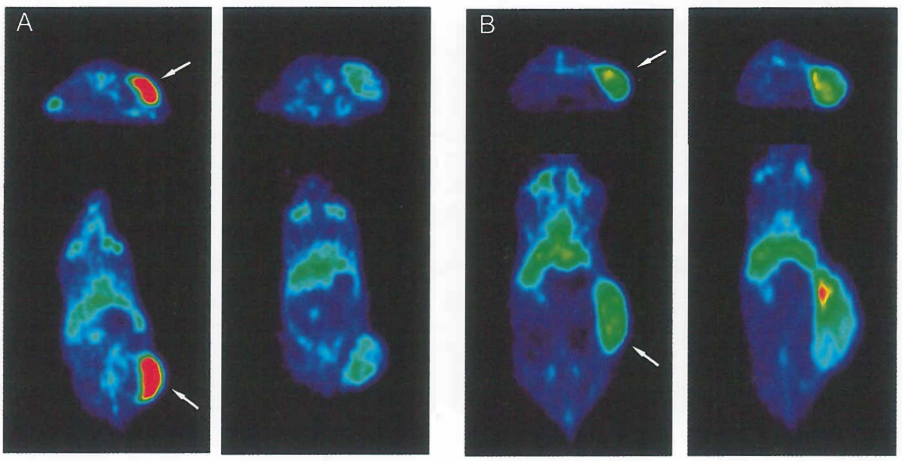

Figure 2. Representative transversal and coronal microPET images of ^{89}Zr-bevacizumab obtained pre-treatment of A2780 (A) and CP70 (B) xenografts (left panels), and following NVP-AUY922 treatment (right panels). Images were obtained 144 h after injection of ^{89}Zr-bevacizumab. Tumor is indicated by arrow. (see page 60)

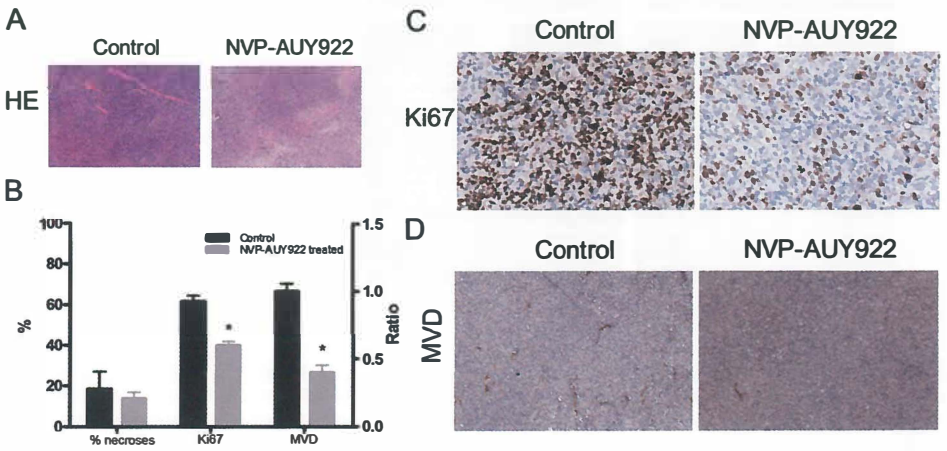

Figure 5. (A) Representative HE staining, (C) representative Ki67 staining, (B) % necroses, Ki67 staining and MVD (right Y-axis) (*$P < 0.05$) and (D) representative vWf staining for MVD of control and NVP-AUY922 treated A2780 xenograft. *Data is presented as mean ± SEM.* (see page 74)

Chapter 6

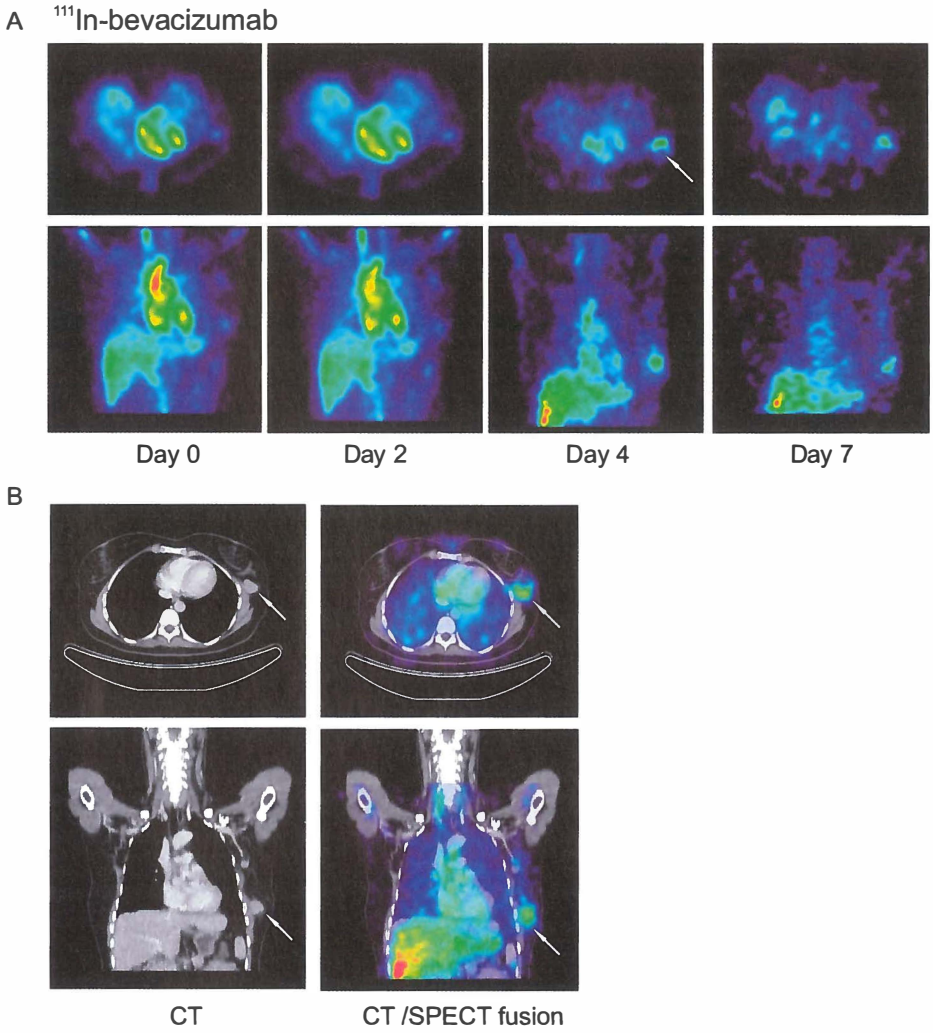

Figure 1. (A) Transversal and coronal VEGF-SPECT images at day 0, 2, 4 and 7 post injection of the tracer. In time, ^{111}In-bevacizumab accumulates in the tumor with optimal tumor to background ratio 4 days post injection. (B) Transversal and coronal CT image and VEGF SPECT/CT fusion 4 days post injection. (see page 86)

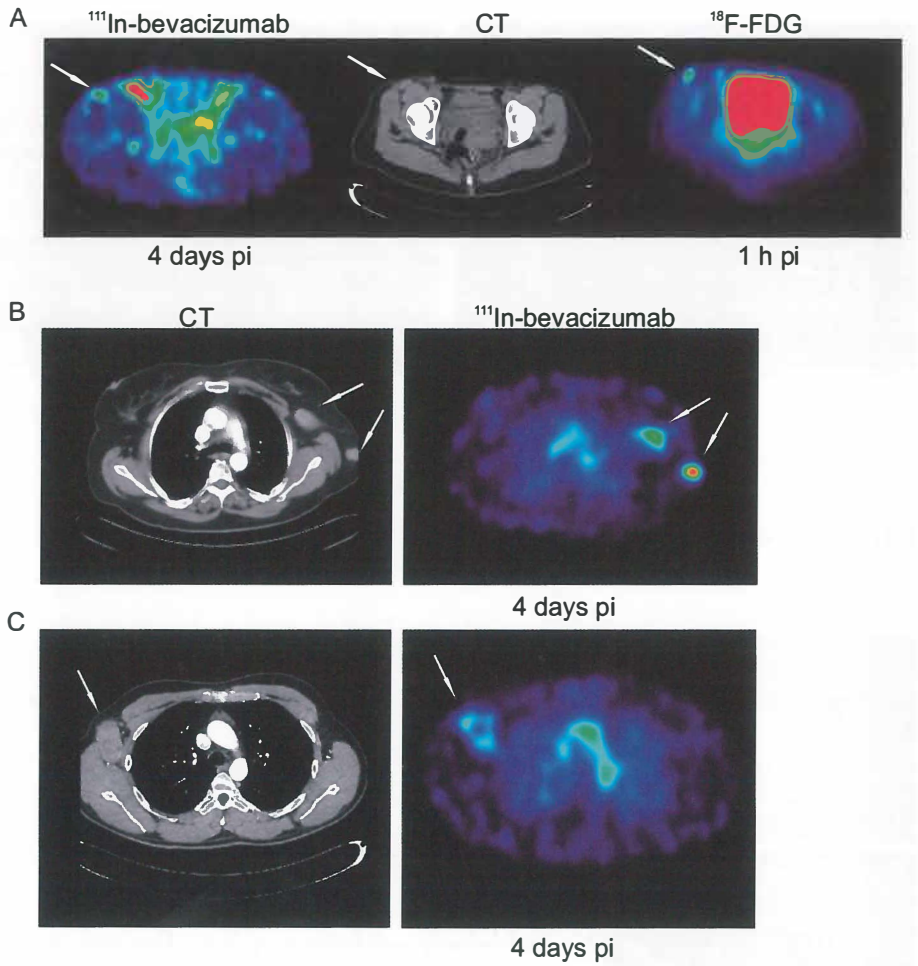

Figure 2. (A) Small melanoma lesions (white arrow), 12 mm in diameter on CT, detection by ^{111}In-bevacizumab, CT imaging and FDG imaging. (B) Differential ^{111}In-bevacizumab uptake between two melanoma lesions. (C) Inhomogeneous ^{111}In-bevacizumab tumor uptake in melanoma lesion. (see page 87)

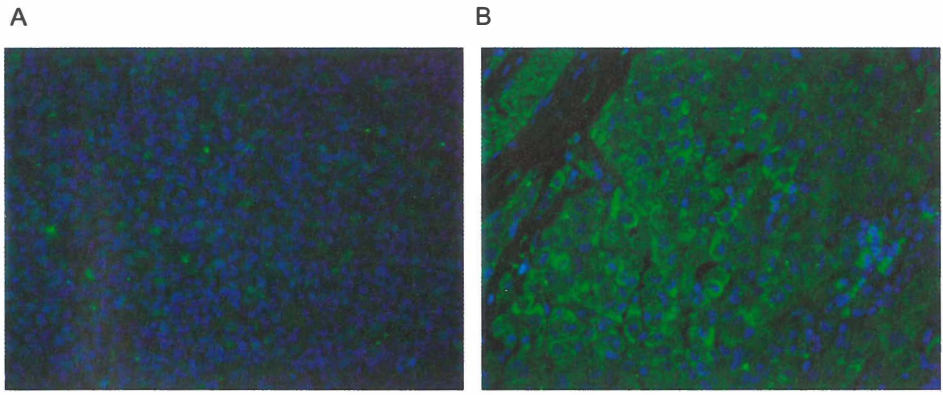

Figure 4. Weak (A) and strong (B) VEGF-A immunofluorescent staining of primary melanoma lesions. (see page 88)

Chapter 6B

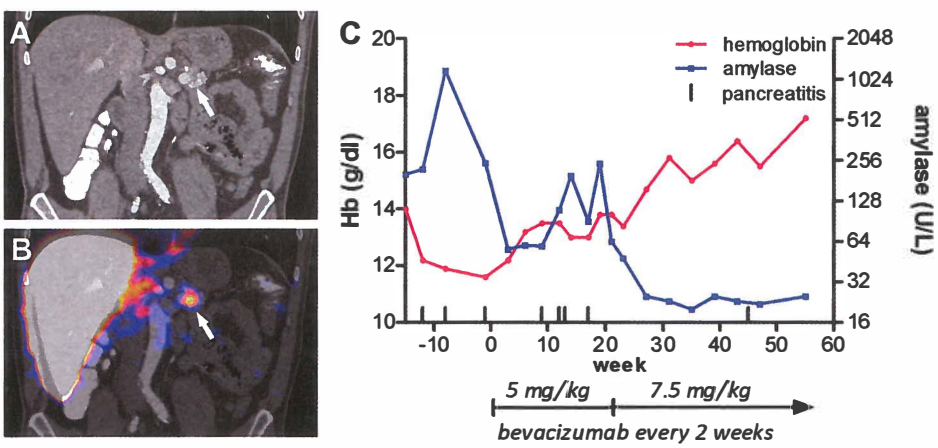

Figure 1. A. Coronal CT image of a patient with hereditary hemorrhagic telangiectasia with arteriovenous malformations (AVMs) in the pancreas (arrow). B. Fused coronal ^{111}In-bevacizumab SPECT/CT image . The SPECT image shows increased ^{111}In-bevacizumab uptake in an AVM (arrow) indicating increased local VEGF concentration. C. Changes in hemoglobin and serum amylase and pancreatitis episodes before and during treatment with bevacizumab. (see page 92)

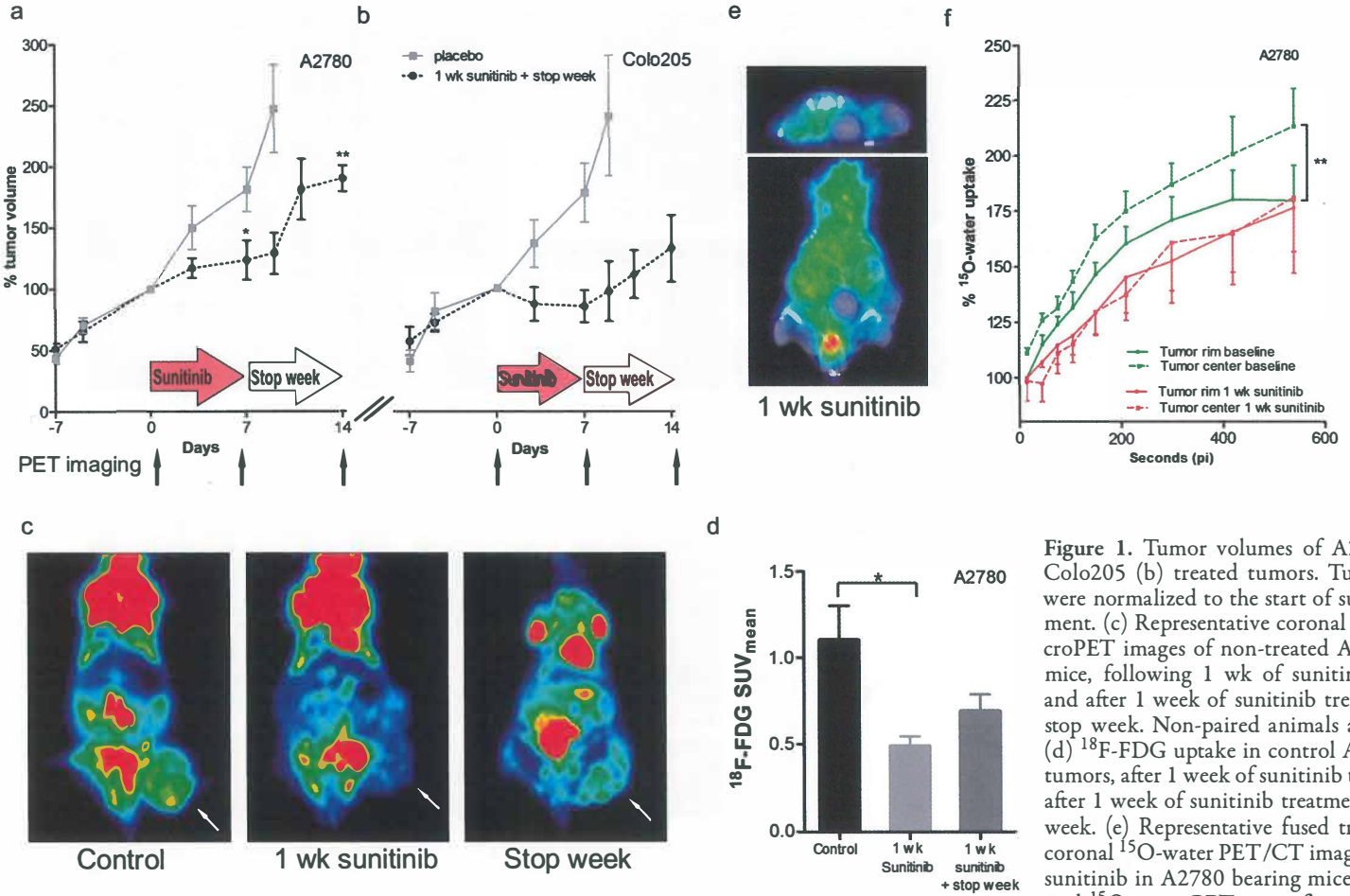

Figure 1. Tumor volumes of A2780 (a) and Colo205 (b) treated tumors. Tumor volumes were normalized to the start of sunitinib treatment. (c) Representative coronal ^{18}F-FDG microPET images of non-treated A2780 bearing mice, following 1 wk of sunitinib treatment and after 1 week of sunitinib treatment plus a stop week. Non-paired animals are presented. (d) ^{18}F-FDG uptake in control A2780 treated tumors, after 1 week of sunitinib treatment and after 1 week of sunitinib treatment plus a stop week. (e) Representative fused transversal and coronal ^{15}O-water PET/CT image after 1 week sunitinib in A2780 bearing mice. (f) Normalized ^{15}O-water PET quantification at baseline and following 1 week of sunitinib. * $P < 0.05$, ** $P < 0.01$. *Data presented as SEM.* (see page 99)

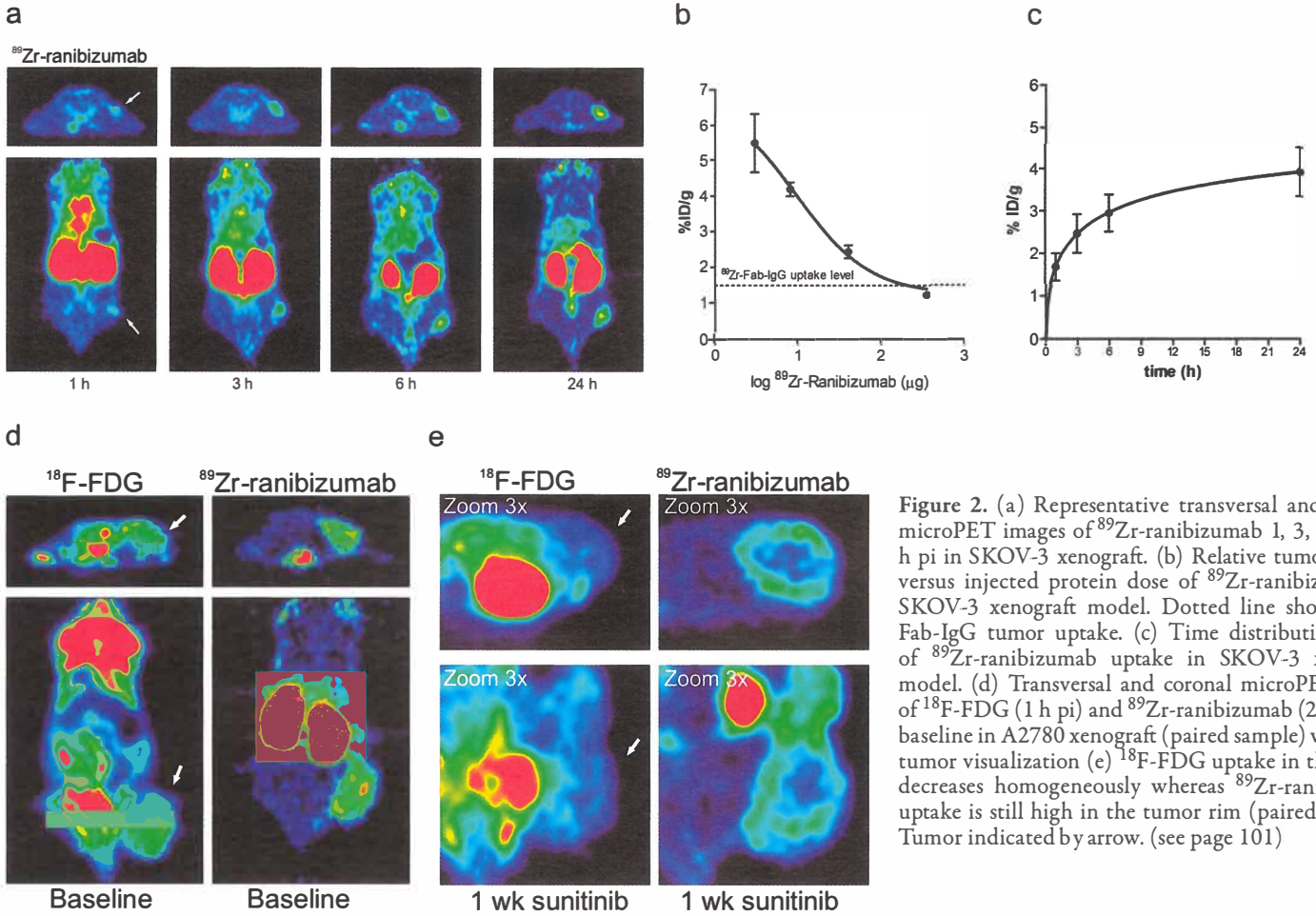

Figure 2. (a) Representative transversal and coronal microPET images of ^{89}Zr-ranibizumab 1, 3, 6 and 24 h pi in SKOV-3 xenograft. (b) Relative tumor uptake versus injected protein dose of ^{89}Zr-ranibizumab in SKOV-3 xenograft model. Dotted line shows ^{89}Zr-Fab-IgG tumor uptake. (c) Time distribution curve of ^{89}Zr-ranibizumab uptake in SKOV-3 xenograft model. (d) Transversal and coronal microPET image of ^{18}F-FDG (1 h pi) and ^{89}Zr-ranibizumab (24 h pi) at baseline in A2780 xenograft (paired sample) with clear tumor visualization (e) ^{18}F-FDG uptake in the tumor decreases homogeneously whereas ^{89}Zr-ranibizumab uptake is still high in the tumor rim (paired sample). Tumor indicated by arrow. (see page 101)

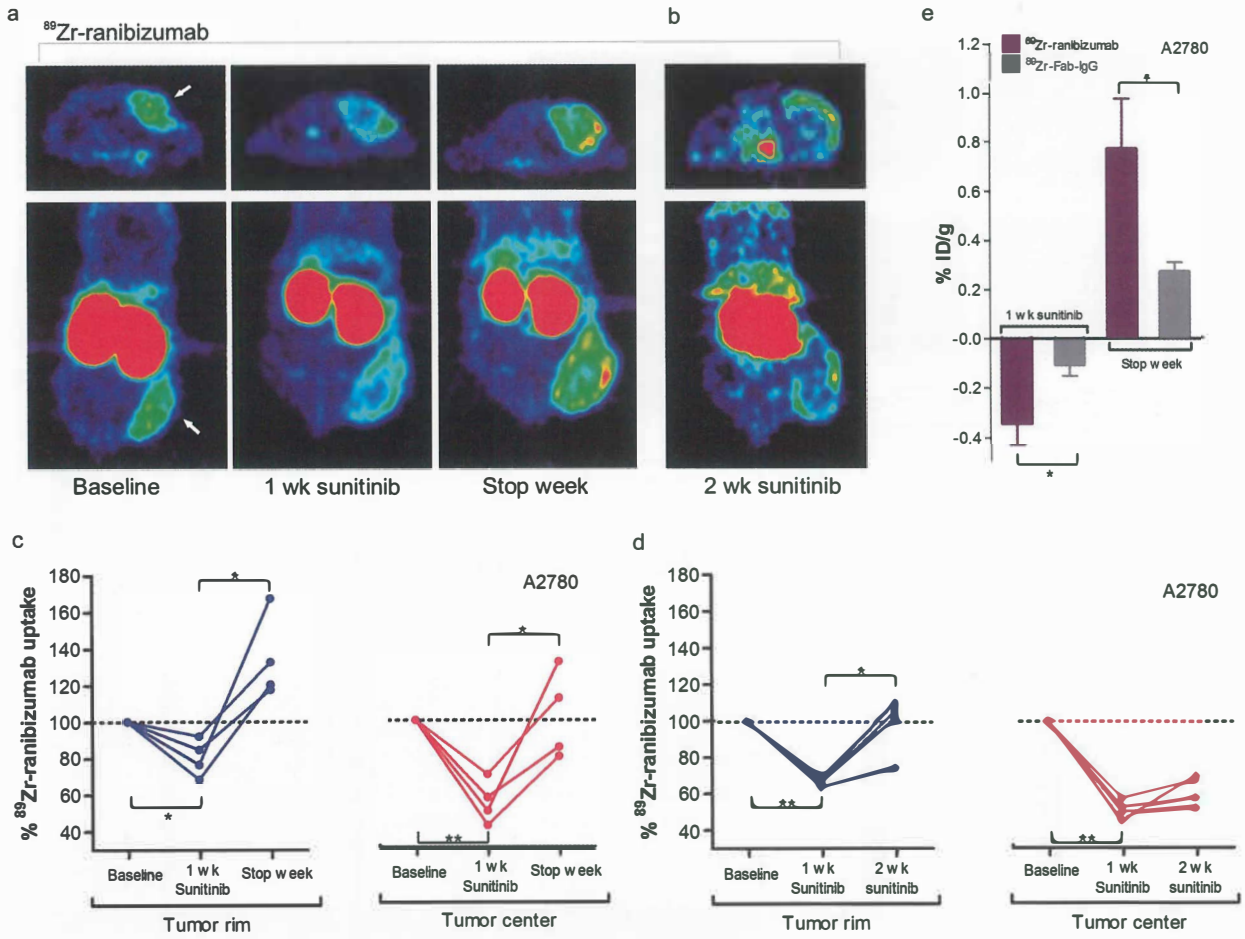

Figure 3. Transversal and coronal microPET images of ^{89}Zr-ranibizumab at 24 h post injection of the tracer (a) High tumor to background ratios clearly visualize a more pronounced reduction in the tumor center compared with the tumor rim after 7 d of sunitinib treatment. After 7 d of discontinuation, ^{89}Zr-ranibizumab uptake increases (paired samples). (b) At d 14 of sunitinib treatment, ^{89}Zr-ranibizumab uptake returns to baseline in the tumor rim while remaining low in the tumor center. ^{89}Zr-ranibizumab quantification of tumor rim and center of mice treated with sunitinib for 1 week at d 7 and following a stop week (c) and after 14 days of sunitinib treatment (d). Individual tumor uptake values are normalized relative to baseline. (e) Change in average tumor uptake (both rim and center) of ^{89}Zr-ranibizumab and ^{89}Zr-Fab-IgG after 7 d of sunitinib and after a stop week in A2780 xenograft model. * $P < 0.05$, ** $P < 0.01$. *Data presented as SEM.* (see page 103)

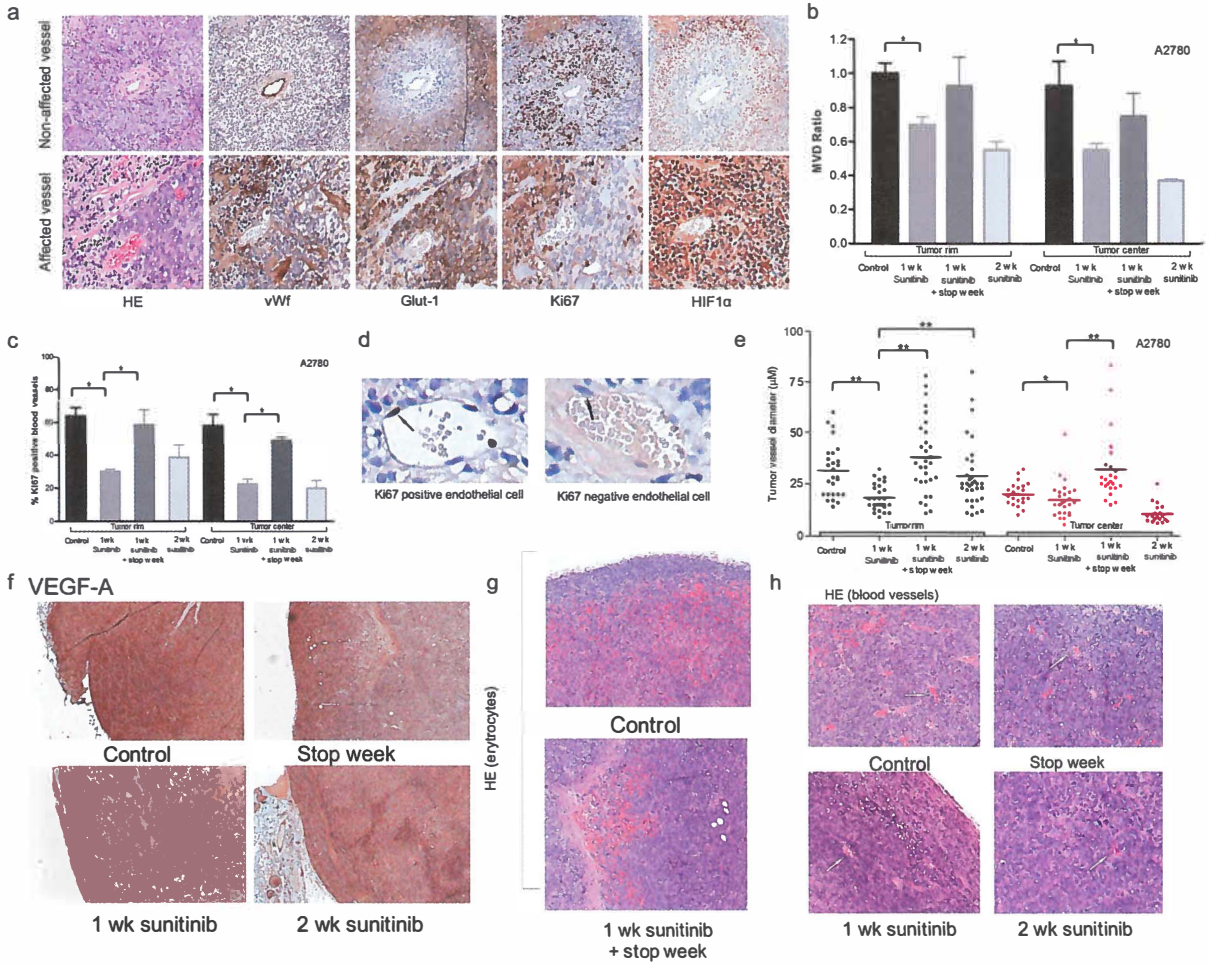

Figure 4. (a) Representative examples A2780 of affected and non-affected tumor vessels following 7 d of sunitinib treatment. Non-affected vessels demonstrates clear vWf staining with low Glut-1 expression, high Ki67 staining and low HIF1α expression in the surrounding tumor tissue which is the opposite for affected tumor vessels. (b) MVD quantification of the tumor rim and center. (c) Percentage of tumor vessels containing Ki67 positive endothelial cells in tumor rim and center. (d) Example of Ki67 positive and negative endothelial cell. (e) Tumor vessel diameter of tumor rim and center. (f) Representative VEGF-A staining. (g) Example of pelioses, randomly distributed red blood cells throughout the tumor at baseline and after stopping sunitinib. (h) Representative examples of blood vessel distribution in the tumor. * $P < 0.05$, ** $P < 0.01$. *Data presented as SEM.* (see page 105)

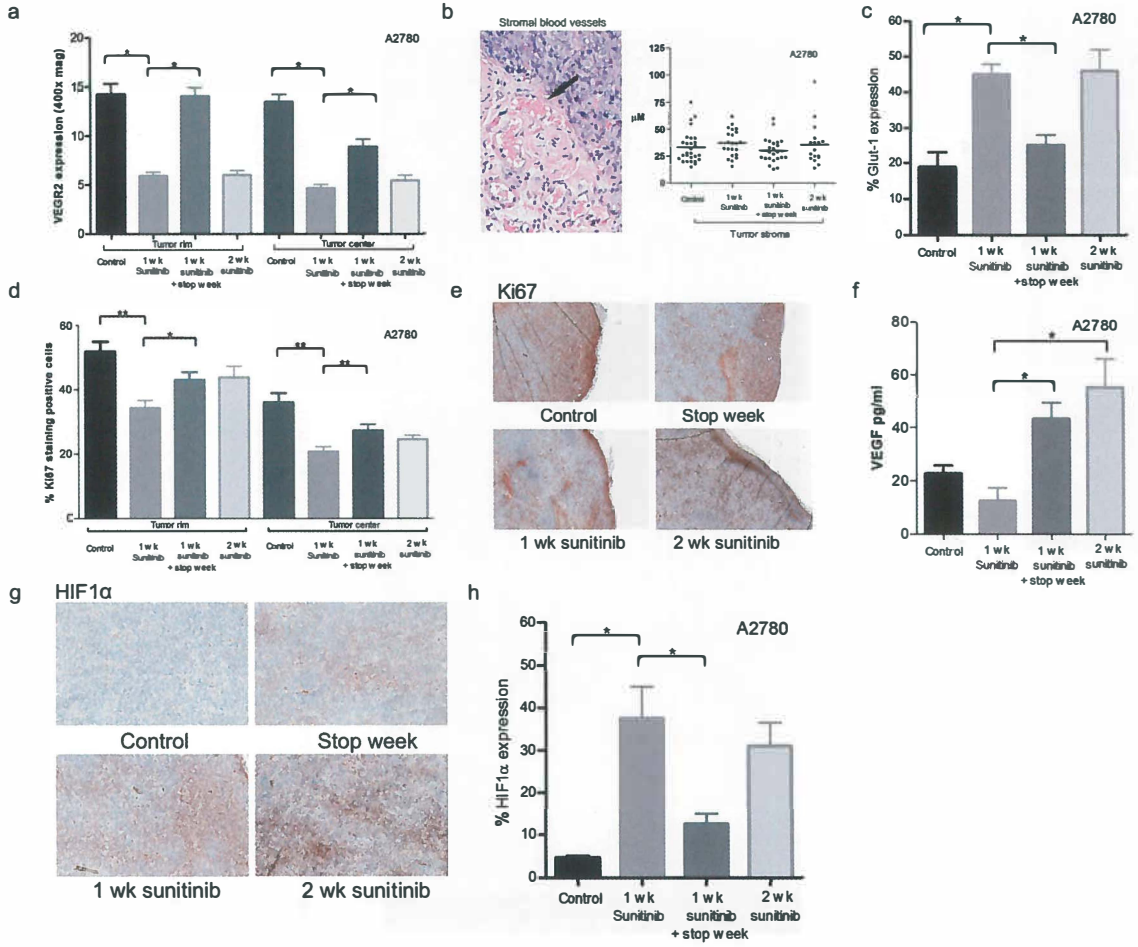

Figure 5. (a) VEGFR2 staining in the tumor rim and center. (b) Peritumoral stromal blood vessels adjacent to the tumor rim and stromal blood vessel diameter. (c) Whole tumor Glut-1 expression. (d) Tumor proliferation rate at the tumor rim and center. After 7 d of sunitinib overall tumor proliferation decreases, though it remains high at the rim. (e) representative examples of Ki67 staining. (f) Human VEGF plasma levels of sacrificed A2780 bearing animals. (g) Representative examples of HIF1α expression. (h) Tumor HIF1α expression. * $P < 0.05$, ** $P < 0.01$. *Data presented as SEM.* (see page 168)

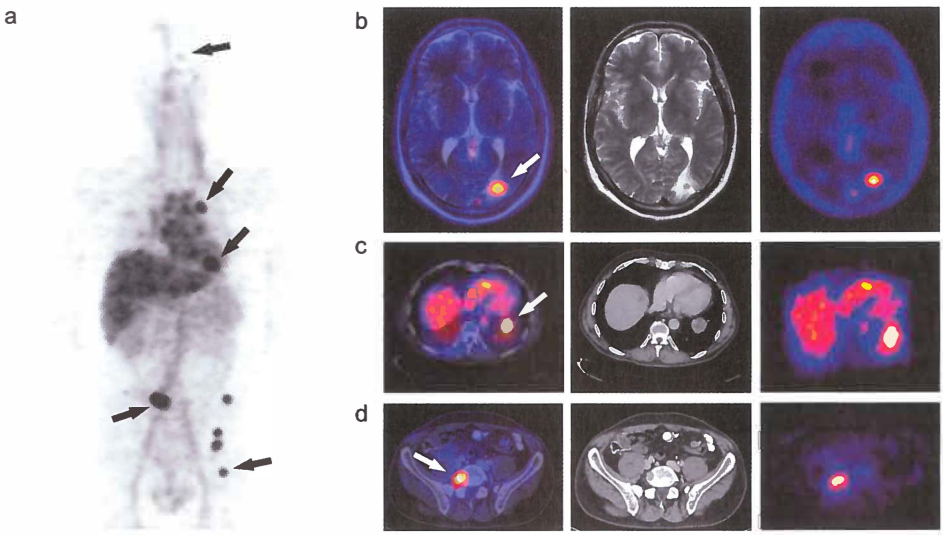

Figure 6. (a) Representative clinical VEGF-PET whole body image 4 days post injection of 37 mBq ^{89}Zr-bevacizumab in a metastatic RCC patient. PET/CT image, CT and PET images of brain (b), lung (c) and vertebral (d) metastatic lesions. Tumors indicated by arrow. (see page 107)

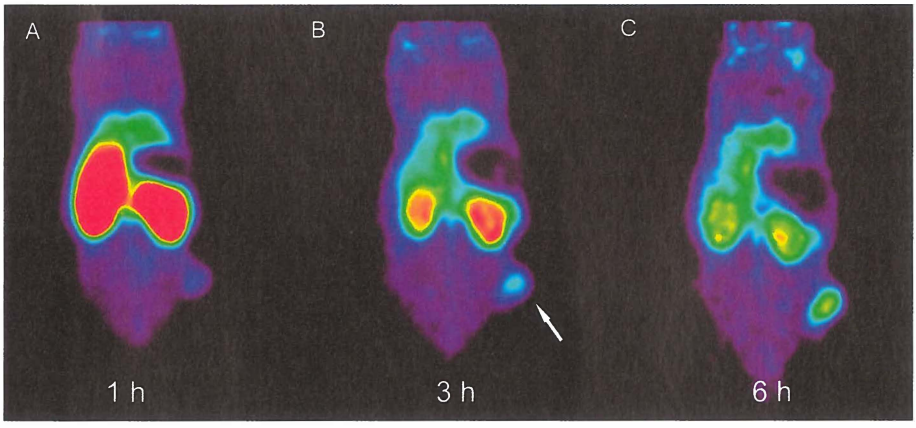

Supplement 4 . Coronal microPET images of ^{18}F-ranibizumab 1, 3 and 6 h post injection. In time, ^{18}F-ranibizumab accumulates in the tumor whereas uptake in well perfused organs decreases. Tumor indicated by arrow. (see page 109)

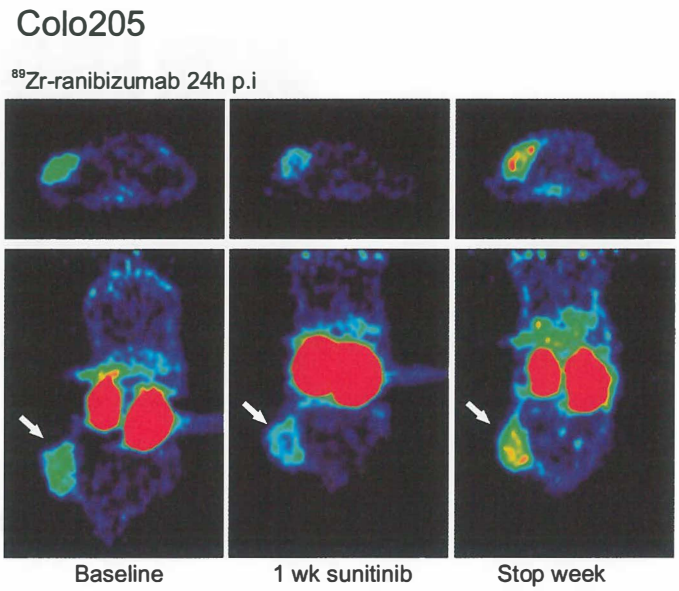

Supplement 5. Transversal and coronal microPET images of ^{89}Zr-ranibizumab at baseline, following 1 week of sunitinib treatment and after 1 stop week. After 1 week of sunitinib treatment ^{89}Zr-ranibizumab uptake decreases, mainly in the center of the tumor. After 1 week of discontinuation, ^{89}Zr-ranibizumab uptake increases. (see page 110)

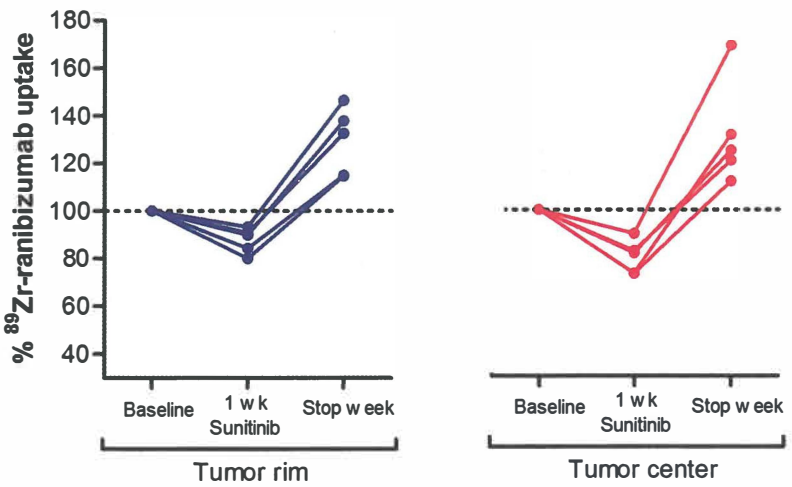

Supplement 6. ^{89}Zr-ranibizumab quantification of tumor rim and center of Colo205 mice treated with sunitinib for 1 week at d 7 and following a stop week. (see page 110)

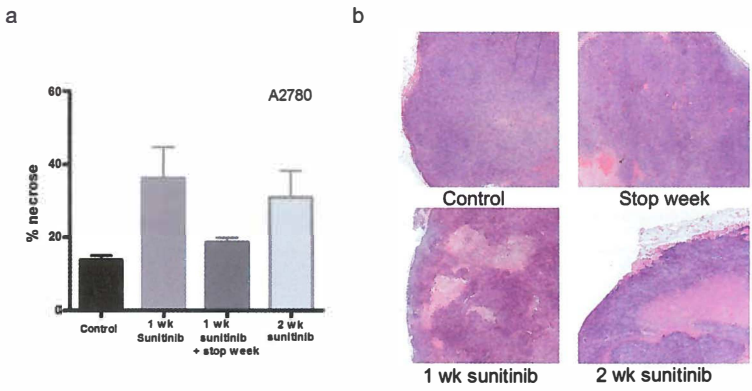

Supplement 7. (A) percentage necrosis of A2780 tumors at baseline, following 1 week of sunitinib treatment, after 1 stop week and after 2 weeks of sunitinib treatment. Individual tumor uptake values are normalized relative to baseline. (B) Representative HE staining at baseline, following 1 week of sunitinib treatment, after 1 stop week and after 2 weeks of sunitinib treatment. (see page 111)